ABSTRACT

Title of Document: RATIONAL DESIGN OF NON-DAMAGING CAPACITIVELY COUPLED PLASMA ETCHING AND PHOTORESIST STRIPPING PROCESSES FOR ULTRALOW K DIELECTRIC MATERIALS

Ming-Shu Kuo, Doctor of Philosophy, 2010

Directed By: Professor Gottlieb S. Oehrlein,
Department of Materials Science and Engineering
and Institute for Research in Electronics and Applied
Physics

Resistance-capacitance delay, crosstalk, and power dissipation associated with the increasing capacitance of interconnect structures limits the performance of high-speed microelectronics and leads to the demand for porous ultralow dielectric constant (ULK) material introduction. Process integration of ULK dielectrics requires plasma etching of dielectric material, stripping of the post-etching photoresist (PR) mask, and surface cleaning of plasma-etching-related residues, without damaging the dielectric. Dual frequency capacitively coupled plasma (CCP) reactor are becoming the standard for etching of ULK materials. In this work, we evaluated ULK-

compatible PR stripping using both remote plasma and *in situ* ashing processes coordinated with CCP fluorocarbon (FC)-based ULK etching. Remote H_2 plasma enabled a high PR ashing rate while introducing little ULK damage at an elevated substrate temperature (275 °C), and was the best for our remote plasma ashing processes. *In situ* ashing, with the advantage of no need for an additional dedicated reactor, is preferable to the remote plasma ashing for industry, and we studied in detail CO_2 *in situ* ashing process. The ULK damage introduced during CO_2 *in situ* ashing increased with atomic oxygen density as a function of chamber pressure. To compare the performance of different ashing processes for PR stripping from ULK material, we introduced an ashing efficiency (AE) parameter which is defined as the thickness of PR removed over the thickness of ULK simultaneously damaged, and can be considered a process figure of merit. A high AE can be obtained under low pressure operation, which suppresses ULK damage with minimal atomic oxygen while combining with a RF bias to enhance the PR ashing rate. The preceding ULK etching process using 10% C_4F_8/Ar plasma deposits FC coating on ULK feature sidewalls. For H_2-based remote plasma at high temperature, most of FC coating was removed rapidly and its impact on ULK ashing damage was minor. For CO_2 *in situ* ashing, FC coating remained on ULK sidewalls and provided effective protection of ULK. FC protection was essential for the success of the CO_2 *in situ* ashing process. A strong decrease of ULK post-ashing damage with increasing FC coverage was found, which may be due to surface protection by FC surface coverage along with pore-sealing by the FC material.

RATIONAL DESIGN OF NON-DAMAGING CAPACITIVELY COUPLED PLASMA ETCHING AND PHOTORESIST STRIPPING PROCESSES FOR ULTRALOW K DIELECTRIC MATERIALS

By

Ming-Shu Kuo

Dissertation submitted to the Faculty of the Graduate School of the
University of Maryland, College Park, in partial fulfillment
of the requirements for the degree of
Doctor of Philosophy
2010

Advisory Committee:
Prof. Gottlieb S. Oehrlein, Dept. of Materials Science & Engineering, Chair
Prof. Robert M. Briber, Dept. of Materials Science & Engineering
Prof. Sheryl H. Ehrman, Dept. of Chemical & Biomolecular Engineering
Prof. Reza Ghodssi, Dept. of Electrical & Computer Engineering
Prof. Joonil Seog, Dept. of Materials Science & Engineering

© Copyright by
Ming-Shu Kuo
2010

Acknowledgements

First and foremost, I would like to thank my advisor, Professor Oehrlein, whose guidance and encouragement with patience support me in regard to research and life throughout the past five years. Your devotedness and emphasis on teamwork help create an excellent research environment, and your professional knowledge and abundant experience constantly lead me into correct direction.

Second, I would like to acknowledge Semiconductor Research Corporation (SRC) Center for Advanced Interconnect Science and Technology (CAIST) for their financial support and providing precious opportunities to interact with industries.

I would also like to thank the collaboration with companies and other research groups. I thank Paolo Lazzeri and Mariano Anderle (ITC-irst, Center for Scientific and Technological Research, Italy) for the characterizations using time-of-flight secondary ion mass spectroscopy (ToF SIMS), Abbas Ali, Ping Jiang (Texas Instruments) and Xuefeng Hua (while at IBM) for scanning electron microscopy (SEM) characterizations, and Andrew Li (AMAT), Stephen Sirard and Eric Hudson (Lam Research) for providing samples. I appreciate your contribution to this work.

I thank my former and current colleagues, Xuefeng Hua, Li Ling, Sebastian Engelmann, Bryan Orf, Robert Bruce, Guido Stueber, Florian Weilnboeck, Deuk Yeon Lee, Masahiro Sumiya, Arup Pal and Nicolas Fox-Lyon for helpful discussion and assistance in lab maintenance and research. I express my gratitude to Jay Pyle and John Rodgers (IREAP) who have helped me learn a variety of material

machining and equipment maintenance skills. I especially thank Nirav Kumar and Paul Yu for critical proofreading of this thesis.

I would especially like to thank Prof. Robert Briber, Prof. Sheryl Ehrman, Prof. Reza Ghodssi, and Prof. Joonil Seog for the effort to serve on my committee and for their invaluable input.

Finally, I owe my deepest appreciation to my family in Taiwan. My parent, sister, and brother's family, your unconditional love and unwavering support help me make it through my life in United States. I love you all.

Table of Contents

Acknowledgements ii
Table of Contents iiv
List of Tables vii
List of Figures viii

Chapter 1: Introduction 1

1.1 Basic Plasma Processing of Materails 1
1.1.1 Plasma Sources for Plasma Processing of Materials 2
1.2 Back-End-of-Line Interconnect Process 8
1.3 Challenge of Plasma Processing at Nanoscale Dimension 10
1.4 Facilities of the Laboratory for Plasma Processing of Materials 13
1.5 Thesis Outline 14

Chapter 2: Influence of C_4F_8/Ar-Based Etching and H_2-Based Remote Plasma Ashing Processes on Ultralow k Material Modifications 17

2.1 Introduction 20
2.2 Experimental Setup and Procedures 23
2.3 Results and Discussion 28
2.3.1 Blanket Materials Exposed to Remote Discharges 28
2.3.2 Etching/Ashing Combined Experiments 42
2.4 Conclusions 56

Chapter 3: Mechanistic Study of ULK-Compatible CO_2 *In Situ* Photoresist Ashing Processes. I. Process Performance and Influence on ULK Material Modification 59

3.1 Introduction 61
3.2 Experimental Setup and Procedures 62
3.2.1 Capacitively Coupled Plasma Source and
Small Gap Structure 63
3.2.2 Material Diagnostic 64
3.2.3 Plasma Diagnostic 65
3.3 Results and Discussion 65
3.3.1 Ashing Efficiency 65
3.3.2 ULK Material Modifications 77
3.4 Conclusions 83

Chapter 4: Mechanistic Study of ULK-Compatible CO_2 *In Situ* Photoresist Ashing Processes. II. Interaction with Preceding Fluorocarbon Plasma ULK Etching processes 85

4.1 Introduction 87
4.2 Experimental Setup 88
4.3 Results and Discussion 90
4.3.1 PR Ashing 90
4.3.2 ULK Damage 95
4.3.3 Ashing Efficiency 101
4.3.4 Validation Using
Actual Pattern Transfer Process Sequence 102
4.4 Conclusions 106

Chapter 5: Surface and Near-surface modification of Ultralow Dielectric Constant Materials Exposed to Plasma under Sidewall-like Conditions
ULK etching processes 108

5.1 Introduction 110
5.2 Experimental Setup 110

5.3 Results and Discussion 115
5.3.1 Real-Time Ellipsometry Study for Individual Process 115
5.3.2 Process Interaction for ULK Damage 126
5.4 Conclusion 130

Chapter 6: General Conclusions... 133

Chapter 7: Future Works 138

References 142

List of Tables

Chapter 1:

Table 1.1: Organization chart of researchers and competencies.

Chapter 5:

Table 5.1: Discharge parameters used in this work. For real time study of ULK plasma modification, ULK films were respectively exposed to C_4F_8/Ar, Ar, and O_2 or CO_2 plasma under an ellipsometric roof and monitored by real time ellipsometry. The effects of Ar ion bombardment (100 W bias power applied) were also studied using ULK film with line-of-sight Ar plasma exposure. For the study of etching/ashing process interaction, ULK films under a regular roof were processed with the different C_4F_8/Ar etching followed by a standard CO_2 *in situ* ashing processes. Post-ashing damage was quantified by DHF method.

List of Figures

Chapter 1:

Figure 1.1: Schematic diagram of the ICP reactor used in this work

Figure 1.2: Schematic diagram of the dual frequency CCP reactor used in this work

Figure 1.3: Cross-section of hierarchical scaling of MPU device (from IRTS 2007)

Figure 1.4: Via-first dual damascene patterning scheme for forming trenches and holes in dielectric materials that will be filled with metal to form the interconnecting wiring of an IC

Figure 1.5: University of Maryland cluster system for plasma processing of materials

Chapter 2:

Figure 2.1: Illustration of ULK damage issue introduced by plasma-based PR stripping during the fabrication of an interconnecting structure.

Figure 2.2: Schematic of the gap structure. Samples placed in the region shielded by the roof primarily interact with neutral, the remote plasma processing regime.

Figure 2.3: (a) Schematic of the small gap structure used in this work. (b) Simulation of ULK sidewall with blanket samples in region (III) (*Drawings not to scale*).

Figure 2.4: (a) PR ashing rate, (b) ULK damage thickness, and (c) AE for 20 s remote plasma processing at various substrate temperatures and plasma chemistries. ULK damage thickness was evaluated using 1% HF solution/15 s dipping method. AE is defined as the thickness of PR layer removed divided by the thickness of ULK material damaged during the same process step (20 s plasma exposure in this work).

Figure 2.5: OES for H_2/N_2 (1/1) plasma in ICP reactor. 3% Ar was also added to the gas mixture to enable application of Ar actinometry. The emission lines selected for Ar actinometry are indicated with a * symbol.

Figure 2.6: (a) Optical emission intensities of selected spectral lines detected for H_2/N_2 discharges. In (b), the emission line/Ar (811.6 nm) intensity ratios are shown as a function of the nitrogen content in the H_2/N_2 mixtures fed to plasma. The Ar line intensities were recorded using 3% argon in the discharges.

Figure 2.7: Arrhenius plots of (a) PR ashing rate and (b) ULK damage thickness for remote plasma processing. Results obtained with pure H_2, H_2/N_2 (1/1), and pure N_2 plasma chemistries are displayed.

Figure 2.8: C 1*s*, Si 2*p*, O 1*s*, and N 1*s* XPS spectra of untreated ULK and ULK exposed to pure H_2, H_2/N_2 (1/1), and pure N_2 remote plasmas at RT and 275 °C for 60 s. The numbers listed next to the peaks of the C 1*s*, Si 2*p*, and O 1*s* spectra are the integrated C-Si/C-C, Si, and O peak intensities divided by the values measured for untreated ULK.

Figure 2.9: ULK damage thickness for plasma etching/remote plasma ashing process sequences and ashing only. Plasma etching using a CCP reactor was performed using $C_4F_8/Ar/O_2$ for 148 s and $C_4F_8/Ar/N_2$ for 191 s. A small gap structure was used to expose the ULK material for sidewall-like conditions. The ashing processes consisted of exposures to H2 or H_2/N_2 (1/1) remote discharges for 60 s. Damage thickness was evaluated using the 1% HF solution selective etching method.

Figure 2.10: C 1*s*, F 1*s*, N 1*s*, Si 2*p*, and O 1*s* XPS spectra on ULK films exposed to CCP $C_4F_8/Ar/O_2$ etching plasma for 148 s or $C_4F_8/Ar/N_2$ etching plasma for 191 s in a small gap structure, which simulated sidewall-like exposure conditions.

Figure 2.11: C 1*s*, Si 2*p*, O 1*s*, F 1*s*, and N 1*s* XPS spectra of ULK films exposed to CCP etching plasmas and remote ashing plasma process sequences. CCP etching plasma exposures were performed using $C_4F_8/Ar/O_2$ plasma for 148 s or $C_4F_8/Ar/N_2$ plasma for 191 s in a small gap structure, which simulated sidewall-like exposure conditions. Subsequent remote plasma exposures were performed using H_2 or H_2/N_2 (1/1) remote plasmas for 60 s. For comparison, the spectra of blanket ULK film and ULK films with remote plasma exposure (ashing controls) are also shown. (a) Untreated ULK; (b) H_2 remote ashing only; (c) $C_4F_8/Ar/O_2$ etching + H_2 remote ashing; (d) $C_4F_8/Ar/N_2$ etching + H_2 remote ashing; (e) H_2/N_2 remote ashing only; (f) $C_4F_8/Ar/O_2$ etching + H_2/N_2 remote ashing; (g) $C_4F_8/Ar/N_2$ etching + H_2/N_2 remote ashing.

Figure 2.12: Summaries of (a) integrated intensities of C-Si/C-C in C 1*s*, Si in Si 2*p*, and O in O 1*s*, and of (b) Si 2*p* and O 1*s* binding energies from Fig. 2.11. The integrated intensities are normalized relative to the values measured for the untreated ULK.

Figure 2.13: ToF-SIMS depth profiling of ULK for plasma etching/remote plasma ashing combined experiments and ashing controls. CCP etching plasma exposures were performed using $C_4F_8/Ar/O_2$ for 148 s or $C_4F_8/Ar/N_2$ for 191 s in a small gap structure, which simulated sidewall-like exposure conditions. Remote plasma exposures were performed using D_2 remote plasma with 275 °C substrate for 60 s.

Figure 2.14: Illustration and SEM cross-sectional profiles of ULK trenches etched using (a) CCP $C_4F_8/Ar/O_2$ plasma for 177 s, (b) subsequently ashed by pure H_2, or (c) H_2/N_2 (1/1) remote plasma at 275 °C substrate for 60 s, and finally dipped into 1% HF solution/15 s for damage evaluation [(b)→(d), (c)→(e)].

Figure 2.15: SEM cross-sectional profiles of ULK trenches etched using (a) CCP $C_4F_8/Ar/N_2$ plasma for 228 s, (b) subsequently ashed by pure H_2, or (c) H_2/N_2 (1/1) remote plasma at 275 °C substrate for 60 s, and finally dipped into 1% HF solution/15 s for damage evaluation [(b)→(d), (c)→(e)].

Chapter 3:

Figure 3.1: Photoresist ashing rate (a), ULK damage (b), and ashing efficiency (c) of CO_2 and O_2 discharges as a function of gas pressure. The other experimental parameters were: 40 SCCM gas flow, 200 W source power, no bias power to substrate. ULK damage was evaluated for 2 min of exposure. AE is defined as the thickness of PR layer removed divided by the thickness of ULK material damaged during the same process step (2 min of plasma exposure in this work).

Figure 3.2: Damage thickness of ULK exposed to CO_2 and O_2 discharges as a function of atomic oxygen density measured for discharges operated at different gas pressures. The other experimental parameters were: 40 SCCM gas flow, 200 W source power, no bias applied to substrate and 2 min exposure time. Changes in atomic oxygen density were determined from the intensity variation of the 844.6 nm O atom related emission line and Ar actinometry.

Figure 3.3: PR ashing rates measured for CO_2 and O_2 discharges operated between 10 and 100 mTorr. PR ashing rates are plotted versus the ion current

density measured for the same conditions. The other experimental parameters were: 40 SCCM gas flow, 200 W source power, no bias applied to substrate. The ICD was measured using a Langmuir probe 2 cm above the substrate with a -100 V bias.

Figure 3.4: Photoresist ashing rate (a), ULK damage (b), and ashing efficiency (c) of 10 and 100 mTorr CO_2/Ar discharges as a function of %Ar added to CO_2. Ashing efficiency is defined as the thickness of PR removed after 3 min of process time over the thickness of ULK damaged during the same period. Plasmas were maintained at a 40 SCCM gas flow and 200 W source power, and no bias was added to the substrate. ULK damage and AE were evaluated for 3 min of exposure.

Figure 3.5: Photoresist ashing rates measured for pure O_2 and Ar/CO_2 discharges as a function of self-bias voltage. Different CO_2/Ar mixtures were used. Plasmas were maintained at 10 mTorr of gas pressure, 40 SCCM of total gas flow and 200 W of source power.

Figure 3.6: Ionic etching yields for O_2 and Ar/CO2 discharges with -100 V self-bias.

Figure 3.7: C 1*s*, Si 2*p* and O 1*s* photoemission difference spectra obtained with ULK after 20 s or 200 s of plasma exposure at two different pressures (10 and 100 mTorr for O_2 and CO_2 discharges used) and ULK reference spectra (obtained with untreated control). The other experimental parameters were: 40 SCCM gas flow, 200 W source power, no bias applied to substrate. Spectra were obtained at a photoemission angle of 90° with respect to the surface.

Figure 3.8: Normalized intensity of species observed in SSIMS spectra of ULK exposed to $^{13}CO_2$ plasmas maintained at a 40 SCCM gas flow rate and 200 W source power without applying a bias to the substrate. Intensities were normalized using initial intensities.

Figure 3.9: DSIMS depth profiling results obtained with untreated ULK and ULK after exposure to $^{13}CO_2$ plasma. The discharges were maintained using a 40 SCCM gas flow rate and 200 W source power without applying a bias to the substrate.

Chapter 4:

Figure 4.1: Illustration of issues related to the fluorocarbon ULK trench etching/*in situ* PR ashing process interaction.

Figure 4.2: PR thickness removed in the CO_2 *in situ* ashing process. No bias power was applied to the substrate. For combined sequence process, a $C_4F_8/Ar/N_2$ PE process of 100 s duration preceded the *in situ* ashing.

Figure 4.3: PR ashing rate as a function of CF_4 ratio in a CF_4/CO_2 mixture. Plasmas were maintained at 40 SCCM total gas flow rate and 200 W source power. No bias power was applied to the substrate. Ashing rates using 10 and 100 mTorr gas pressure were examined and compared.

Figure 4.4: PR thickness removed in the ashing step of the combined process sequence. The ashing process was conducted using 10 mTorr CO_2 discharge. Bias power was selectively applied to the substrate. A $C_4F_8/Ar/N_2$ PE process of 100 s duration preceded the *in situ* ashing.

Figure 4.5: ULK damage in CO_2 *in situ* ashing process. No bias power was applied to the substrate. In some cases, to study etching/ashing process interaction, a $C_4F_8/Ar/N_2$ PE process of 160 s duration preceded the *in situ* ashing for the seasoning chamber and/or introducing PE-related ULK modification. A small gap structure was employed to simulate sidewall-like reaction on the blanket ULK films.

Figure 4.6: XPS C 1*s*, Si 2*p*, O 1*s*, and F 1*s* spectra of untreated ULK (a) and pristine ULK exposed to CO_2 discharges in a clean (b) and a FC-coated chamber (c) for 180 s. No bias power was applied to the substrate. A $C_4F_8/Ar/N_2$ PE process of 160 s duration was conducted to introduce a FC-coated chamber. A small gap structure was employed to simulate a sidewall-like reaction on the blanket ULK films.

Figure 4.7: XPS C 1*s* and Si 2*p* spectra of untreated, post-etching, and post-ashing ULK in the combined processes. The $C_4F_8/Ar/N_2$ etching process was conducted for 160 s. The subsequent CO_2 *in situ* discharge was maintained for 180 s without bias power applied to the substrate. Both processes were simulated with blanket ULK films in the small gap structure.

Figure 4.8: Summary of AE for CO_2 *in situ* ashing using a clean chamber and the FC-coated chamber with 10 mTorr CO_2 discharges for 180 s.

Figure 4.9: SEM cross-sectional profiles of ULK trenches etched using (a) $C_4F_8/Ar/N_2$ etching plasma for 100 s, (b) subsequently *in situ* ashed by 10 mTorr CO_2 plasma or (c) 100 mTorr CO_2 plasma without substrate

bias applied, and finally dipped into 0.5% DHF/ 15 s for damage evaluation. [(b)→(d), (c) →(e)].

Figure 4.10: SEM cross-sectional profiles of ULK trenches etched using (a) $C_4F_8/Ar/N_2$ etching plasma for 100 s, (b) subsequently *in situ* ashed by 10 mTorr CO_2 plasma without -90 V self-bias, and finally dipped into 0.5% DHF/ 15 s for damage evaluation.

Chapter 5:

Figure 5.1: Schematic of the small gap structure using the regular roof (a) and the ellipsometric roof (b), which supports *in situ* ellipsometry characterization.

Figure 5.2: (a) Real-time ellipsometric Ψ-Δ trajectories for ULK exposed to remote O_2 and CO_2 plasmas using the ellipsometric roof (remote). Modeled curves based on two-layer structure comprising the highly porous overlayer (n=1.248) and unmodified ULK film (n=1.320) are superimposed. Initial thickness of ULK film was 500 nm. Figure (b) shows a close-up for the experimental trajectories. The "compass" in figure (c) indicates general directions of trajectories for deposition or erosion, and changes in (optical) material density.

Figure 5.3: ULK damage as a function of exposure time obtained by optical two-layer modeling with refractive index n=1.248 for the plasma-modified layer (see Fig. 5.2). The ULK damage depth obtained with the DHF method for 300 s CO_2 and O_2 plasma exposure is included for comparison.

Figure 5.4: (a) Real-time ellipsometric Ψ-Δ trajectories for ULK exposed to remote or direct Ar plasma. The Ψ-Δ simulated trajectories of unmodified ULK film (n=1.320) with varying thickness and constant refractive index are shown with curve (i). Also, the Ψ-Δ simulated trajectory for a constant 12 nm silica-like densified layer (n=1.465) on top of a varying thickness of unmodified ULK is shown with curve (ii). Initial ULK film thickness was 500 nm.

Figure 5.5: (a) Real-time ellipsometric Ψ-Δ trajectories for ULK exposed to 10% C_4F_8/Ar plasma using the ellipsometric roof. Modeled curves based on a two-layer structure comprising the ULK/FC-mixed layer (n=1.446) and unmodified ULK (n=1.320) are superimposed. Initial ULK film

thickness was 500 nm. (b) The ULK/FC-mixed layer thickness is shown as a function of exposure time, and was obtained from the measured trajectories of (a) by optical modeling.

Figure 5.6: Post-ashing damage as a function of post-etching FC film thickness determined by XPS. The standard etching conditions are listed in Table I. The processing time for C_4F_8/Ar-based etching plasma, and subsequent CO_2 *in situ* ashing plasma, were 180 s and 300 s, respectively. The exposures were conducted using a regular roof. For comparison, post-ashing damages of the pristine samples processed in a clean chamber and in a FC-coated chamber seasoned with standard etching conditions are also shown. Post-ashing damage was quantified by the DHF method.

Figure 5.7: ULK post-ashing damage measured for a FC etching plasma/CO_2 ashing plasma combination as a function of ULK exposure time to the 10% C_4F_8/Ar plasma. We employed 300 s CO_2 ashing plasma exposure, regular roof, and post-ashing damage was quantified by the DHF method.

Chapter 7:

Figure 7.1: Schematic of tri-layer masking

Chapter 1: Introduction

1.1 Basics of Plasma Processing of Materials

Plasmas are partially ionized gases with, on the average, an equal number of positive and negative charges, generated in electrically neutral gases with external energies e.g. heat or radiation, which strip electrons from atoms or molecules. Next to solid, liquid and gas, it is the fourth state of matter which comprises more than 99% of the universe in volume and mass.

Weakly ionized low temperature plasmas are widely used for thin film material processing.[1.1-1.5] Most of these plasmas are driven by external electrical field. In the field, energy is primarily given to the electrons which are mobile and easily accelerated. Even though kinetic energy can be exchanged between particles through elastic collisions, the enormous difference of mass restricts energy transfer from electrons to heavy particles. Ions can only absorb little energy directly from electrical field and share with neutrals by collisions. Since the temperature of electrons is much higher, often tens of thousands of degree, than that of ions and neutrals, the plasma is in a state of nonequilibrium. This is advantageous to processing of materials which are sensitive to thermal approaches. First, reactive species such as free radicals, that without plasma would require temperature in the range of $\sim 10^3$-10^4 K, can be generated from gas molecules which undergo inelastic collision with energetic electrons and remain at relatively low temperature. Second, the thermal velocity of electrons is much higher than that of ions because of low mass. The surface in contact with plasma can rapidly collect a net negative charge which repels electrons and is

surrounded by a net positive space charge. The layer of positive space charges, referred to as plasma sheath, leads a potential drop to a surface which can be tailored with bias. Positive ions diffusing into the sheath are accelerated and deliver energy to the surface in the form of ion bombardment. Hence, the chemistry which takes place on surfaces with reactive species at low temperature can be further promoted without heating the substrate.

1.1.1 Plasma Sources for Plasma Processing of Materials

Capacitively coupled plasma (CCP) have been commonly used in etching and deposition tools since the 1970's, but the relatively low plasma density limited its application to processing materials with complex structures. In order to overcome the limitation, high density plasma driven by other modes including inductive coupling, electron cyclotron resonance (ECR), and helicon resonance have been developed.[1.6] Of these, the inductive coupled plasma (ICP) has the simplest equipment configuration and quickly dominated the markets of the semiconductor industry. In this work, both ICP and CCP are used. Their basic experimental setup and plasma principles are briefly reviewed in the following.

Also, since the late 1990's low *k* materials have been replacing conventional SiO_2 as dielectric films for back-end-of-the-line (BEoL) interconnect technology,[1.7,1.8] but are susceptible to plasma damage.

A. Inductively Coupled Plasma

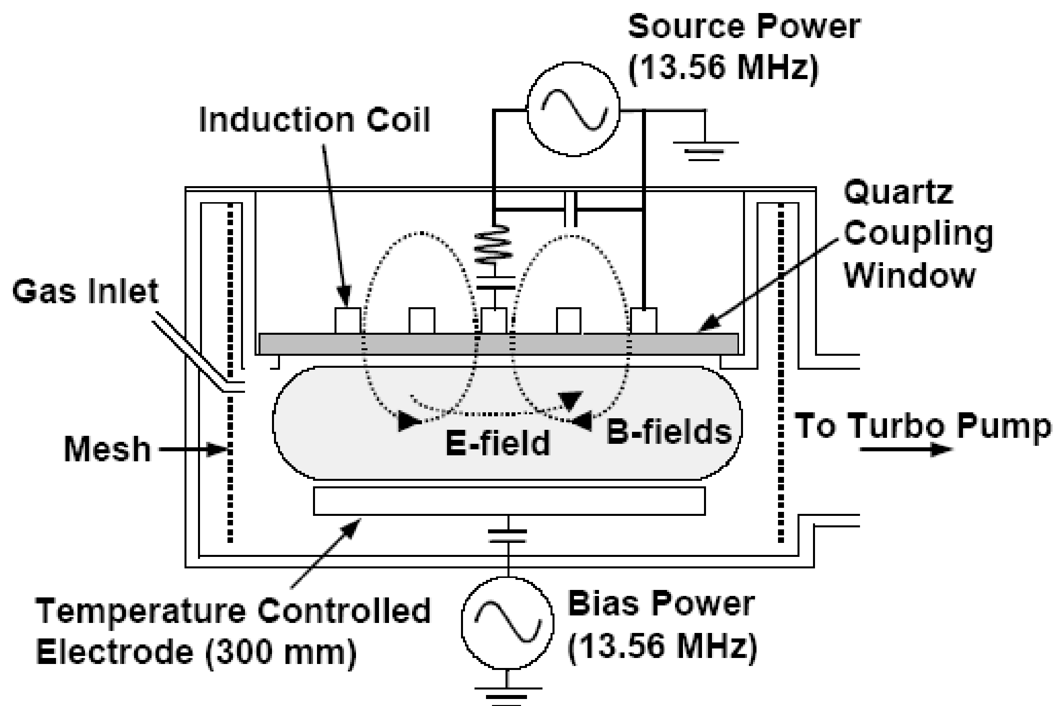

Figure. 1.1: Schematic diagram of the ICP reactor used in this work.

The ICP reactor used in this work is shown in Fig. 1.1. . The stainless steel chamber below the quartz window is pumped using a turbomolecular pump backed by a roots blower and a mechanical pump. The chamber base pressure is about 8×10^{-6} Torr. Process gases are fed into the using mass flow controllers. Typical total gas flow was set at 50 SCCM (SCCM denotes cubic centimeters per minute at STP), and the constant gas pressure was maintained at the order of 10 mTorr using a throttle valve in the pump line. A planar coil is placed on top of a quartz coupling window and powered by a 13.56 MHz rf generator. The matching of power is achieved by an L-type matching network configuration. When a RF current is driven through the coil,

an electromagnetic field is coupled into the vacuum chamber below the window. Since electrons are much mobile and able to respond to the applied electromagnetic fields varying at 13.56 MHz, an electron current runs below the quartz window in the opposite direction of the coil current and shields the electromagnetic fields. The electron current normally concentrated within a skin depth of the plasma surface, typically a few centimeters. Low energy electrons in this current cannot efficiently transfer their kinetic energy to massive neutrals. Hence, electrons can sustain their energies while colliding with neutrals and are heated by the electromagnetic fields. The electron temperature is 3-5 eV for typical processing conditions and is much higher than the ion/neutral temperature, which is of the order of 0.05 eV. When the electron energies have been sufficiently promoted, typically from 1 to 20 eV, electrons can transfer their energies to neutrals and ions through inelastic collisions which lead to excitation, dissociation, attachment, ionization, recombination, or their combination. The discharge can be maintained when the electron generation through ionization balances the electron loss in the plasma.

Additionally, the electrode in contact with the plasma charges up negatively while a positive space charge builds up near the surface. This space charge is referred to as a sheath. The sheath thickness is on the order of 1 mm and is the only region where charge separation exists. The potential across the sheath, i.e. the sheath potential, is typically 10-30 V. It accelerates the ions that enter the sheath towards the substrate which is placed on the electrode. The energy of the bombarding ions to the 300 mm diameter of substrate electrode can be independently increased through use of another 13.56 MHz rf generator and matching network assembly. During the first

rf cycles, electrons are collected faster than ions at the electrode. The substrate charges up more negatively while the positive sheath near the substrate expands. This increases the time-averaged sheath voltage and the energy of impacting ions. The wafer is mounted at the center of the electrode that is cooled by a low temperature circulator. The ability to control ion energies independent of plasma density is an important feature of high density plasma systems and is absent in rf diodes, where the substrate electrode is used for plasma generation.

B. Capacitively Coupled Plasma

Capacitive sources are often referred to as rf diodes.[1,3] The discharge is sustained by the rf current directly applied to an electrode immersed in the plasma. The energies are coupled from rf currents to plasma electrons in two main ways: (1) *Ohmic or collision heating.* Free electrons in the plasma bulk respond to the instantaneously electric fields produced by the rf driving voltage and oscillate back and forth while massive ions respond only to the time-averaged electric field. (2) *Stochastic or collisionless heating.* Electrons are reflected from the field of a high-voltage sheath and obtain momentum from the oscillating boundary. Energetic electrons are also created at the cathode because of secondary emission by ion bombardment. These electrons are accelerated by the sheath back into the body of the plasma. This secondary electron emission becomes important only if the electrode is made of the materials with a high secondary electron emission coefficient.

Due to the inherent difference in electron heating, the plasma density of CCP is relatively lower than that of inductively coupled plasma. A high rf power can be

applied to increase the density, but it results in many issues, such as a low efficiency of plasma heating and the erosion of the electrode due to high voltage sheaths. The plasma density of capacitive source is typically limited to 10^{10} cm^{-3}. For a reasonable ion flux, the ion energy resulting from the broad sheath is usually high. It can lead to undesirable damage for wafer placed on the plasma-driven electrode. To independently control the plasma density and ion bombarding energy, CCP reactors employ two different RF frequencies. The high frequency RF supply is used to produce the plasma (source) and the low frequency RF supply is used to bias the substrate. This design is based on the fact that high frequency drive can produce a higher plasma density for a given power and avoid the interference to low frequency drive which controls the ion energy. Due to the advantage in selectivity and damage control, dual frequency CCP reactors are becoming the standard for etching of low dielectric constant materials. The pressure used in CCP is usually in the range of ten to hundreds mtorr, which is higher than for ICP. In addition, the floating potential in the CCP is strongly dependent on the chamber geometry and other processing parameters. It usually ranges from tens to hundreds volts, which is much higher than that in inductively coupled plasma.

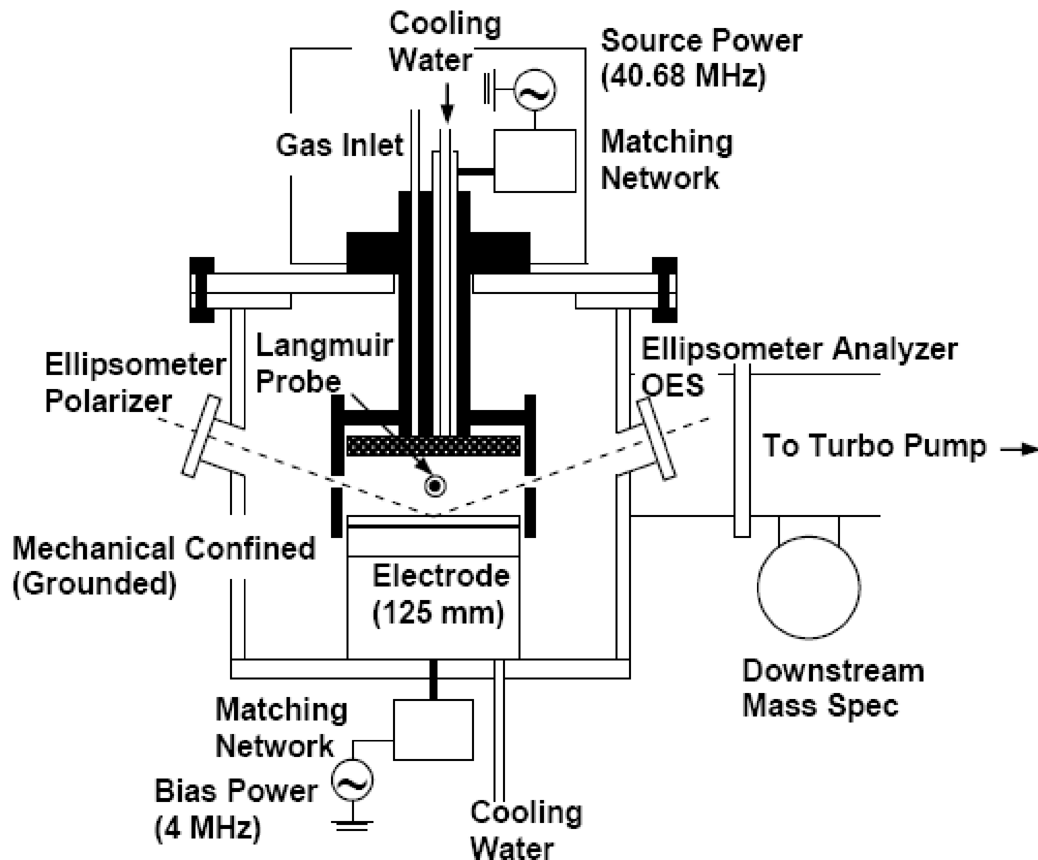

Figure. 1.2: Schematic diagram of the dual frequency CCP reactor used in this work.

A schematic of the dual frequency capacitively coupled plasma (CCP) reactor used in this work is shown in Fig. 1.2. The electrodes are inserted in a stainless steel vacuum chamber with an inner diameter of 250 mm. The diameters of the top and bottom electrodes are 150 and 125 mm respectively and the interelectrode distance is 40 mm. An aluminum confinement ring with 150 mm diameter surrounds both electrodes and interelectrode space, and mechanically confines the plasma and provides an additional ground reference. The top electrode features a showerhead design for uniform gas distribution and is powered using a 40.68 MHz rf generator

and Π-matching network configuration. Typical powers applied are in the range of 100-300 W. The bottom electrode (substrate) is powered through a modified L-matching network using a 4 MHz rf generator. Typical rf bias power applied are in the range of 50-150 W. The temperature of the bottom electrode is controlled at 10 °C using a low temperature circulator. The vacuum system is similar to that of the ICP reactor. The chamber base pressure is about 8×10^{-6} Torr. Typical total gas flow was set at 40 SCCM and the gas pressure was varied from 10 to 100 mTorr.

1.2 Back-End-of-Line (BEoL) Interconnect Process

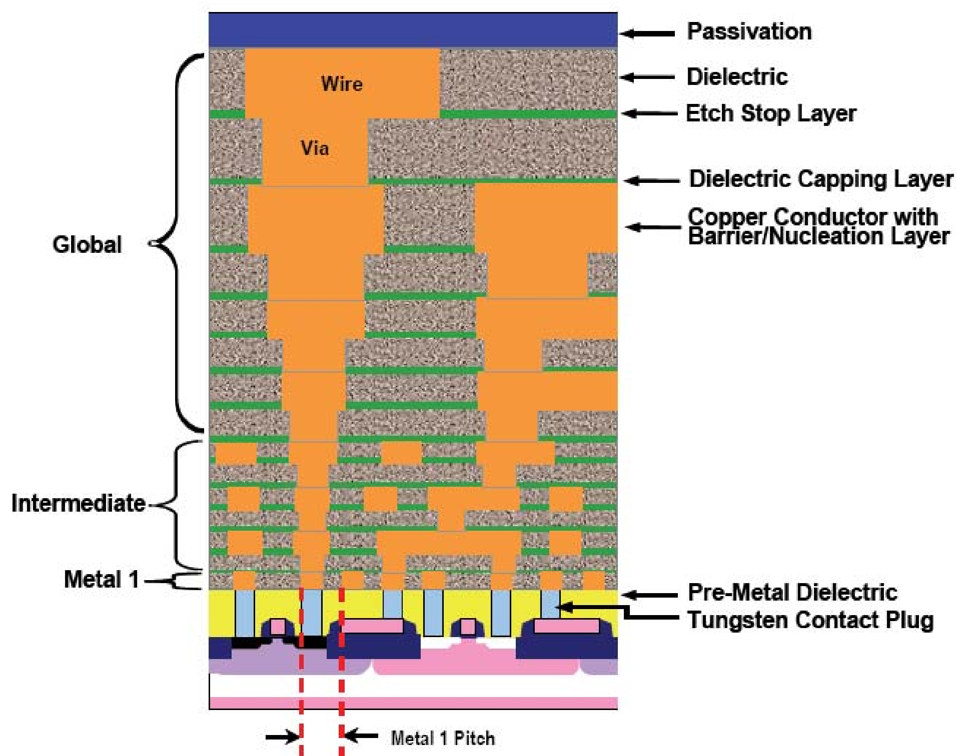

Figure. 1.3: Cross-section of hierarchical scaling of MPU device (from IRTS 2007).

Plasmas have been indispensable technologies for advanced materials processing in the manufacture of microelectronic devices. Leading-edge photolithography and plasma etching (PE) techniques have enormously shrunk the dimensions of transistors and enabled very large scale integration (VLSI) devices. In an integrated circuit (IC), individual transistors are connected by metallic interconnects which are separated by insulating dielectric in each layer. A typical cross-section of a Microprocessing Unit (MPU) device is shown in Fig. 1.3.[1.9] The metal-1 layer pitches, for example, are 60-70 nm for 45 nm technology, while upper layer metal pitches increase progressively to optimize integration density. The interconnects are formed by the dual damascene patterning of dielectric films.[1.10] The via-first dual damascene process is briefly illustrated in Fig. 1.4 and follows the following basic step: Step a) Dielectric layers are deposited with etching stop layers and a hard mask layer. A photoresist is spun onto the hard mask. The pattern for the via is then exposed and developed. Step b) The via is etched through the layer stack to the bottom etching stop layer. The patterned PR is then stripped. Step c) The photolithography process in step 1 is repeated. The pattern for the trench is developed. Step d) The trench is etched through the hard mask and the top dielectric layer to the embedded etching stop layer. Step e) Step The patterned PR is stripped. Step f). The bottom etching stop layer is etched.

Steps a) through f) can be repeated to build a 3-dimensional structure.

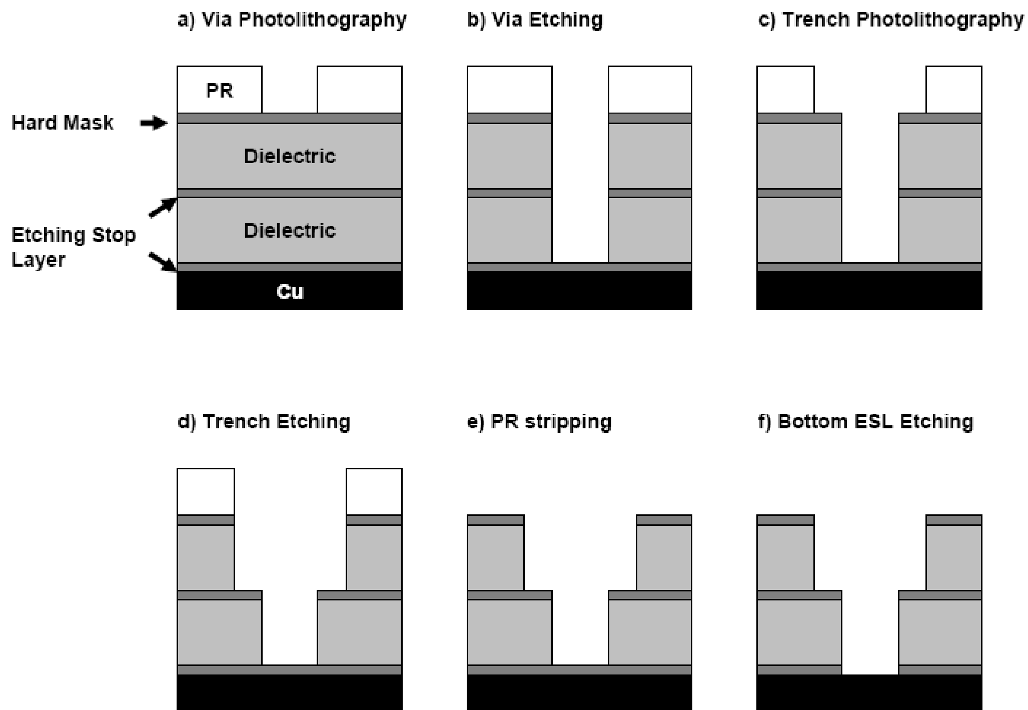

Figure 1.4: Via-first dual damascene patterning scheme for forming trenches and holes in dielectric materials that will be filled with metal to form the interconnecting wiring of an IC.

1.3 Challenges of Plasma Processing at Nanoscale Dimension

As the feature size of VLSI circuits is scaled down, metal lines in multi-layer structures, as illustrated in Fig. 1.3, are necessary to interconnect high-density circuits and enhance device performance. However, these designs emphasize the Resistance-Capacitance (RC) signal delay of interconnects. When the effective channel length was 0.25 µm, interconnect-related RC delay contributed half of the total delay and limited the speed of circuits. To reduce this issue, aluminum/silicon dioxide (Al/SiO_2) has been replaced by copper/low dielectric constant material (Cu/low *k*) as the scheme for interconnect technologies. The demand for *k* value of low dielectric materials constantly increases with the shrinking feature size. For the 45 nm node in

line with 2007 International Technology Roadmap for Semiconductor (ITRS), use of in interlevel insulator with an effective dielectric constant below 2.6 and width of 60 to 70 nm at the lowest metal level is required.[1.9]

Process integration of low *k* or ultralow *k* (ULK) dielectrics requires plasma etching of dielectric materials, stripping of the resist mask, and surface cleaning of PE-related residues without damaging the dielectric. Pores in the dielectric reduce the effective *k* value. The synthesis of most ULK materials utilizes processes where pores are generated by removal of one component of a dielectric film, e.g. of carbon-based groups for methyl silsesquioxane (MSQ) based silica.[1.7] Promising ULK candidate materials have an overall porosity of up to 50%, a pore size below about 2 nm and contain a large amount of residual carbon, e.g. methyl groups. For ULK materials, the diffusivity of reactants during plasma processing is dramatically increased, which can make materials unstable and give rise to unacceptable changes of ULK properties. If conventional plasma processes are used, e.g. O_2-based PR stripping process, the results can be a significant modification of nanoporous ULK materials. Typical problems seen with porous ULK films include carbon-loss from the trench/via sidewalls, and densification of the dielectric.[1.11,1.12] These modifications increase the overall dielectric constant from the goal of 2.6 or lower for 45 nm technology and also lead to a loss of CD control in the overall process sequence. Process-induced materials modification have become a key problem since, at the 45 nm node, the extent of plasma etching, stripping, and cleaning modified surface regions of the ULK material using current process technology amounts to a 20-30 nm effect and is therefore comparable to the dimensions of the smallest metal line level.

The overall goal of this work has been the rational design and validation of coordinated plasma etching, PR mask stripping and surface cleaning processes that are non-damaging to the ULK materials based on a fundamental understanding of the principal plasma surface interaction mechanisms as a function of process variables. Since the ULK modification caused by the PR stripping step of pattern transfer processes has been especially highlighted by ITRS, we emphasize studies of plasma ULK material surface/bulk interaction during PR stripping processes. It will provide the scientific basis for the design and further development of generic, mutually coordinated and consistent approaches to the pattern transfer, resist stripping and sidewall cleaning of ULK materials with goal of avoiding ULK damage and achieving an effective k value of 2.6 or lower at 45 nm lateral dimension. The use of CCP and remote plasma equipment, and an extensive coverage of relevant parameter space will enable rapid transfer of this knowledge into commercial equipments.

1.4 Facilities of the Laboratory for Plasma Processing of Materials

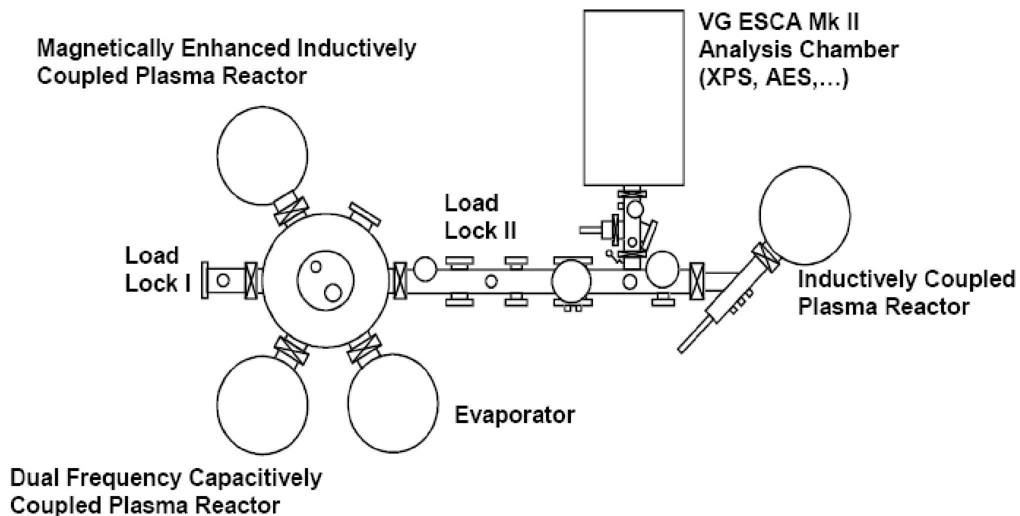

Figure 1.5: University of Maryland cluster system for plasma processing of materials

Fig. 1.5 shows the cluster system in the laboratory for plasma processing of materials, University of Maryland. Various reactors, including an inductively coupled plasma reactor and a dual frequency capacitively coupled plasma reactor described above, are connected in this cluster system with a surface analysis chamber (Vacuum Generator ESCA Mk II). The major scientific theme of this laboratory is the characterization and understanding of the processes at the plasma-material interface that control the properties of the material or structure that is ultimately produced. To understand the plasma properties, measurements are conducted to obtain information of ion current or radical density using a Langmuir probe and optical emission spectroscopy. These tools provide real time information on plasma properties and enhance the process control. For materials characterization, *in situ* ellipsometers are installed in the capacitively coupled plasma reactor to real-time monitor the surface modification of the sample. Samples are also characterized by *ex situ* techniques

including ellipsometry, XPS, SIMS, and SEM. The studies in this thesis involve many collaborative efforts from industries and laboratories throughout the world, in particular for the characterizations of the samples after plasma process done at University of Maryland (UMD). I am grateful to these collaborators. To emphasize their contributions, a summary of overall measurements involved in this thesis is listed below.

Measurement	**Method**	**Location**	**Information**
Optical emission Spectroscopy	*In situ*	UMD	Gas phase composition
Langmuir probe	*In situ*	UMD	Ion current density
Downstream mass spectroscopy	*In situ*	UMD	Downstream gas analysis
Ellipsometry	*In situ/ ex situ*	UMD	Multilayer thickness and optical properties
X-ray photoelectron spectroscopy	Air transfer	UMD	Chemical information
Time of flight secondary ion mass spectroscopy	*Ex situ*	ITC-irst	Chemical information
Scanning electron microscopy	*Ex situ*	Texas Instruments and IBM	Characterizations of structures

1.5 Thesis Outline

Unacceptable ULK sidewall damage for conventional O_2 plasmas lead us to the investigation of H_2 plasma stripping processes. In Chapter 2, H_2-based remote PR stripping processes were conducted in the ICP reactor with a gap structure setup and a heating plate assembly. The effects of gas additions of N_2 and Ar and substrate temperature varying between 200-275 °C on the ashing performance were evaluated with measured PR stripping rate and ULK materials damage. ULK sidewall

modifications introduced during prior CCP C_4F_8/Ar plasma etching process and its interaction with the H_2-based remote plasma is presented along with its impact on the ULK damage inflicted during the PR stripping process.

In situ PR stripping processes are attractive to industries because of high integratability with ULK etching processes. For *in situ* ashing in conjunction with a CCP reactor, H_2-based plasmas provide ashing rates much lower than practical values (since the use of a high temperature substrate is not possible). In Chapter 3, we examine the feasibility of CO_2 as an alternative source gas other than H_2 and O_2 for *in situ* PR ashing processes compatible with ULK materials. The parameters for CO_2 processing were varied to optimize the PR removal efficiency related to ULK damage introduction. The mechanisms of plasma material interactions are discussed.

In situ PR stripping, as a following step conducted in the CCP etching chamber, is subject to chamber memory effect due to the plasma etching step. In chapter 4, we studied how fluorine memory effects influence PR ashing rate and ULK modifications, respectively. The effect of the presence of PE-related modifications on material surfaces during the CO_2 *in situ* processing is also described.

Pore-sealing by etching byproduct deposited on ULK trench sidewall is a compelling strategy to protect ULK again plasma damage. In chapter 5, we examined the factors that determine the ability of PE-related residues/plasma surface modification of porous ULK sidewalls to protect the ULK materials during subsequent CO_2 *in situ* processes and, based on this knowledge, rationally designed a

ULK sidewall-protection approach in conjunction with coordinated plasma etching and PR stripping process.

Finally, chapter 6 summarizes the main conclusions of all these studies and chapter 7 outlines the future work.

Chapter 2: Influence of C_4F_8/Ar-Based and H_2-Based Remote Ashing Processes on Ultralow *k* Material Modifications

J. Vac. Sci. Technol. B 28, 2010

M.-S. Kuo, X. Hua, G. S. Oehrlein, A. Ali, P. Jiang, P. Lazzeri, and M. Anderle

ABSTRACT

We evaluated photoresist (PR) stripping processes that are compatible with ultralow dielectric constant (ULK) materials using H_2-based remote plasmas generated in an inductively coupled plasma (ICP) reactor. The materials used were 193 nm PR and nanoporous SiCOH-based ULK (JSR LKD 5109). PR ashing rates and ULK damage (carbon depletion) were measured for H_2, H_2/N_2, and H_2/Ar discharges as a function of substrate temperature over the range 200 to 275°C. We employed ellipsometry, x-ray photoelectron spectroscopy (XPS), optical emission spectroscopy (OES), and time-of-flight secondary ion mass spectroscopy (ToF-SIMS) for analysis. For our H_2 remote plasmas and a substrate temperature in the range 200 to 275 °C, the PR ashing rate varied from 270 to 880 nm/min, whereas 3 to 5 nm of ULK damage was measured for 20 sec remote plasma exposure. As a useful process metric, we defined *ashing efficiency* as the thickness of PR removed over the thickness of ULK simultaneously damaged. PR stripping processes can be optimized to an *ashing efficiency of* ~60 for substrate temperatures above 250°C, if pure H_2 discharges are employed. The addition of N_2 or Ar to H_2 did not improve the ashing

rate and, especially for N_2, such additions dramatically increased ULK damage. This resulted in reduced *ashing efficiency* for these cases.

To clarify the impact of etching/ashing process interactions on ULK modification, we exposed blanket ULK film to C_4F_8/Ar-based etching plasmas employing a dual frequency (40.68/4 MHz) capacitively coupled plasma (CCP) reactor. Plasma exposures of the ULK were performed utilizing a silicon roof which shielded the ULK film located underneath from direct ion bombardment. Since the aspect ratio of the small gap structure was selected to be equal to that of an actual trench structure, trench sidewall-like surface modifications induced by etching processes along with their impact on ashing damage that was introduced during a subsequent PR stripping process can be simulated and studied on blanket films with appropriate size. XPS revealed fluorocarbon (FC) deposition together with ~3 nm of ULK damage on the ULK film surface after the FC plasma etching process. Most of the deposited FC material was removed during a subsequent H_2-based remote plasma treatment at 275 °C. The influence of surface modifications introduced by the prior C_4F_8/Ar-based etching exposure on hydrogen permeation of the ULK material during a subsequent H_2 remote plasma ashing process was studied by substituting deuterium (D_2) for H_2 in the remote plasma process and performing ToF-SIMS analysis. ToF-SIMS depth profiling of ULK films exposed to D_2 plasma showed reduced D permeation in the ULK films with C_4F_8/Ar etching plasma exposure relative to that without such FC plasma exposure.

Photoresist patterned ULK structures were also processed, employing the same ashing conditions after prior FC plasma etching in the CCP reactor. The ULK

damage results measured with trench structures were consistent with the above findings obtained with blanket ULK films.

2.1 Introduction

The International Technology Roadmap for Semiconductors (ITRS) 2006 update for Interconnects[2.1] discusses that an interlevel metal insulator with a bulk dielectric constant k = 2.1 to 2.4 [ultralow k (ULK) materials] is required for a line width below 40 to 50 nm at the lowest metal level. Nanoporous silica-based dielectric materials are generated by thermal or ultraviolet (UV) decomposition of sacrificial organic components from the dielectric films as deposited.[2.2] Most of the silica-based ULK materials contain Si bound methyl groups (Si-CH_3), referred to as SiCOH. The Si-CH_3 terminates continuous silica structures and stabilizes the nanopores. Process integration of ULK dielectrics requires plasma etching of dielectric materials, stripping of PR masks, and surface cleaning of plasma etching-related residues without damaging the dielectrics. SiCOH dielectric materials are susceptible to damage from plasma species which typically destroy Si-CH_3 bonds and restore the porous dielectric to a SiO_2-like structure with high k value.[2.3,2.4] Process-induced materials modifications have become a key problem since, at the 45 nm node, the extent of plasma etching, stripping, and cleaning modified surface regions of the ULK material using current process technology amounts to a 20-30 nm effect and is therefore comparable to the dimensions of the smallest metal line level (see Fig. 2.1).

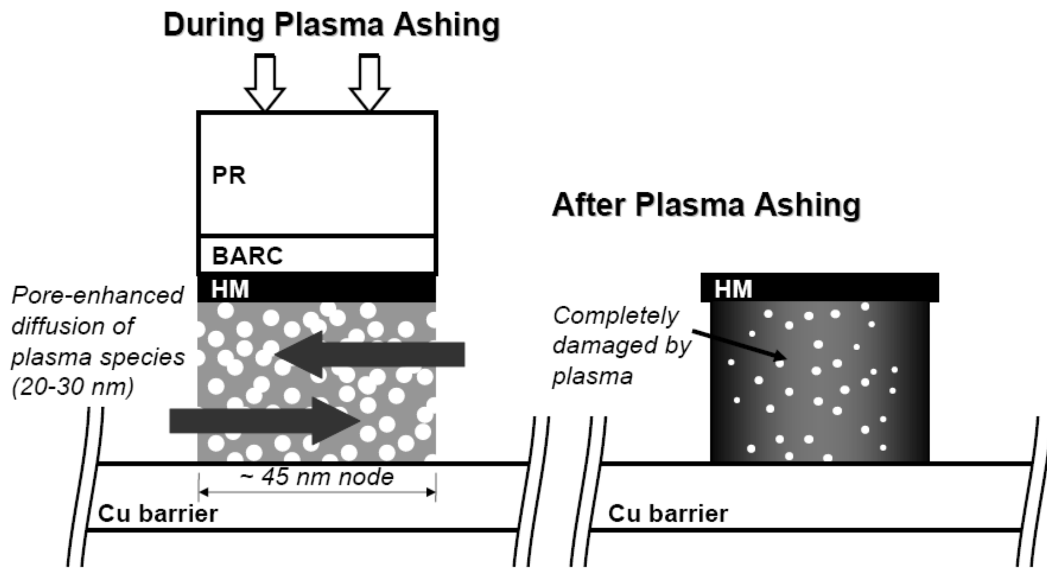

Figure 2.1: Illustration of ULK damage issue introduced by plasma-based PR stripping during the fabrication of an interconnecting structure.

It is well known that both remote (isotropic) and *in situ* (anisotropic) plasma stripping of the PR mask using conventional O_2 plasma leads to unacceptable ULK damage.[2.5] Chemistries other than oxygen must be considered for PR stripping processes that are compatible with ULK materials.[2.6-2.9] *In situ* PR stripping using CO_2 plasmas has been studied in a capacitively coupled plasma (CCP) etcher; the results will be presented in Chapter 2 and Chapter 3.[2.10] The current article focuses on remote processing, which eliminates device degradation from energetic ion bombardment. In previous work,[2.3,2.11] we have shown that hydrogen (H_2) remote plasma ashing of PR in our reactor introduced little ULK damage while providing a satisfactory ashing rate of PR materials for a substrate temperature near 300 °C. This indicates that activated hydrogen species may act very differently when attacking carbonaceous PR material on the surface of a substrate or when interacting with CH-

bonds inside the nanoporous dielectrics. The selective attack of PR material in H_2 plasmas can be used as a basis for formulating ULK-compatible PR ashing gas mixtures. Since the use of pure H_2 discharge may not be desirable due to its low ashing rate relative to O_2 discharge, we investigated the performance of gas mixtures that included H_2/N_2 and H_2/Ar. The PR stripping (ashing) rate and ULK materials damage introduced at substrate temperatures in the range 200-275 °C were measured. Surface chemistry characterizations of ULK material, along with plasma compositional analysis, allowed us to obtain insights into plasma/ULK interactions and correlate these data with the results of process performance studies.

For realistic pattern transfer processes, PR stripping takes place after ULK plasma etching. Fluorocarbon (FC)-based plasmas are employed for plasma etching of silica-based dielectrics, and produce FC film coverage at ULK trench sidewalls.[2.12-2.14] We examined C_4F_8/Ar plasma etching-related ULK surface modifications and their interactions with H_2-based remote plasma processes during PR removal. Macroscopic blanket ULK films were coated with materials analogous to sidewall films using a small gap structure approach.[2.12,2.13] These studies enabled surface chemical characterization of C_4F_8/Ar etching-induced ULK modifications and allowed us to determine their influences on ULK damage production during PR stripping.

2.2 Experimental Setup and Procedures

Nanoporous silica (JSR LKD 5109), a spin-coated methyl silsesquioxane (MSQ)-based dielectric with $k = 2.2$, was used as the ULK material.[2.15-2.17] The nanopores are created as a result of the removal of the polymeric porogen from the matrix. The pore diameter is about 2~3 nm, and overall porosity is above 30%.

H_2-based remote plasma ashing processes were performed in the ICP reactor (see Fig. 1.1) with a gap structure setup. The discharge conditions were 1000 W 13.56 MHz source power, a pressure of 100 mTorr and total gas flow rate of 50 SCCM. Samples were mounted on the center of a 15 cm diameter circular heating plate assembled on the 300 mm diameter of the bottom electrode.[2.11] For remote plasma processing, a 15 cm diameter bare silicon roof, supported by two aluminum spacers, was placed above heating plate and kept the samples from directly exposing to plasma. The schematic of the gap structure is illustrated in Fig. 2.2. Due to high aspect ratio of the gap structure, ions were effectively de-ionized by frequent collision with surfaces on the way to sample; importance of neutral species relative to ions was hereby emphasized on sample surface. We believe that the results obtained with this setup captures essential elements of the plasma surface interaction that would be seen for a commercial remote plasma reactor. In this work, the gas chemistries of H_2/N_2 and H_2/Ar were examined, with the ULK substrate temperature varying between 200-275 °C.

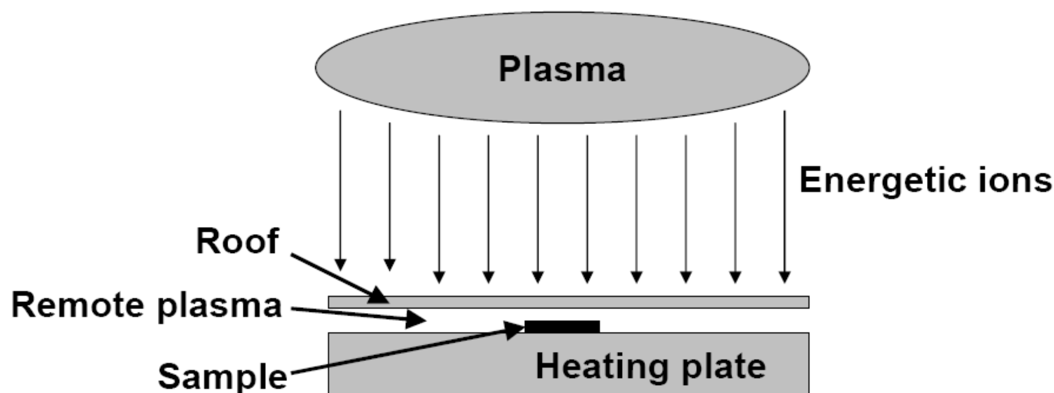

Figure 2.2: Schematic of the gap structure. Samples placed in the region shielded by the roof primarily interact with neutral, the remote plasma processing regime.

For the etching/ashing process interaction studies, a dual frequency (40.68 /4.0 MHz) capacitively coupled plasma (CCP) reactor (see Fig. 1.2) was employed for ULK etching. A gas mixture consisting of C_4F_8/90%Ar (total gas flow of 40 SCCM) was employed, to which additional gas flows of either 2 SCCM O_2 or 4 SCCM N_2 were added for specific experiments. These etching plasma gas compositions are denoted as $C_4F_8/Ar/O_2$ and $C_4F_8/Ar/N_2$. Other parameters were a gas pressure of 30 mTorr and 200 W rf (40.68 MHz) power applied to the top electrode. The bottom electrode was biased, using 100 W rf (4 MHz) power and controlled at 10 °C. The self-bias voltage was about -300 V.

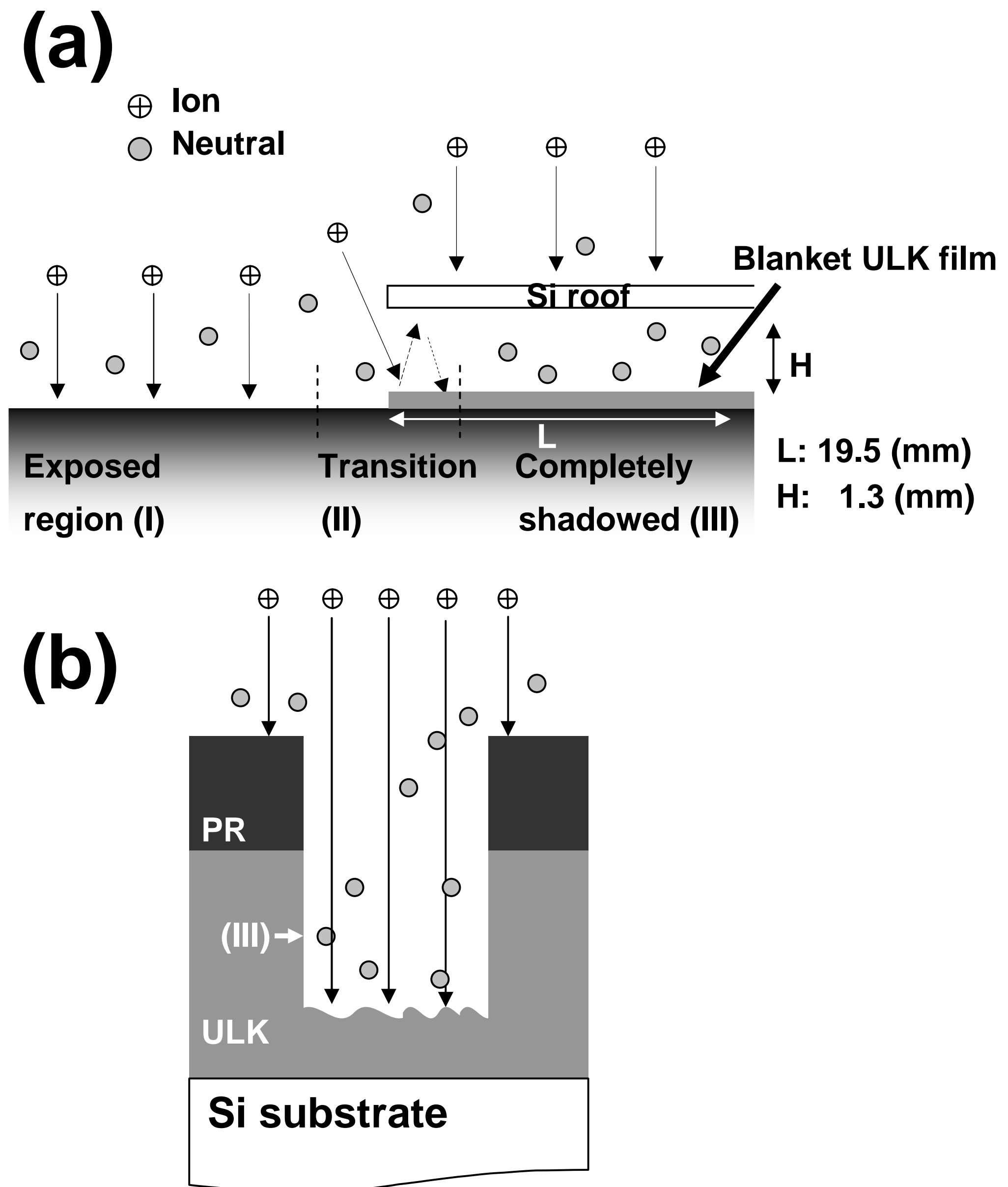

Figure 2.3: (a) Schematic of the small gap structure used in this work. (b) Simulation of ULK sidewall with blanket samples in region (III) (*Drawings not to scale*).

During actual plasma etching processes, ULK surfaces at vertical sidewalls see little direct ion bombardment and primarily react with plasma neutrals. The reactivity of the incident particle flux depends on the aspect ratio (A/R) of trench/via

structures because this determines the number of collisions with sidewalls. The dynamic random access memory (DRAM) interconnect technology requires a contact A/R >20 for 45 nm technology.[2.1] For ULK characterization, a gap structure, illustrated in Fig. 2.3, was assembled using a bare silicon (Si) roof with a width of 39 mm and a height (H) of 1.3 mm supported by two Si spacers.[2.13] The ULK samples were located underneath the center of the Si roof. The blanket ULK films located in the small gap were shielded from direct ion bombardment by the silicon roof. The distance of the sample location relative to the roof edge (L) was 19.5 mm, giving an aspect ratio of the gap structure of about 15. Because the A/R of the gap structure was selected to be equal to that of the actual trench structure, trench sidewall-like surface modification induced by plasma-etching processes can be simulated and studied using blanket ULK films.

These ULK films were then exposed to H_2-based remote plasmas in the ICP reactor under selected ashing conditions. For these etching/ashing combined experiments and their ashing controls, a Kapton film was attached to the inner side of the quartz window in the ICP reactor to prevent production of inadvertent oxygen from window sputtering[2.18,2.19] during the remote plasma processes. The interaction of the plasma with this film, i.e. consumption of plasma species due to its reaction with the Kapton, led to a lowering of reactive plasma species relative to conditions examined in prior work.[2.3,2.11] In parallel, trench ULK structures were processed and examined using identical process conditions.

The glow of H_2/N_2 plasmas produced in the ICP reactor was characterized using optical emission spectroscopy (OES). The density change of plasma species with different H_2/N_2 gas mixture ratios was estimated by Ar actinometry.[2.20]

For ULK materials analysis, a variety of complementary materials characterization techniques were used to characterize thickness, chemical composition on the surface and in the depth of blanket films, and to obtain micro images of stacked structures. These techniques included single wavelength ellipsometry, x-ray photoelectron spectroscopy (XPS), time-of-flight secondary ion mass spectroscopy (ToF-SIMS), and scanning electron microscopy (SEM). Film thickness was measured by a single wavelength laser ellipsometer in the polarizer-compensator-sample-analyzer (PCSA) configuration with a 632.8 nm He/Ne laser source beam incident at an angle near 73° from the surface normal. XPS surface analysis was performed in a Vacuum Generators ESCA Mk II analysis chamber. Using a nonmonochromatized Mg $K\alpha$ x-ray source (1253.6 eV), photoelectrons were emitted into the analyzer with a slit size of 15 mm × 6 mm. Photoemission intensities were acquired at 90° takeoff angles and spectra obtained at dwell time of 500 ms and pass energy of 20 eV. ToF-SIMS (Ion-TOF, ToF-SIMS IV) depth profiling utilized Cs^+ at 1.5 keV as the sputtering beam, electron flooding for charge compensation, and Ga^+ at 15 keV as the primary probe. Samples for depth profiling were sputter-coated with a thin layer of gold. The depth crater was calibrated by a mechanical profilometer (KLA TENCOR, P15). SEM (Hitachi S4800) images were acquired using an electron beam acceleration voltage of less than 2 kV to avoid dimension distortion and degradation of measurement accuracy.

The damage thickness of ULK presented in this work was quantified using the hydrofluoric (HF)-staining approach.[2.21] The plasma-exposed ULK is dipped into 1% diluted HF acid solution, which selectively etches the carbon-depleted ULK layer at the surface. The time for wet etching was 15 sec. The thickness change of ULK films before plasma exposure and after HF-dipping was measured by ellipsometry using a single layer model and is reported as plasma damage thickness. In this work, the material and discharge conditions can be well reproduced and the uncertainty of reported ULK damage depth for different processing conditions was primarily attributed to errors from the DHF approach. The coefficient of variation defined as the standard deviation divided by the mean was within 6 % for our experiments. The difference of ULK damage depth reported for a variety of process conditions is statistically significant.

2.3 Results and Discussion

2.3.1 Blanket materials exposed to remote discharges

A. Ashing efficiency

Blanket PR and ULK films were exposed to H_2-based remote plasmas at substrate temperatures between 200-275 °C. Results of PR ashing rate and ULK damage measurements are summarized in Fig. 2.4(a) and 2.4(b). Both PR ashing rate and ULK damage increase strongly with increasing substrate temperatures. It is desirable to maximize the PR ashing rate relative to the introduction of ULK damage. This suggests defining ashing efficiency (AE) as the thickness of PR removed divided by the ULK damage layer thickness for a given amount of process time. This

parameter is shown for a process time of 20 sec in Fig. 2.4(c). Relative to pure H_2 remote plasma, the addition of N_2 or Ar did not improve PR ashing efficiency. The addition of N_2 to H_2 dramatically increased ULK damage for the substrate temperatures examined. The performance of pure N_2 remote plasma is also included as a reference in Fig. 2.4. N_2 remote plasma displays a relatively low ashing rate and very high ULK damage. In general, AE was improved by increasing the substrate temperature. Pure H_2 discharges provided the highest values of AE (~60) and simultaneously (at 275 °C) an ashing rate that approached 900 nm/min for the conditions employed here.

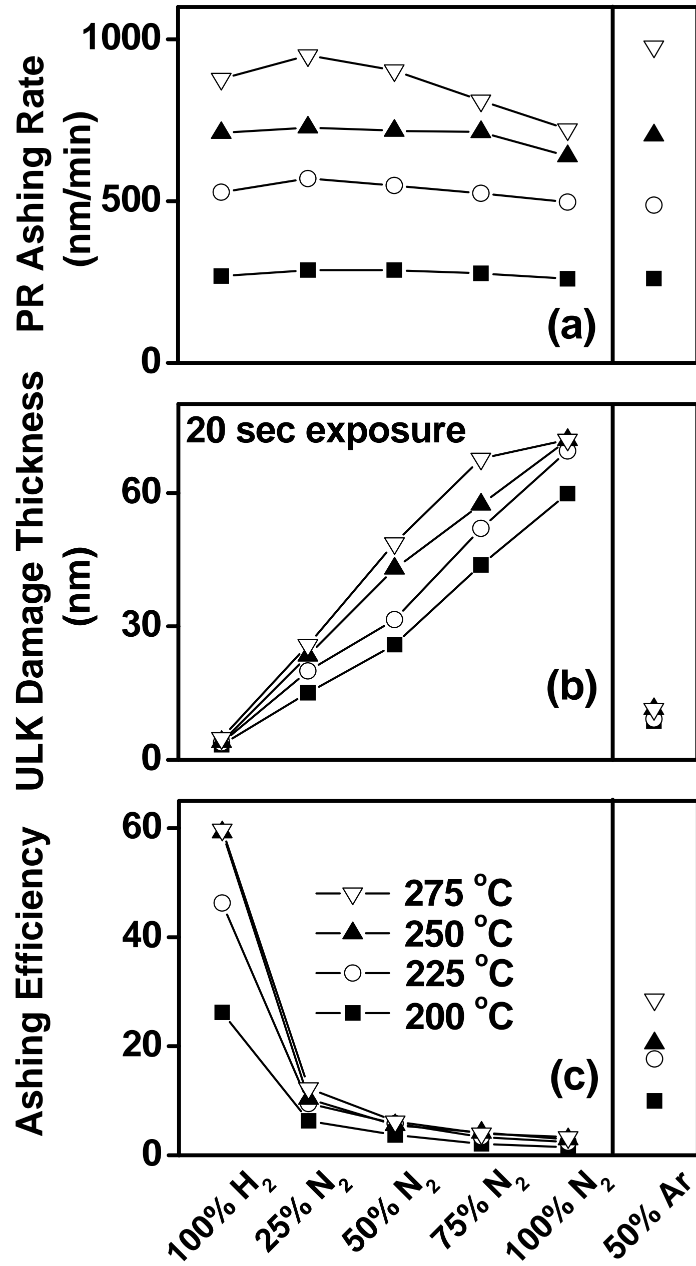

Figure 2.4: (a) PR ashing rate, (b) ULK damage thickness, and (c) AE for 20 remote plasma processing at various substrate temperatures and plasma chemistries. ULK damage thickness was evaluated using 1% HF solution/15 s dipping method. AE is defined as the thickness of PR layer removed divided by the thickness of ULK material damaged during the same process step (20 s plasma exposure in this work).

B. Composition of H_2/N_2 plasmas

The H_2/N_2 plasmas in the glow region can be characterized by optical emission spectroscopy (OES). As an illustration, the spectrum obtained with H_2/N_2 (1/1) plasma is displayed in Fig. 2.5. The identification of molecular and atomic spectra is based on *The Identification of Molecular Spectra*[2.22] and *NIST Atomic Spectra Database.*[2.23] In Fig. 2.5, the N_2 first ($B^3\Pi_g \rightarrow A^3\Sigma_g^+$) and second ($C^3\Pi_u \rightarrow B^3\Pi_g$) positive systems can be seen. Distinct emission lines at 656.3 nm and 486.2 nm are identified as H atom emission lines (H_α: n=3→2 and H_β: n=4→2 of the H Balmer lines). The emission at 336 nm is attributed to NH (imidogen) ($A^3\Pi \rightarrow X^3\Sigma^-$). For N atoms, the emission line at 821.6 nm ($3p^4P^0 \rightarrow 3s^4P$) was the only observable N line with a high signal/noise ratio. The species interacting with the PR and ULK materials in a remote plasma environment are long-lived neutrals produced in the plasma. In the work of Amorim *et al*. in H_2/N_2 DC plasmas,[2.24] it was found that NH radicals can be detected in the glow region, but not in the post-glow region; they concluded that NH radicals are quickly extinguished by reactive collisions with gases and chamber walls. Although NH can be detected in the glow region by OES, its significance to material reaction in the remote region is neglected. H and N atoms in their ground state are the most populated active species in H_2/N_2 plasmas. Since their wall loss probabilities in H_2/N_2 systems are very small,[2.25,2.26] we expect that their flux, which was incident at the surface of the materials in the remote plasma environment, was strongly related to densities in the glow region. The density change of H and N atoms in the glow region for different H_2/N_2 mixtures was estimated by Ar actinometry. When 3% noble Ar was added into the feed-in gas, Ar emission lines at

750.4 nm and 811.6 nm can be detected. Optical emission lines of H at 656.3 nm, N at 821.6 nm, and N_2 at 357.7 nm in the second positive system are selected for actinometry with the Ar line at 811.6 nm. At first, their intensities are collected as a function of H_2/N_2 mixtures and shown in Fig. 2.6(a). Ar emission intensity with increasing N_2 content in H_2/N_2 mixtures indicates decreasing excitation efficiency of Ar, which might be related to the change in electron temperature. The threshold energies of electron-impact optical excitation are 13.1 eV for the selected Ar line and 11.1 eV for the N_2 second positive system. According to the linear relationship of N_2 emission with increasing N_2 content in H_2/N_2 mixtures in Ar actinometry [see Fig. 2.6(b)], it can be confirmed that the optical emission of N_2 and also H and N with threshold energies of 12.1 and 11.8 eV in our H_2/N_2 plasmas was excited by the same electron group with the selected Ar line. Although atomic species such as H and N in optical excitation states may not come only from direct electron impact excitation but also from dissociative excitation, the high threshold energies for dissociative excitation [18.1 and 24.3 eV for H_2 and N_2 (Ref. 2.27), respectively] likely minimized their contribution. The fidelity of actinometry to quantify density changes of H and N atoms can be ensured.

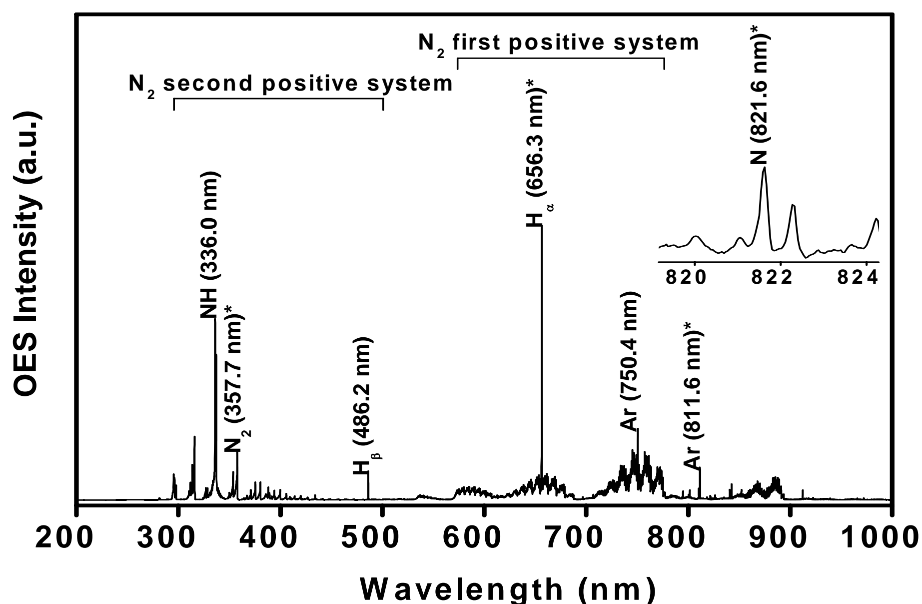

Figure 2.5: OES for H_2/N_2 (1/1) plasma in ICP reactor. 3% Ar was also added to the gas mixture to enable application of Ar actinometry. The emission lines selected for Ar actinometry are indicated with a * symbol.

If N_2 was added into H_2 plasma, in order to maintain constant total pressure, the amount of H_2 molecules in the reactor would be relatively reduced. One could expect fewer H atoms to be produced. However, Ar actinometry indicates that H atom density in the H_2/N_2 plasma peaked at about 30% N_2 addition. This is likely a result of excitation of N_2 to metastable states by electron impacts. The quenching of these metastable states provides additional dissociative channels, which significantly increases the H_2 dissociation ratio.[2.28] With the interplay between number density and the dissociation ratio of H_2 molecules, the increase of H atoms can be observed with the addition of N_2 to our plasmas from 0-50% N_2 in the N_2+H_2 plasma. Additionally, N atoms in the glow region were generated from dissociation of N_2. The efficient

quenching of vibrational states of N_2 by collisions with H_2 leads to the loss of N_2 population densities in the tail of the vibrational distribution (for v≥ 25) and reduces the dissociation of N_2 from vibrational-translational (V-T) energy exchanges.[2.24,2.29] Compared with N_2 content in H_2/N_2 mixtures, the increase of N atoms with the N_2 addition was relatively slow. In other words, the dissociation of N_2 in plasmas was suppressed by H_2 molecules.

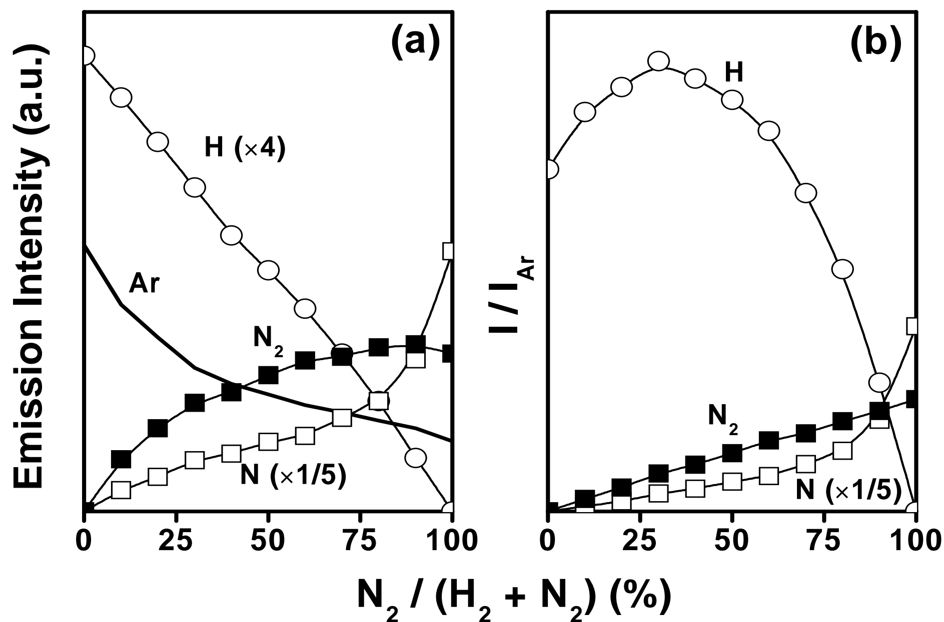

Figure 2.6: (a) Optical emission intensities of selected spectral lines detected for H_2/N_2 discharges. In (b), the emission line/Ar (811.6 nm) intensity ratios are shown as a function of the nitrogen content in the H_2/N_2 mixtures fed to plasma. The Ar line intensities were recorded using 3% argon in the discharges.

C. Remote plasma/ material reaction

a. Apparent activation energy

The effect of temperature on a chemical reaction reflects the activation energy (E_a) of the reaction. To obtain E_a of PR ashing and ULK damage introduction with remote plasma exposure, Fig. 2.4(a) and 2.4(b) were converted into Arrhenius plots and are shown in Fig. 2.7(a) and 2.7(b). E_a can be examined for each by the slope of straight line fits. Results for pure H_2, H_2/N_2 (1/1), and pure N_2 are displayed in Fig. 2.7(a) for PR ashing and 2.7(b) for ULK damage. In the temperature range of 200-275 °C, the linear fit suggests a constant E_a for ULK damage while the change of the slopes of the linear fit indicates a decreasing E_a of PR ashing with increasing temperature. Rather than activation energy, we prefer to use "apparent" activation energy since the measured rates are due to a sequence of reaction steps involving reactants in the remote plasma environment arriving at the surfaces of the materials and leading to PR removal and ULK damage. In our ashing processes, the removal of PR material was not only caused by its reaction with plasmas but also by thermal decomposition on elevated temperature substrates. Polymer typically starts to decompose at temperatures above 200 °C.[2.30] PR films after being loaded into the reactor under atmosphere remained on the elevated temperature substrate for approximately 30 minutes while evacuating the vessel to its designated base pressure. With 400 nm of initial thickness, more than 100 nm of thickness may be lost due to thermal decomposition on a substrate at elevated temperature during pump down. The ashing rate here was defined as total thickness loss divided by 20 sec of plasma exposure time. As a result, the contribution of thermal decomposition to ashing rate

shown in Fig. 2.4(a) can be more than 300 nm/min. Since thermal decomposition shows a different dependence than plasma/material interaction on temperature, it may explain the change of apparent E_a with temperature.

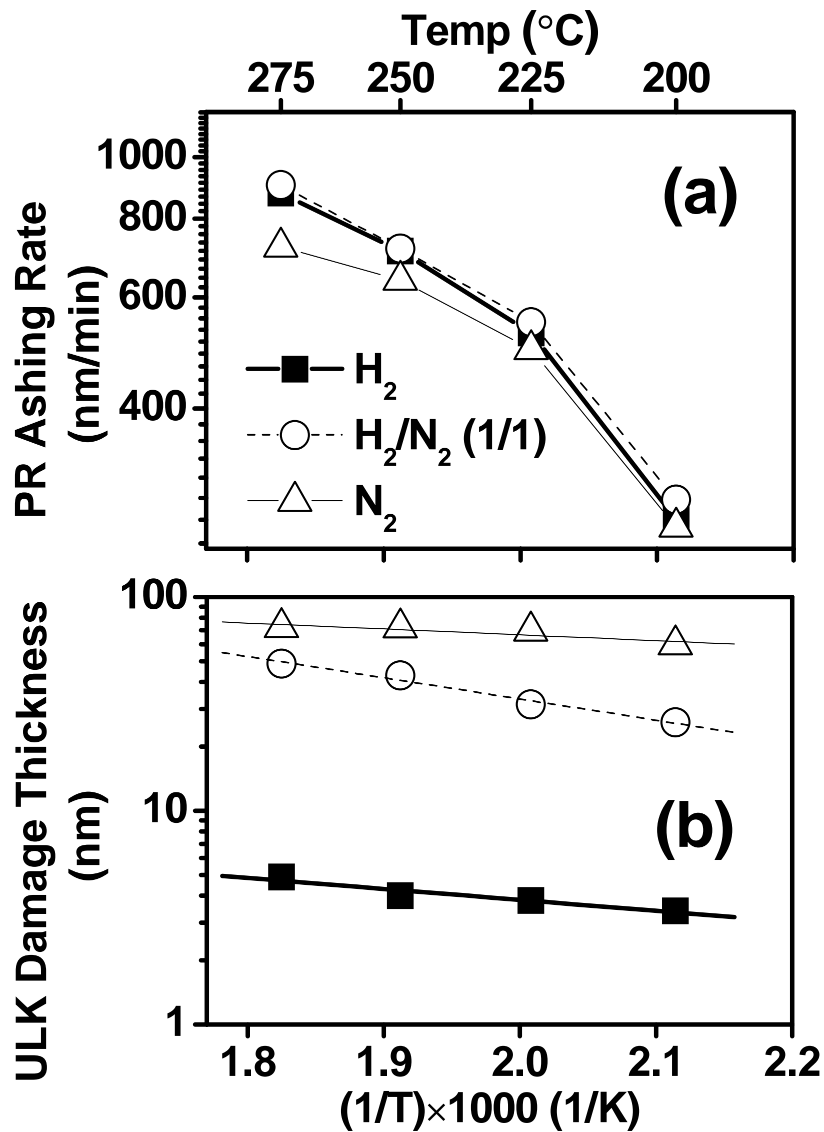

Figure 2.7: Arrhenius plots of (a) PR ashing rate and (b) ULK damage thickness for remote plasma processing. Results obtained with pure H_2, H_2/N_2 (1/1), and pure N_2 plasma chemistries are displayed.

The ULK damage is caused by the penetration and reaction of plasma reactants within the dielectric material. Therefore, the growth of the damage thickness during the plasma exposure may be expected to be limited by reactant diffusion in two ways: (1) the required diffusion path for plasma reactants such as H and N increases with damaged layer thickness; (2) the damage-derived densification reduces the diffusivity and flux of plasma reactants inside the porous material. The apparent activation energies E_a measured here for both ULK damage introduction and PR cannot be easily interpreted due to the contribution of multiple processes. However, these quantities are useful process optimization parameters since they express the relative temperature sensitivities of ULK damage and PR ashing. The data collected from our ashing processes indicates an apparent activation energy E_a ~0.35 eV for PR ashing, which is higher than the apparent activation energy E_a ~0.15 eV obtained for ULK damage introduction. As the substrate temperature is increased, the PR ashing rate grows more rapidly than ULK damage introduction, consistent with the observation of a greater AE when higher substrate temperatures were employed for processing. However, as the substrate temperature is increased, the apparent activation energy for PR ashing decreases and approaches the apparent activation energy for ULK damage introduction. This is in agreement with our observation that AE saturated for substrate temperatures greater than 250 °C.

b. Characteristics of H_2/N_2 mixture remote plasmas in materials processing

Even though thermal decomposition contributed to PR removal in our ashing process, the loss of PR thickness due to thermal decomposition for a given substrate temperature is assumed to be the same for different remote plasma chemistries. N_2 addition to H_2 can enhance the PR ashing rate for less than ~50% N_2 [see Fig. 2.4(a)]. The increase of the ashing rate upon N_2 addition reflects the increase of the H density [which peaks at ~30% N_2 addition as per Fig. 2.6(b)] seen in the OES measurements. However, the increase of the PR ashing rate was far less than the simultaneous increase of the ULK damage thickness [see Fig. 2.4(b)].

To study the interaction of porous ULK with H_2 remote plasma, Lazzeri *et al.*[2.31] exposed ULK to D_2 remote plasma and characterized the D depth profile by ToF-SIMS. They found that D from the remote plasma replaced intrinsic H in the original ULK films, but the total amount of H + D remained unchanged. This replacement reaction between D from plasma and intrinsic H in the films confirms the finding that H species from the plasma can penetrate into the ULK films and replace H without changing the stoichiometry of the ULK films. For N_2 remote plasma, the interaction with ULK has different consequences and can lead to significantly more ULK damage relative to H_2 remote plasma exposure.

For the data described up to this point, ULK damage was determined by the HF-staining method after different processing conditions. XPS was employed for the ULK surface chemistry studies to be described next. Although the probing depth of XPS was limited to ~10 nm, and most experimental conditions used induced deeper ULK modification, the surface chemical bonding information can provide insight into

the mechanism of ULK damage. ULK was exposed to remote plasmas with the substrate at 22 °C [room temperature (RT)]. The minimum amount of ULK damage at RT can be a baseline for the study of temperature effects when compared with results at 275 °C, at which the best AE was obtained. Completed XPS spectra including C 1*s*, Si 2*p*, O 1*s*, and N 1*s* of untreated ULK and ULK exposed to H_2, H_2/N_2 (1/1), and N_2 remote plasmas at RT and 275 °C are displayed in Fig. 2.8. Integrated intensities of C-Si/C-C peaks in C 1*s* and total Si 2*p* and O 1*s* were divided by their initial intensities of untreated sample and labeled by the peaks. The reduction of C-Si/C-C intensity indicates the ratio of carbon depletion caused by plasma in the top 10 nm surface region. At RT, a greater amount of ULK damage is seen in pure N_2 compared to pure H_2 remote plasma. For H_2/N_2 (1/1), the ULK damage level was in between but much less than that of pure N_2. This result can be related to our gas phase characterization, which showed that N atom density was suppressed with H_2 molecules. This supports the picture that N atoms are primarily responsible for ULK damage for N_2-containing remote plasmas.

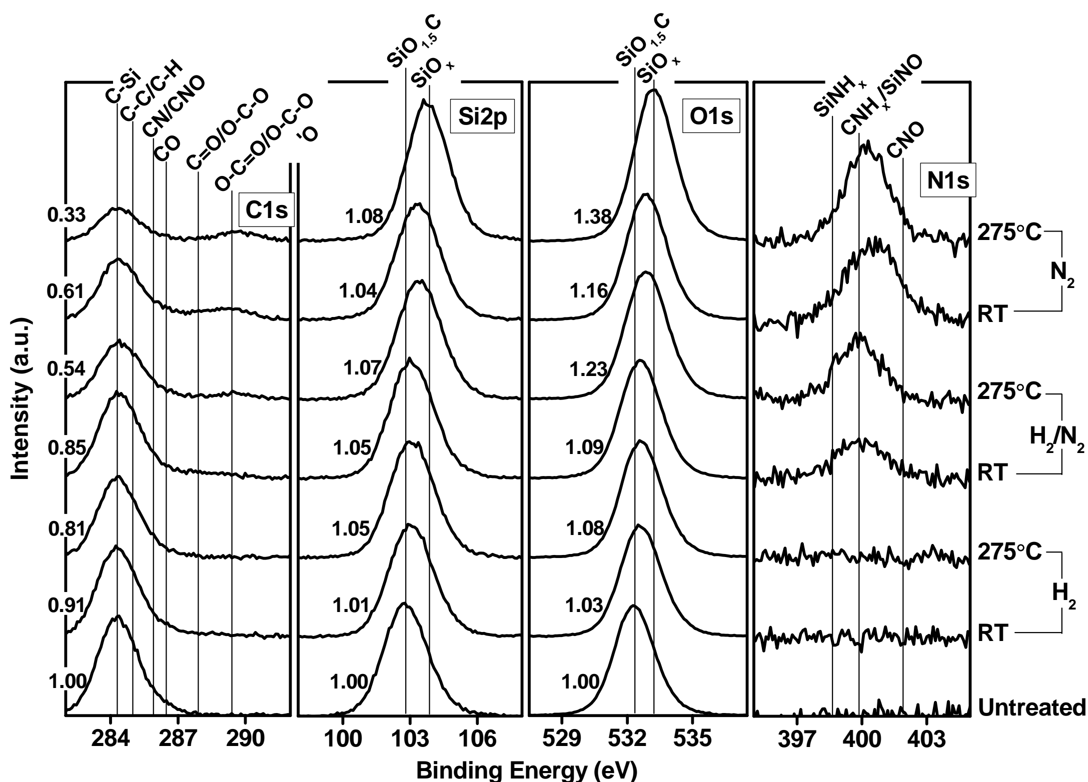

Figure 2.8: C 1*s*, Si 2*p*, O 1*s*, and N 1*s* XPS spectra of untreated ULK and ULK exposed to pure H_2, H_2/N_2 (1/1), and pure N_2 remote plasmas at RT and 275 °C for 60 s. The numbers listed next to the peaks of the C 1*s*, Si 2*p*, and O 1*s* spectra are the integrated C-Si/C-C, Si, and O peak intensities divided by the values measured for untreated ULK.

At RT, the ULK damage level introduced in H_2/N_2 and pure H_2 plasma was similar. As the temperature was raised to 275 °C, the damage for H_2/N_2 (1/1) plasma increased to a level comparable to pure N_2 plasma, while the ULK damage after pure H_2 plasma exposure remained minor. As carbon was depleted from the ULK, the Si and O signals were changed. The shift of the Si 2*p* and O 1*s* binding energies was consistent with the depletion of carbon. The increase of O 1*s* intensities indicates that the site of depleted carbon was replaced with O when damaged ULK films were

exposed to air. For N_2-containing plasmas, incorporation of N in ULK can be observed in the N 1*s* spectra. The weak N 1*s* intensities have been explained by Lazzeri *et al.*,[2.32] who showed that N-related intermediate compounds were apparently converted into volatile species and lost from the surface.

After pure N_2 plasma exposure of ULK, -NO bonding can be observed as a shoulder on N 1*s* peak at about 401.9 eV binding energy (BE) as observed in Fig. 2.8. Oxygen incorporation into the ULK material is also indicated in the C 1*s* spectra, which showed C-O, C=O, O-C-O, O-C=O and O-(C-O)-O moieties between 286 and 289 eV BE (Fig. 2.8).[2.33] Residual oxygen existed in H_2/N_2 plasma. A possible source of oxygen may be the oxygen sputtered off from the quartz (SiO_2) window of the apparatus by plasma ions. Since heavier N_2 ions have a higher sputter yield than H_2, the residual O content of the discharge may be expected to increase with N_2 content in the H_2/N_2 plasma. The O content may also come from the residual H_2O in vacuum chamber, which was dissociated during the operation of N_2-containing discharges.

c. Reaction mechanism and influence on ashing efficiency

Based on the data of Grill *et al.*[2.34] and Lazzeri *et al.*,[2.31] we assume that, for H_2 remote plasma, replacement of intrinsic H in the ULK film with H atoms from the plasma takes place, while simultaneously, no significant carbon depletion by formation of volatile CH_4 with H occurs. For N_2 remote plasmas, N atoms could deplete carbon in the ULK by directly cleaving bonds between Si and methyl ($-CH_3$) groups. Nitrogen atoms can also bond with carbon in the ULK to form –CN

moieties,[2.32] which may subsequently be converted into volatile HCN and lead to additional carbon loss. Lazzeri's ToF-SIMS depth profiling data[2.32] also indicates that the chemical modification caused by D_2/N_2 (3/1) plasma relative to pure N_2 plasma was less intense but the modified layer was broader. This is consistent with the idea that high film densification is caused by the greater reactivity of a pure N_2 plasma which reduces the flux of plasma reactants into the porous ULK and restricts the plasma modification depth by causing more significant surface densifications. Our HF-staining approach consistently showed smaller ULK damage thickness for H_2/N_2 gas mixtures relative to pure N_2. It suggests that HF (1%, 15 sec) may not be able to etch and resolve the tail portion of the ULK modified layer with a minor chemistry change. However, since the chemical modification of the extended layer was relatively minor and also the thickness extended beyond the dimension of ULK in the actual trench structure used (< 45 nm), our findings of relative ULK damage thickness for different H_2/N_2 chemistries determined after HF-staining appear reasonable. The generation of N atoms is reduced relative to N_2 and will result in lower ULK damage [see Fig. 2.4(b)].This leads to a gradual improvement of AE for increasing H_2 in H_2/N_2 gas mixtures relative to using pure N_2. The AE was dramatically increased only if no N_2 was added.

2.3.2 Etching/ashing combined experiments

The ULK damage in etching/ashing combined experiments and in the ashing controls at 275 °C substrate temperature are shown in Fig. 2.9. As indicated in the experimental setup section, the densities of ashing plasmas were reduced for the

studies of etching/ashing process interactions. Thus, the ULK ashing damage in both H_2 and H_2/N_2 ashing control experiments which consisted of ashing by itself (see Fig. 2.9) was reduced as compared to the results in Sec. 2.3.1 [see Fig. 2.4(b)]. Additionally, the damage to ULK material resulting from etching/ashing combined experiments was higher than in the ashing control experiment. Here we examined the question: What caused the additional damage found in the ULK after a plasma etching/ashing process sequence? The interactions that occurred during remote plasma ashing processes were thermally activated. If this additional damage had already been established after the CCP etching process, it should be independent of ashing process temperature. Alternatively, one could consider a mechanism where the additional damage was caused by the interaction of etching-induced surface modification with the ULK during the ashing process. In this case, for a thermally activated interaction process, we would expect that the magnitude of the additional damage would show a dependence on the substrate temperature of the ashing processes. For the sake of conciseness, the results were not shown here. However, our data showed that for both a) plasma etching/ashing process sequences and b) for ashing control experiments ULK damage increased with ashing temperature, but that the additional ULK damage introduced for plasma etch/ashing process sequences was constant and independent of ashing temperature. This proves that this additional damage was created after the CCP etching process, implying that C_4F_8/Ar-based CCP etching process introduces ULK damage in sidewalls during etching processes. The damage caused by etching plasmas was at ~3 nm for $C_4F_8/Ar/N_2$ and ~4 nm for $C_4F_8/Ar/O_2$.

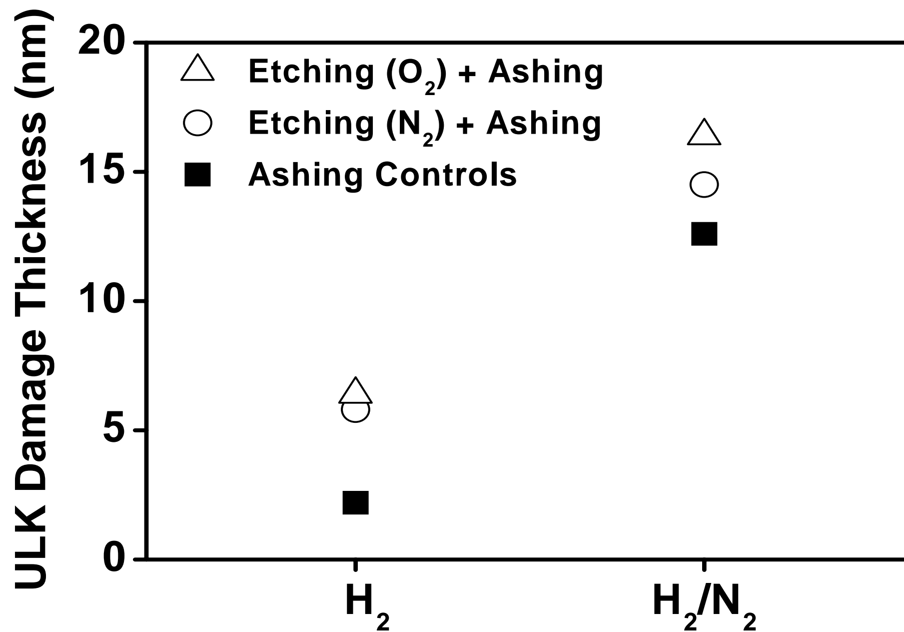

Figure 2.9: ULK damage thickness for plasma etching/remote plasma ashing process sequences and ashing only. Plasma etching using a CCP reactor was performed using $C_4F_8/Ar/O_2$ for 148 s and $C_4F_8/Ar/N_2$ for 191 s. A small gap structure was used to expose the ULK material for sidewall-like conditions. The ashing processes consisted of exposures to H_2 or H_2/N_2 (1/1) remote discharges for 60 s. Damage thickness was evaluated using the 1% HF solution selective etching method.

A. *Trench sidewall evolution for sequential plasma processes*

XPS was used to characterize the surfaces of blanket ULK films exposed to $C_4F_8/Ar/N_2$ and $C_4F_8/Ar/O_2$ etching plasmas in a small gap structure. The results of C 1*s*, F 1*s*, N 1*s*, Si 2*p*, and O 1*s* spectra are shown in Fig. 2.10. In the C 1*s* spectra, the plasma-deposited FC films with four characteristic peaks[2.33] assigned to C-CF_x (x=1, 2, 3), CF, CF_2, and CF_3 bonding in the order of binding energies can be seen. For $C_4F_8/Ar/N_2$, the incorporation of nitrogen into the FC film can be directly observed

from CNF, NCF, NCF_2, and NCF_3 peaks in the C 1*s* spectrum and in NC_xF_y peak in the N 1*s* spectrum. The integrated intensities of N-related peaks matched for the N 1*s* and C 1*s* spectra after being normalized by their sensitivity factors. Relative to C_4F_8/Ar/O_2, its CF_x peak intensities in the C 1*s* spectra and C_xF_y intensity in F 1*s* spectra were higher, indicating more FC deposition on the ULK surface with the N_2-containing gas mixture. Signals of Si 2*p* and O 1*s* spectra derived from the ULK substrates. Due to being attenuated by the FC overlayer, their intensities show an inverse relationship to the amount of FC deposition (overlayer), i.e., weaker Si 2*p* and O 1*s* intensities for C_4F_8/Ar/N_2 relative to C_4F_8/Ar/O_2. The C/Si ratio of etching-plasma-exposed ULK was calculated from intensities of C-Si/C-C moiety versus Si 2*p*. It was 0.43 for C_4F_8/Ar/N_2 and 0.32 for C_4F_8/Ar/O_2. Since the initial value from untreated ULK was 0.62, the obvious loss of intrinsic carbon confirmed the plasma damage, which was less for the plasma chemistry of C_4F_8/Ar/N_2 than for C_4F_8/Ar/O_2.

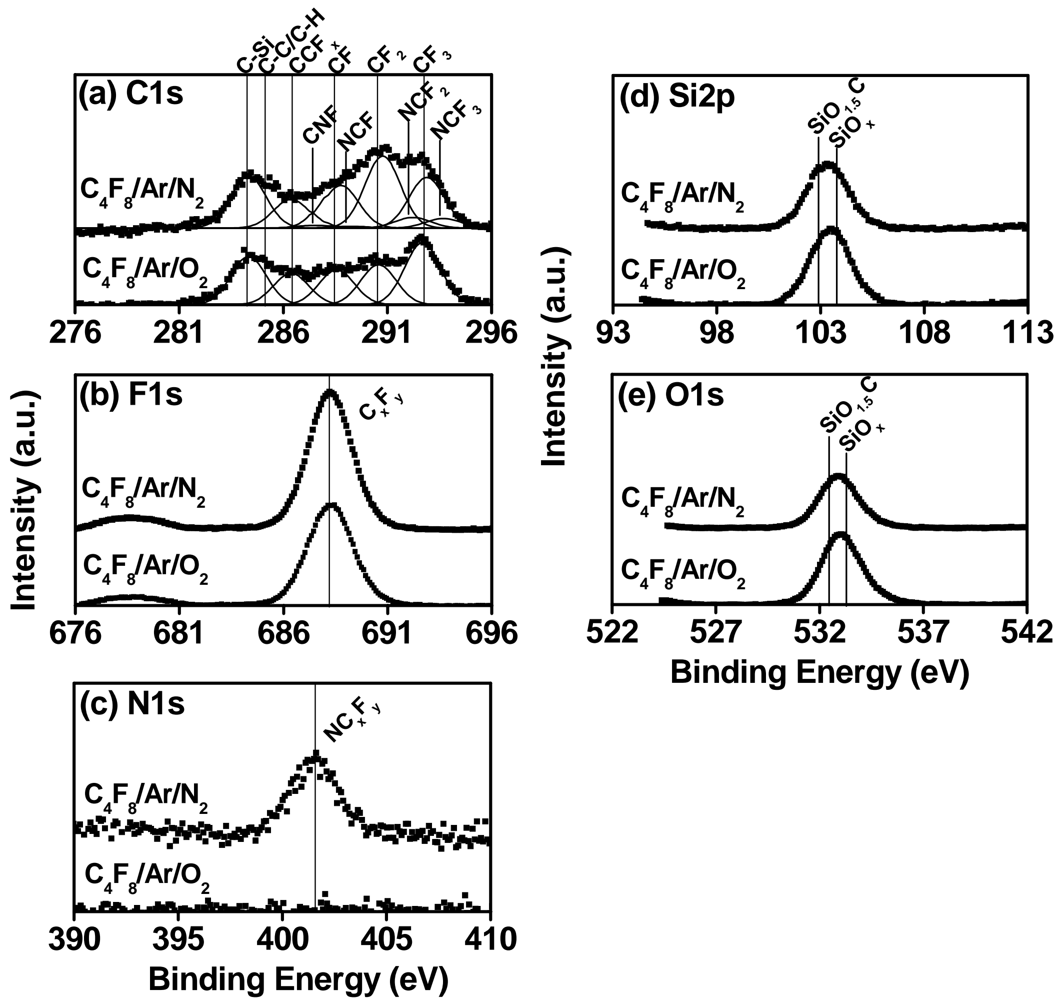

Figure 2.10: C 1*s*, F 1*s*, N 1*s*, Si 2*p*, and O 1*s* XPS spectra on ULK films exposed to CCP $C_4F_8/Ar/O_2$ etching plasma for 148 s or $C_4F_8/Ar/N_2$ etching plasma for 191 s in a small gap structure, which simulated sidewall-like exposure conditions.

Fig. 2.11 shows the XPS spectra of ULK surfaces after C_4F_8/Ar-based plasma etching/remote H_2 based ashing combined processes. For comparison, the spectra of untreated ULK and ULK with only remote ashing plasma exposure are also added. The etching-plasma-deposited FC films evident on the ULK surface (see Fig. 2.10) are nearly absent after the H_2-based remote ashing procedure. Most of the F 1*s* signal was lost post H_2 ashing. For $C_4F_8/Ar/O_2$, the ratio of remaining F 1*s* intensities to that

from post-etching ULK was 25% for H_2 [Fig. 2.11(c)] and 13 % for H_2/N_2 [Fig. 2.11(f)] while for $C_4F_8/Ar/N_2$, it was 14% for H_2 [Fig. 2.11(d)] and 8% for H_2/N_2 [Fig. 2.11(g)]. Even though $C_4F_8/Ar/N_2$ plasma left more FC films on post-etching ULK surfaces, the N_2-contained FC film was more easily removed by H_2-based remote plasma than O_2-based FC film. In general, H_2/N_2 (1/1) remote plasma is more efficient in etching-related FC residue cleaning than 100% H_2. For the sake of having clear readings, the integrated peak intensities of intrinsic carbon C-Si/C-C, Si 2*p*, and O 1*s* and binding energies of Si 2*p* and O 1*s* with different processing conditions are summarized in Fig. 2.12. Since most of the FC was removed, with minimized signal attenuation due to an overlayer, the intensities of C-Si/C-C peak from ULK show sensitively the loss of intrinsic carbon due to etching/ashing plasma exposure by comparison with the initial intensity. The carbon loss indicates H_2/N_2 remote plasma [Fig. 2.12(a) (e))] introduced higher damage into the ULK than pure H_2 [Fig. 2.12(a) (b)]. Due to etching-induced damage, the carbon loss on the ULK in the etching/ashing combined processes was worse than that on ULK only exposed to remote plasmas. Since the carbon content of the ULK has been depleted after the etching process, the loss of carbon while exposed to the remote ashing plasma appears to saturate. For the worst case of $C_4F_8/Ar/O_2$ etching and H_2/N_2 ashing combined process [Fig. 2.12(a) (f)], the ratio of carbon loss reached ~57%. The difference between carbon loss after H_2/N_2 and pure H_2 exposure [Fig. 2.12(a) (e) and (b)] is reduced with a prior C_4F_8/Ar etching plasma exposure [e.g., Fig. 2.12(a) (f) and (c) for $C_4F_8/Ar/O_2$]. This shift of binding energies as shown in Fig. 2.12(b), of Si 2*p* and O 1*s* is more precise in presenting the modification in intrinsic methyl groups.

It is consistent with the depletion of C-Si/C-C peak intensities in C 1*s* spectra as shown in Fig. 2.12(a). For ashing controls [see Figs. 2.12(b) (b) and (e)], when carbon was depleted from Si-C by ashing plasma, Si was subsequently bonded with residual oxygen. The change of chemistry increased the binding energies of Si and O in silica networks. Since for H_2/N_2 plasma, more carbon was depleted than that for H_2 plasma, a larger BE shift than that for H_2 plasma can be seen. For H_2 plasma exposure, the carbon depletion was much higher in etching/ashing combination relative to ashing control [see Fig. 2.12(a) (c) and (d) vs. (b)]; however, the amount of oxygen incorporation was not as responsive to the carbon depletion. That suggests that when the ULK was exposed to C_4F_8/Ar etching plasmas, carbon was depleted and the dangling site was replaced with fluorine. A portion of these fluorine can remain bonded through the ashing process and subsequent air exposure. The bonding of fluorine to Si also correlates the shift of Si 2*p* and O 1*s* spectra to a high BE [see Fig. 2.12(b) (c) and (d) vs. (b)] when corresponsive oxygen incorporation was not observed in these cases.

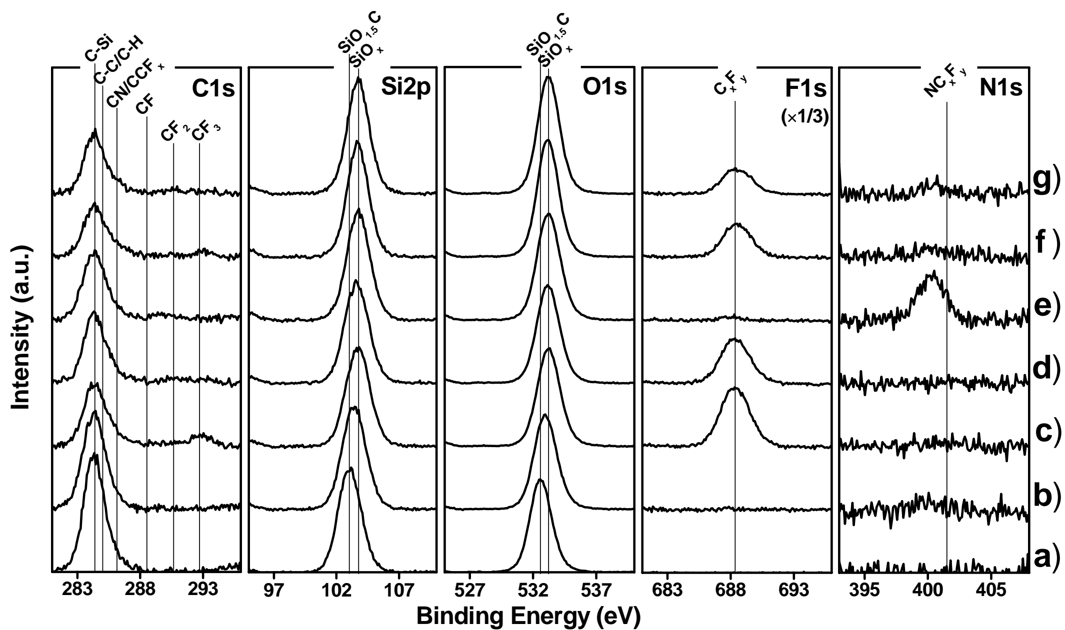

Figure 2.11: C 1*s*, Si 2*p*, O 1*s*, F 1*s*, and N 1*s* XPS spectra of ULK films exposed to CCP etching plasmas and remote ashing plasma process sequences. CCP etching plasma exposures were performed using $C_4F_8/Ar/O_2$ plasma for 148 s or $C_4F_8/Ar/N_2$ plasma for 191 s in a small gap structure, which simulated sidewall-like exposure conditions. Subsequent remote plasma exposures were performed using H_2 or H_2/N_2 (1/1) remote plasmas for 60 s. For comparison, the spectra of blanket ULK film and ULK films with remote plasma exposure (ashing controls) are also shown. (a) Untreated ULK; (b) H_2 remote ashing only; (c) $C_4F_8/Ar/O_2$ etching + H_2 remote ashing; (d) $C_4F_8/Ar/N_2$ etching + H_2 remote ashing; (e) H_2/N_2 remote ashing only; (f) $C_4F_8/Ar/O_2$ etching + H_2/N_2 remote ashing; (g) $C_4F_8/Ar/N_2$ etching + H_2/N_2 remote ashing.

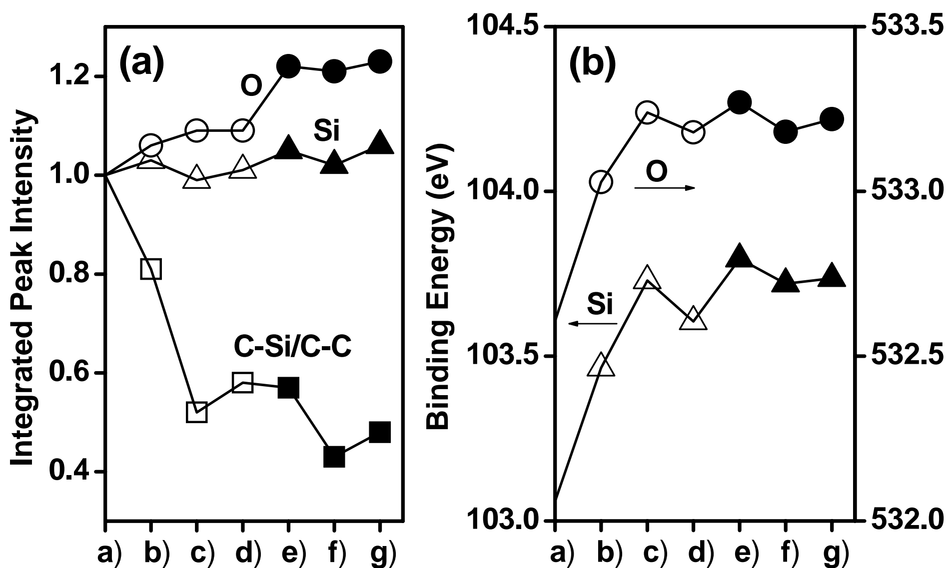

Figure 2.12: Summaries of (a) integrated intensities of C-Si/C-C in C 1*s*, Si in Si 2*p*, and O in O 1*s*, and of (b) Si 2*p* and O 1*s* binding energies from Fig. 2.11. The integrated intensities are normalized relative to the values measured for the untreated ULK.

B. Effects of etching-introduced modification on ashing damage

In order to directly evaluate the impact of etching processes on follow-on ashing damage by chemistry modification, we employed ToF-SIMS depth profiling to analyze ULK films. For these experiments, we used D_2 instead of H_2 for the ashing processes, which made it possible to distinguish “hydrogen atoms” (represented by D atoms) introduced during remote plasma processing from intrinsic H atoms in ULK films. Results for ULK films exposed to D_2 remote plasma are shown in Fig. 2.13. The existence of D in ULK films confirmed the approximately 100 nm deep permeation of D during remote plasma exposure. The slightly lower deuterium (D) amount and in-depth distribution (about 80 nm) inside ULK in combined process

relative to that in ashing control experiments also confirmed the etching/ashing interaction for ULK ashing damage. Most of the FC deposit can be effectively removed by H_2 remote plasma at elevated substrate temperatures. The residual penetrated FC appears to reduce D diffusion into the ULK films during the elevated temperature process. ULK damage, as evidenced by carbon depletion and SiO_2 densification from the surface, was, therefore, reduced for ULK films after $C_4F_8/Ar/N_2$ and $C_4F_8/Ar/O_2$ etching plasma exposure under sidewall-like conditions. Since this protection effect from sparse FC residuals was minor and observed only using SIMS depth profiling, as per Fig. 2.13, HF staining was not able to detect it (see Fig. 2.9).

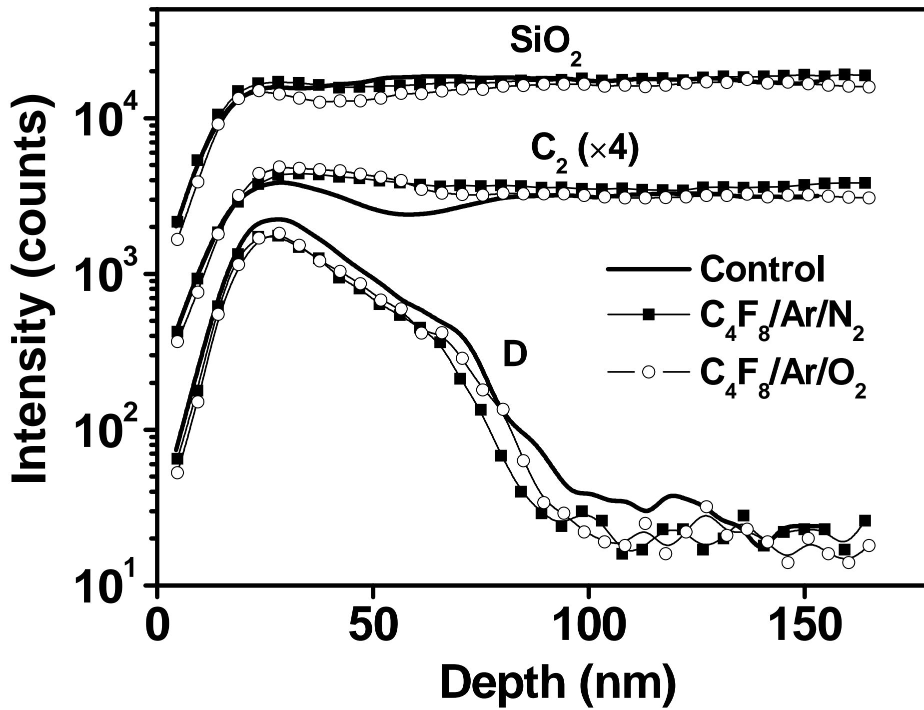

Figure 2.13: ToF-SIMS depth profiling of ULK for plasma etching/remote plasma ashing combined experiments and ashing controls. CCP etching plasma exposures were performed using $C_4F_8/Ar/O_2$ for 148 s or $C_4F_8/Ar/N_2$ for 191 s in a small gap structure, which simulated sidewall-like exposure conditions. Remote plasma exposures were performed using D_2 remote plasma with 275 °C substrate for 60 s.

C. Actual pattern transfer process for ULK materials

The ashing process performance was evaluated in this work using both blanket and patterned ULK films. Pure H_2 and H_2/N_2 (1/1) remote plasma ashing was performed on ~60 nm wide trench structures. SEM images displayed in Fig. 2.14(a) and 2.15(a) were obtained with structures plasma etched using $C_4F_8/Ar/O_2$ for 177 sec and $C_4F_8/Ar/N_2$ for 228 sec with the other parameters described in the experimental section. Etching time was not optimized and, thus, ULK was in the under-etched

trench structures. The etched structures were exposed to H_2 and H_2/N_2 remote plasmas at 275 °C substrate temperature for 60 sec for PR ashing. According to the analysis of SEMs obtained with post-ashing structures [see Fig. 2.14(b) and 2.15(b) for H_2; 2.14(c) and 2.15(c) for H_2/N_2], the effective ashing rate of H_2/N_2 remote plasma was slightly higher than that of pure H_2 remote plasma. For samples prepared using $C_4F_8/Ar/N_2$ plasma etching, the etching time was extended and the remaining post-etching PR layer was thinner. This also led to less post-ashing PR residue on the structures as compared to structures plasma etched using $C_4F_8/Ar/O_2$. HF etching of post-ashing ULK employing trench structures has been widely used for SEM characterization of ULK damage for pattern transfer and mask stripping processes.[2.6,2.8,2.9] The damage of post-ashing ULK was assessed following HF-dipping. The profile changes [see Figs. 2.14(d) and 2.15(d) for H_2; Figs. 2.14(e) and 2.15(e) for H_2/N_2] clearly indicate that H_2/N_2 remote plasmas introduced more ULK damage than occurred with pure H_2 remote plasmas. In addition, ULK trench profiles were severely damaged at the top corners with the H_2/N_2 plasma, where rounding is observed. The structure effect was caused by the combination of the characteristics of the remote plasma reaction and the selection of layer stacks. During remote plasma ashing, the PR mask is removed isotropically. Since there was no hard mask between PR and ULK in our layer stacks, the top surface of the ULK was gradually opened and exposed to the remote plasma. This created an additional damage pathway for plasma reactants to attack the ULK and thus caused greater damage at the top corners. For samples with $C_4F_8/Ar/N_2$ plasma etching, due to less PR coverage on the ULK top surface during ashing processes than when using $C_4F_8/Ar/O_2$, this structure effect

was more pronounced. As a result, more ULK damage can be seen than with $C_4F_8/Ar/O_2$ plasma etching. Although the quality of the SEM images is not very good, the ULK damage differences between using H_2 or H_2/N_2 plasmas for PR ashing for etching/ashing combined processes can be distinguished for the Fig. 2.14 and Fig. 2.15 SEM data. The ULK damage was defined as the loss of ULK between post-etching and after HF-dipping. Estimated at the height in the trench, which is ~100 nm under the top surface of the ULK stack, damage using either $C_4F_8/Ar/O_2$ or $C_4F_8/Ar/N_2$ etching was approximately 10 nm for H_2 ashing and 20 nm for H_2/N_2 ashing. The difference of modified thickness between H_2 and H$_2$/N2 ashing are quantitatively consistent with the data shown in Fig. 2.9, which were obtained using blanket wafers, and support the conclusion drawn from the studies using blanket films.

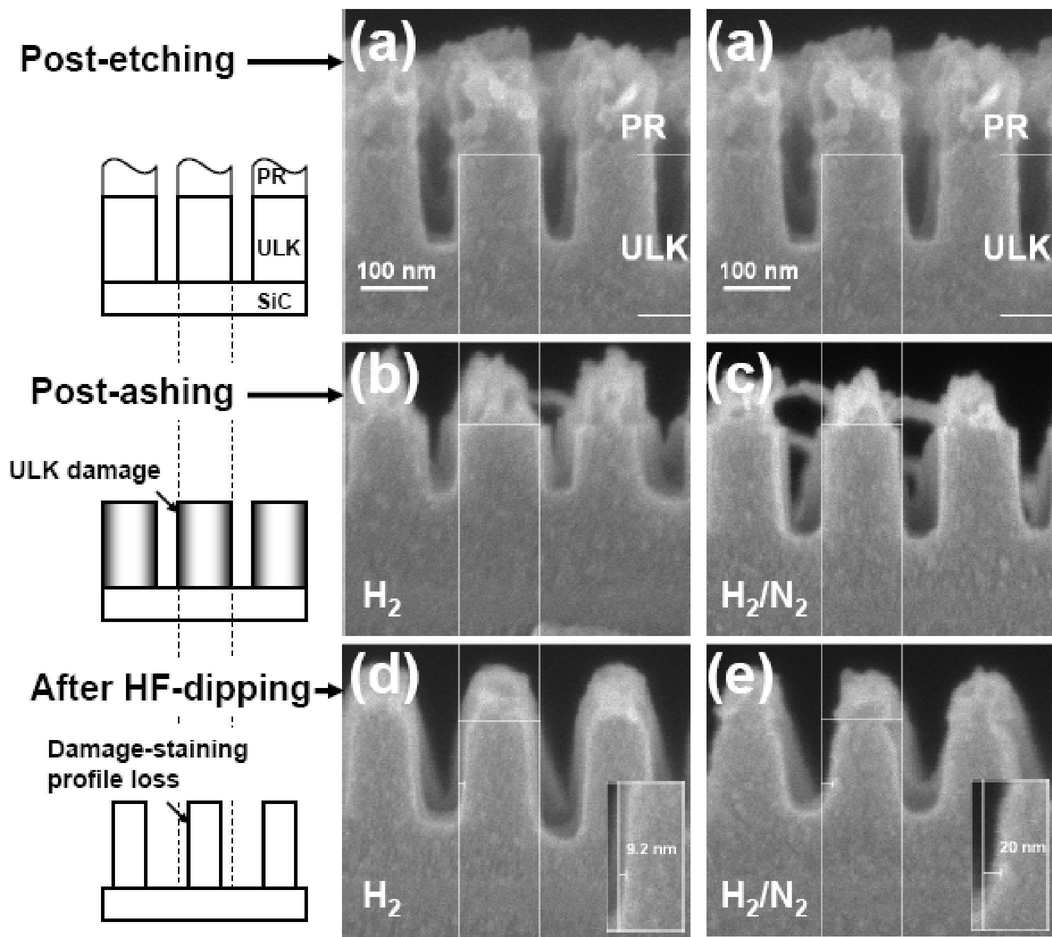

Figure 2.14: Illustration and SEM cross-sectional profiles of ULK trenches etched using (a) CCP $C_4F_8/Ar/O_2$ plasma for 177 s, (b) subsequently ashed by pure H_2, or (c) H_2/N_2 (1/1) remote plasma at 275 °C substrate for 60 s, and finally dipped into 1% HF solution/15 s for damage evaluation [(b)→(d), (c)→(e)].

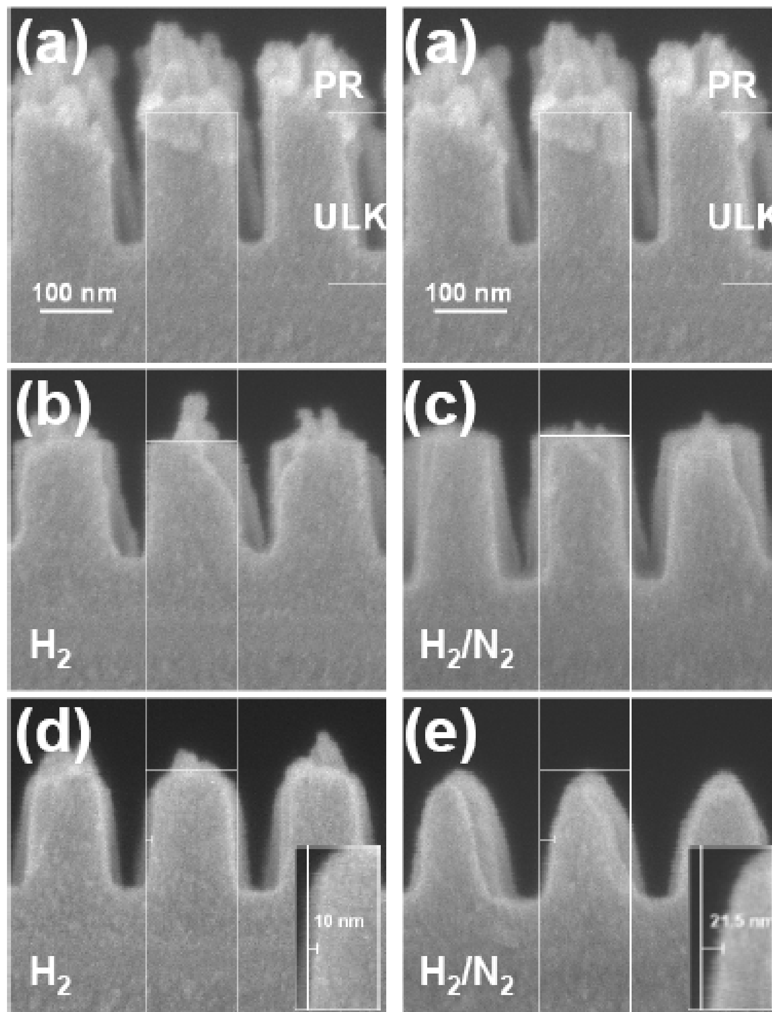

Figure 2.15: SEM cross-sectional profiles of ULK trenches etched using (a) CCP $C_4F_8/Ar/N_2$ plasma for 228 s, (b) subsequently ashed by pure H_2, or (c) H_2/N_2 (1/1) remote plasma at 275 °C substrate for 60 s, and finally dipped into 1% HF solution/15 s for damage evaluation [(b)→(d), (c)→(e)].

2.4 CONCLUSIONS

Hydrogen remote plasma processes were examined for stripping of 193 nm PR and for compatibility with nanoporous carbon-containing ULK materials. For the process conditions used in our work (H_2 remote plasma, 100 mTorr gas pressure, 50 SCCM flow rate, 1000 W inductive source power, and a substrate temperature of

275°C), the PR ashing rate can approach 900 nm/min while the ULK damage was limited to 5 nm for 20 sec remote plasma exposure. Increasing the substrate temperature from 200 to 275°C increased the PR removal rate more rapidly than the ULK damage spatial extent. This suggests the use of a substrate temperature of 250°C to 275°C, for which an ashing efficiency of ~60 is possible. The influence of N_2 or Ar gas additions to H_2 on ULK damage and ashing efficiency was also examined. Over the temperature range examined, ULK damage thickness increased with the amount of N_2 in the H_2/N_2 gas mixture. At a substrate temperature of 275°C, required to achieve a practical PR ashing rate for H_2/N_2, we observed strongly enhanced ULK damage for H_2/N_2 gas mixtures, and ashing efficiency could not be increased for H_2/N_2 relative to pure H_2.

The surface modifications at ULK trench sidewalls introduced by C_4F_8/Ar plasma etching processes and interactions with H_2 based remote plasma PR stripping processes were also investigated. For $C_4F_8/Ar/O_2$ or $C_4F_8/Ar/N_2$ plasma etching in a CCP reactor, we observed, in reference to blanket ULK materials processed under sidewall-like conditions, the introduction of ~ 3 nm FC deposits. After additional H_2 remote plasma ashing at a substrate temperature of 275°C, most of the FC deposit was removed. Deuterium depth profiling of ULK films by ToF-SIMS after CCP etching/D_2-based remote plasma ashing and comparison with specimens that were exposed only to D_2-based remote plasma ashing showed that the FC coating/ULK surface modifications introduced by the CCP etching processes reduced D permeation into the ULK, along with reduced ULK densification and carbon loss.

Patterned ULK structures were processed, employing the same ashing conditions after prior FC plasma etching in a CCP reactor. The ULK damage results measured with trench structures were consistent with processed blanket ULK film data.

ACKNOWLEDGEMENTS

Financial support of this work by the Semiconductor Research Corporation's Center for Advanced Interconnect Sciences and Technology (CAIST) under Task ID: 1292.023. is gratefully acknowledged. The authors also thank International SEMATECH and Texas Instruments for supplying the ultralow-*k*, low-*k*, and photoresist materials.

Chapter 3: Mechanistic Study of ULK-Compatible CO_2 *In Situ* Photoresist Ashing Processes. I. Process Performance and Influence on ULK Material Modification

To be submitted to J. Vac. Sci. Technol. B, 2010

M.-S. Kuo, A. R. Pal, G. S. Oehrlein, P. Lazzeri, and M. Anderle

ABSTRACT

In situ photoresist (PR) ashing processes are attractive because of the ease of process integration with plasma etching processes. We have examined the performance of carbon dioxide (CO_2) as a source gas for *in situ* PR ashing processes compatible with ultralow *k* (ULK) materials and compared it with results obtained using O_2. We performed measurements of 193 nm PR ashing rates in a dual frequency capacitively coupled plasma (CCP) reactor. The damage to porous ULK feature sidewalls was simulated by exposing blanket ULK films in a non-line-of-sight fashion in a small gap structure to the plasma-generated reactants. The pressure for the *in situ* ashing processes was varied from 10-100 mTorr, and the self-bias voltages ranged from floating potential to ~-400 V. To increase line-of-sight etching of PR by inert ion bombardment, Ar/CO_2 mixtures with up to 75% Ar were investigated. The ULK material modifications were analyzed by x-ray photoelectron spectroscopy (XPS) and time-of-flight secondary ion mass spectroscopy (ToF-SIMS). Plasma-damage of the ULK material primarily is detected as removal of carbon from the

SiCOH ULK films. To compare the performance of different ashing processes for PR stripping from ULK material, we introduced an ashing efficiency (AE) parameter which is defined as the thickness of PR removed over the thickness of ULK simultaneously damaged, and can be considered a process figure of merit. AE with CO_2 was about 3 times greater than AE with O_2 for the same process conditions. When a 75% Ar/CO_2 gas mixture was used and a -100 V substrate bias was applied during PR ashing, a PR ashing rate of 200 nm/min could be achieved for a 10 mTorr Ar/CO_2 plasma. For this process, the measured AE was 230, more than 10× greater than AE achieved with O_2 discharges using the same conditions. We found that ULK damage showed a direct dependence on the atomic oxygen densities of both CO_2 and O_2 discharges which was characterized by optical emission of discharges. The question whether in-diffusion of carbon species from CO_2 discharges into ULK material was significant was also examined. For this we substituted $^{13}CO_2$ for $^{12}CO_2$ and performed ToF-SIMS analysis of the exposed ULK films. No significant amount of ^{13}C from $^{13}CO_2$ plasmas was detected either on the surface or in the bulk of the $^{13}CO_2$ plasma-exposed ULK.

3.1 Introduction

Resistance-capacitance (RC) delay, crosstalk and power dissipation associated with the increasing capacitance of interconnect structures have become limiting factors for the performance of high-speed microelectronics and driven the introduction of low dielectric constant materials.[3.1-3.3] Of these, porous ultralow *k* (ULK) materials with an effective dielectric constant (κ_{eff}) lower than 2.6 can meet the requirements of the 45 nm node and beyond.[3.4] However, during plasma-based pattern transfer and ashing processes, pore-enhanced plasma reactant diffusion leads to severe ULK modifications (see for instance, the ITRS 2007 edition[3.5], which has emphasized the impact of damage during PR stripping on κ_{eff} of the ULK dielectric as well as on reliability and yield). To achieve coordinated non-damaging PR stripping processes for porous ULK materials, the ashing plasma/ULK interaction for essential ULK candidate materials has to be studied in prior work. Remote ashing processes using hydrogen-based plasmas as opposed to oxygen can minimize ULK damage while providing a practical ashing rate for a high temperature substrate.[3.6-3.9] An attractive alternative to this kind of process that eliminates the need for a dedicated remote plasma processing reactor is *in situ* PR ashing, also known as reactive ion etching (RIE).[3.10] This approach enables a fully integrated pattern transfer process consisting of both plasma etching and PR stripping and is performed in the same plasma reactor. Capacitvely coupled plasma (CCP) systems have been widely used for low *k* material plasma etching and enable low material damage and high etching selectivity.[3.11] The modifications of ULK materials exposed to capacitive plasmas based on O_2 and other chemistries including H_2, N_2, N_2/H_2, NH_3, and Ar have been

studied and discussed.[3.12-3.16] The use of CO_2 *in situ* ashing has been proposed by Fuller *et al*.[3.15] In the present work, we systematically compare the performance of CO_2 as a source gas with conventional O_2 for PR stripping and with regard to process-induced modifications of ULK material. The discharges were characterized using optical emission spectroscopy employing argon (Ar) actinometry and a Langmuir probe. We used a small gap structure and blanket ULK samples to simulate the non-line-of-sight plasma exposure of ULK trench/via sidewalls during *in situ* ashing processes.[3.17,3.18] The use of blanket ULK samples enables characterization of plasma-induced ULK modifications by ellipsometry, X-ray photoelectron spectroscopy (XPS) and time-of-flight secondary ion mass spectroscopy (ToF-SIMS). For CO_2 *in situ* ashing, both PR ashing rates and the ULK damage inflicted will be reported. We also will present a discussion of the damage mechanism of ULK exposed to CO_2 plasma.

3.2 Experimental setup and procedures

The ULK and PR materials used in this work were blanket films on bare silicon wafers. Methyl silsesquioxane (MSQ) dielectric film (JSR LKD 5109) with a *k* value of 2.2 was selected as a representative porous ULK material in this work. Films were spin-coated at a thickness of 420 nm on Si. The photoresist material used for PR stripping studies was 400 nm of 193 nm (ArF) PR film.

3.2.1 Capacitively coupled plasma source and small gap structure

CO_2 and comparative O_2 *in situ* ashing processes were performed in a dual frequency CCP reactor (see Fig. 1.2). For all experiments, plasmas were maintained using 40 SCCM gas flow and a 200 W source power. The gas pressure was varied from 10 to 100 mTorr. Substrate temperature was maintained at 10 °C during material processing. In the effort to acquire an optimal process performance, for selected cases, Ar was added to the gas flow (up to 75% of the total) and/or an RF substrate bias (< -400 V) was applied.

During stripping the blanket PR films were directly exposed to the plasma, and a line-of-sight interaction between the PR mask and the plasma occurred. The samples were mounted at the center of a 125 mm diameter substrate. An *in situ* laser ellipsometer was employed for real time monitoring of the PR thickness change with time, and PR ashing rates for different processing conditions were obtained.

The modifications of ULK material that are of primary interest for this work take place at the ULK sidewalls of trenches or vias during plasma etching and ashing. Because characterization of the modifications of the ULK material that take place in real trench structures is difficult, sidewall-like reactions were simulated in this work using blanket ULK films located in a small gap structure (see Fig. 2.3) using an appropriate geometry.[3.17,3.18]

3.2.2 Materials diagnostic

Selective etching of modified ULK over unmodified ULK using DHF method (0.5%/ 15s) solution provides an expedient approach to quantify ULK damage induced by plasma processing.[3.19]

The *in situ* and *ex situ* ellipsometers used for the ashing rate and ULK damage measurements had a polarizer-compensator-sample-analyzer (PCSA) configuration and employed a 632.8 nm He/Ne laser source beam at an incident angle near 73° from the surface normal. Simulations were performed using single layer models (film plus substrate) to determine thickness changes. Additional surface analysis was performed by x-ray photoelectron spectroscopy (XPS) employing a Vacuum Generators ESCA Mk II analysis chamber. The instrumental parameters are described in detail in Sec. 2.2. The ToF-SIMS measurements were carried out on a ToF-SIMS IV instrument (IONTOF: Germany). Static SIMS spectra were collected for both detection polarities [positive and negative secondary ions (SI)] using 15 keV Ga^+ as the primary probe on an analyzed area of 300 μm × 300 μm. The mass resolution was ~ 6000 at $^{16}O^-$ and ~7000 at $^{28}Si^+$. In addition, dynamic SIMS depth profiles were acquired using 1.5 keV Cs^+ as the sputtering beam with a raster area of 300 μm × 300 μm. Negative SI were collected using a 15 keV Ga^+ primary probe on an analyzed area of 0.1 mm × 0.1 mm. The mass resolution was ~ 7300 at $^{16}O^-$. Samples were sputter-coated with ~10 nm of gold. The sputtered crater depth was measured by a mechanical profilometer (KLA Tenkor P15). For both SSIMS and DSIMS sample charging was compensated by electron flooding using an electron gun.

3.2.3 Plasma diagnostic

The CCP glow discharges were characterized using optical emission spectroscopy (OES). The relative densities of important discharge species were measured using Ar actinometry.[3.20] During the measurement, a small amount of Ar (2.5%) was added to the feed gas of the plasma. The plasma induced emissions of excited states of Ar* and species of interest were compared. For this comparison we assumed that emission from excited states was proportional to the density of species in the ground state. In addition, a Langmuir probe was utilized to measure the ion current density (ICD). The distance between the top (source power) and bottom (bias power/ substrate) electrodes was 4 cm. The cylindrical probe tip of the Langmuir probe was located at the center of the gap, and a bias of -100 V was applied to collect ions in the ion saturation region of the current-voltage characteristic of the probe.

3.3 Results and discussion

3.3.1 Ashing efficiency

For PR stripping near room temperature, ion bombardment of the PR is required to enhance the ashing rate.[3.10] The directed energetic ions selectively bombard PR surfaces on the top of features, while little ion bombardment of ULK sidewalls occurs. ULK sidewalls are exposed to incident neutral fluxes. Upon adsorption at surfaces, the neutrals can permeate throughout the dielectric by a pore-enhanced diffusion mechanism and extensively modify Si-C bonds in the ULK material. During *in situ* PR ashing it is fairly straightforward to optimize the PR ashing rate, and preventing ULK damage during PR stripping is a primary concern.

We define the ashing efficiency (AE) as the thickness of PR removed during a given processing time over the thickness of ULK simultaneously damaged. A process with high AE provides a reduced ULK damage depth for a given PR thickness stripped.

A. Gas pressure

The performance of CCP for *in situ* ashing processes using CO_2 was examined and compared with results obtained with conventional O_2. A pressure range between 10 to 100 mTorr was selected. The choice of gas pressure is expected to play a dominant role in the control of the ion/neutral ratio of the discharge and via variations of the ion/neutral ratio strongly influence process AE. The PR ashing rate and ULK damage depth determined in the fashion described above are reported as a function of gas pressure for CO_2 and O_2 plasmas without substrate bias in Figs. 3.1(a) and 3.1(b), respectively. For both gas sources, the PR ashing rate decreased and ULK damage increased with gas pressure, which resulted in a great reduction of AE with increasing pressure [see Fig. 3.1(c)], indicating that *in situ* ashing should be performed at low gas pressure. Changing the gas source from O_2 to CO_2 reduced both ashing rate and ULK damage thickness. Because the reduction of ULK damage was larger than the reduction of the PR ashing rate (by a factor of ~5 as compared to a factor of ~2), AE using CO_2 for *in situ* ashing was improved about ~3 times relative to AE using O_2. A best AE value of ~18 was obtained for CCP *in situ* CO_2-based ashing (no substrate bias) at the lowest pressure used (10 mTorr).

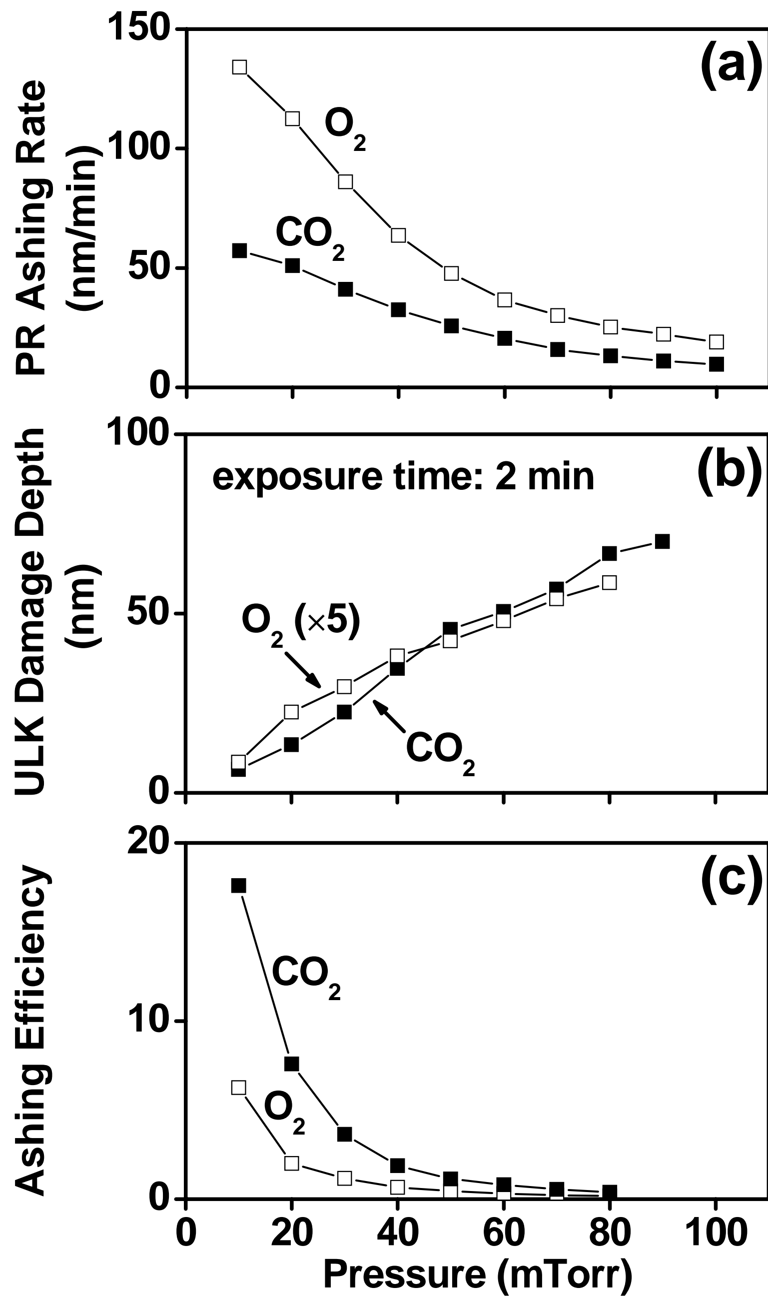

Figure 3.1: Photoresist ashing rate (a), ULK damage (b), and ashing efficiency (c) of CO_2 and O_2 discharges as a function of gas pressure. The other experimental parameters were: 40 SCCM gas flow, 200 W source power, no bias power to substrate. ULK damage was evaluated for 2 min of exposure. AE is defined as the thickness of PR layer removed divided by the thickness of ULK material damaged during the same process step (2 min of plasma exposure in this work).

Because of the absence of ion bombardment of ULK surfaces, ULK damage can be attributed to interaction with neutral plasma components. The density of neutral species changes with gas pressure may correlate with observed ULK damage trends. We used Ar actinometry to examine density changes of neutral species of interest with gas pressure. For this 2.5% of Ar was added to the feed gas, and OES data was acquired for the discharges used for *in situ* ashing. Trends in atomic oxygen density (arbitrary units) were determined by argon actinometry using the relation

$$[\mathrm{O}] = k \frac{I_{\mathrm{O}}}{I_{\mathrm{Ar}}} p_{\mathrm{Ar}} \tag{2.1}$$

where [O] denotes atomic oxygen density, and k is a proportionality constant. I_O and I_{Ar} are the measured optical emission intensities of atomic oxygen at 844.6 nm and argon at 750.4 nm ($2p_1 \rightarrow 1s_2$)[3.21], respectively. p_{Ar} is the argon partial pressure. The optical emission at 844.6 nm results from the decay of excited atomic oxygen ($3p^3P \rightarrow 3s^3S^0$).[3.21] It is typically assumed that emission from excited states is proportional to the density of ground state species.[3.20] Although excited atomic oxygen can also be produced by dissociative excitation of O_2, the optical emission at 844.6 is dominated by and has been attributed to direct excitation of atomic oxygen in the ground state [O(^3P)].[3.22,3.23]

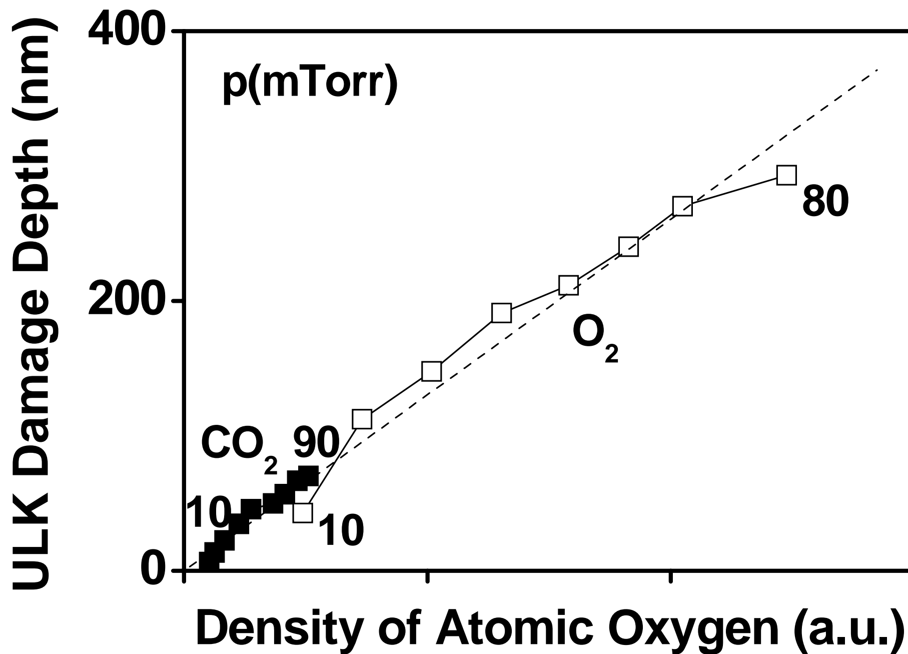

Figure 3.2: Damage thickness of ULK exposed to CO_2 and O_2 discharges as a function of atomic oxygen density measured for discharges operated at different gas pressures. The other experimental parameters were: 40 SCCM gas flow, 200 W source power, no bias applied to substrate and 2 min exposure time. Changes in atomic oxygen density were determined from the intensity variation of the 844.6 nm O atom related emission line and Ar actinometry.

In Fig. 3.2, the amount of ULK damage is shown as a function of measured atomic oxygen density [obtained by Ar actinometry, $I(\mathrm{O}_{844.6\ \mathrm{nm}})/I(\mathrm{Ar}_{750.4\ \mathrm{nm}})$] for both CO_2 and O_2 plasmas as a function of gas pressure. For both CO_2 and O_2 plasmas, the change in the ULK damage seems to correlate directly to the increase of the atomic oxygen density with increasing gas pressure. The correlation of ULK damage depth and atomic oxygen density for both O_2 and CO_2 *in situ* ashing processes indicates that atomic oxygen dominates the introduction of ULK damage for these conditions. Electron impact dissociation is the most likely primary generation mechanism of

atomic oxygen for both CO_2 and O_2 low pressure discharges. For CO_2 discharges, the production of atomic oxygen in the ground state O(^3P) is primarily caused by electron impact dissociation of CO_2 molecules through electronic excitation:[3.24,3.25]

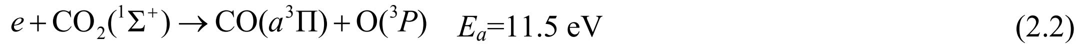

$$e + \mathrm{CO_2}(^1\Sigma^+) \rightarrow \mathrm{CO}(a^3\Pi) + \mathrm{O}(^3P) \quad E_a\text{=11.5 eV} \tag{2.2}$$

For O_2 discharges, the production of O(^3P) can take place through electron impact excitation of O_2 molecules:[3.26]

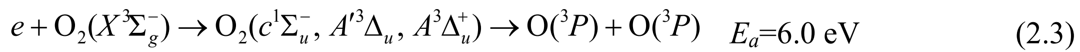

$$e + \mathrm{O_2}(X^3\Sigma_g^-) \rightarrow \mathrm{O_2}(c^1\Sigma_u^-, A'^3\Delta_u, A^3\Delta_u^+) \rightarrow \mathrm{O}(^3P) + \mathrm{O}(^3P) \quad E_a\text{=6.0 eV} \tag{2.3}$$

If the decay of O atoms is not influenced by the presence of CO or CO_2 molecules in the CO_2 discharge,[3.27] the low atomic oxygen density of CO_2 discharges can be explained by the higher threshold energy of the primary atomic oxygen production channel. The atomic oxygen density produced with the CO_2 plasma was less than that generated with the O_2 plasma using the same operating conditions; consequently, damage was reduced for CO_2 compared to O_2. The increase of the atomic oxygen density with increasing gas pressure in the CCP reactor for the CO_2 and O_2 plasmas is explained by the higher density of source molecules.[3.23] Therefore, to reduce ULK damage, the ashing plasma should be operated at low gas pressure characterized by a lower atomic oxygen density. AE depends on both the amount of ULK damage introduced and the PR ashing rate that can be achieved for the same conditions. To confirm the expected relationship between the ashing rate and ion current at the wafer surface, the ion current density (ICD) of plasmas used for *in situ* ashing was measured employing a Langmuir probe. The ICD decreased with increasing gas pressure. In Fig. 3.3, we show ashing rate as a function of ICD measured for the

corresponding CO_2 or O_2 process conditions. A strong correlation between the ashing rate and plasma ICD is indicated by this data and in agreement with ion-enhanced etching.[3.28] Because the plasma ions were collected using a Lamguir probe with a -100 V bias, the current density might be different than the current density that reached the PR surface on the floating substrate due to various factors, e.g., sheath collisions. Fig. 3.3 broadly reveals the relationship between the ashing rate on plasma ICD for both O_2 and CO_2 discharges. The comparison between O_2 and CO_2 plasma ions in regard to their etching yields will be discussed later.

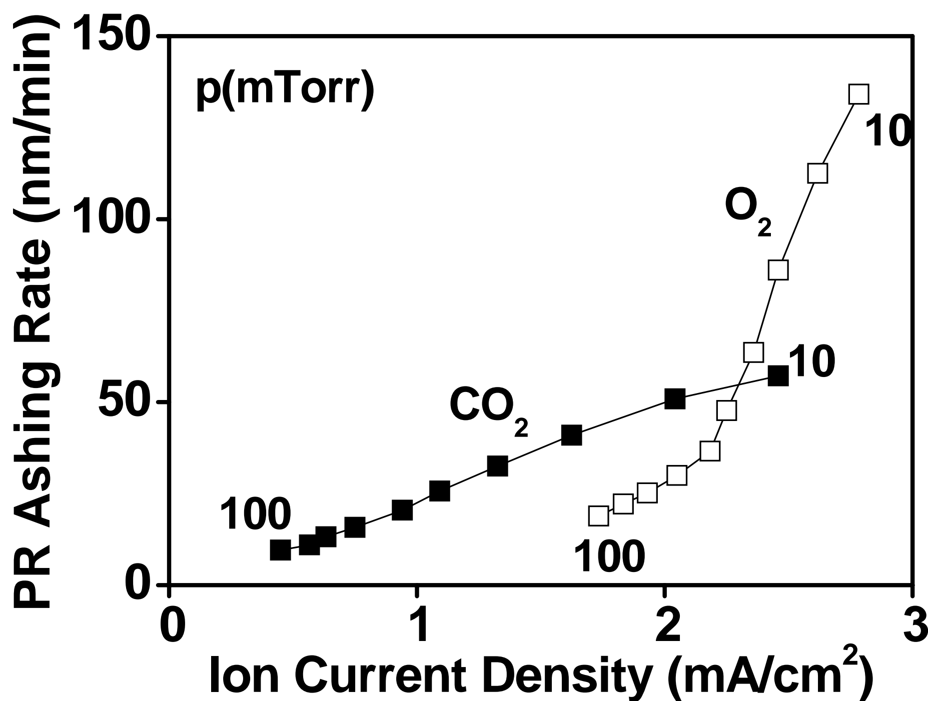

Figure 3.3: PR ashing rates measured for CO_2 and O_2 discharges operated between 10 and 100 mTorr. PR ashing rates are plotted versus the ion current density measured for the same conditions. The other experimental parameters were: 40 SCCM gas flow, 200 W source power, no bias applied to substrate. The ICD was measured using a Langmuir probe 2 cm above the substrate with a -100 V bias.

B. Argon addition

The major drawback of CO_2 plasma for *in situ* PR ashing is the fairly low ashing rate. To improve the ashing rate, Ar was added to CO_2 discharges, which can enhance ICD at the wafer surface.[3.29] The effect of Ar addition in the CO_2/Ar mixture on the ashing rate, ULK damage and AE are shown in Figs. 3.4 (a), 3.4(b) and 3.4(c), respectively. Figure 3.4(a) shows the variation of the ICD with gas composition. An increase of ICD with Ar addition was confirmed for both low (10 mTorr) and higher (100 mTorr) pressure plasmas. The ashing rate increased for 100 mTorr but decreased for 10 mTorr discharges with Ar addition. The impact of Ar addition to CO_2 on the ashing rate was found to depend on gas pressure. For ULK, the damage depth decreased with Ar addition to CO_2 [see Fig. 3.4(b)]. For a constant total pressure, the amount of CO_2 molecules in the reactor decreased with Ar addition. Fewer oxygen atoms should be produced for Ar-rich CO_2/Ar discharges, which explain the decrease of ULK damage with Ar content. This is consistent with the earlier observation that the introduction of ULK damage during CO_2 *in situ* ashing scaled with atomic oxygen content of the discharge. Although ULK damage was different for different gas pressures (ULK damage was greater at 100 mTorr than for 10 mTorr), the reduction of ULK damage seen as a result of Ar addition to CO_2 was similar for high and low pressure operation. For discharges operated at 100 mTorr, AE was improved by Ar addition to CO_2 due to the combination of increased ashing rate and decreased ULK damage. At 10 mTorr, Ar addition decreased both ULK damage and ashing rate. Because the reduction of ULK damage was higher than the reduction of PR ashing

rate, AE increased to 47 at 10 mTorr when pure CO_2 plasma was replaced with a 75% Ar/CO_2 plasma.

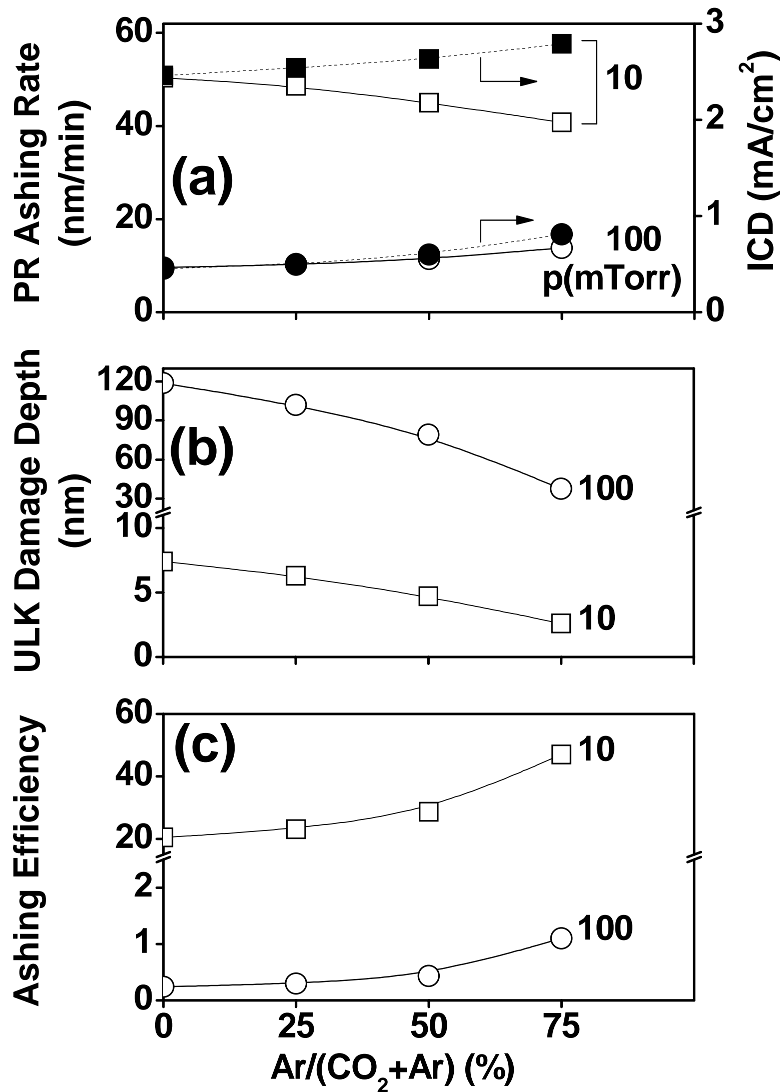

Figure 3.4: Photoresist ashing rate (a), ULK damage (b), and ashing efficiency (c) of 10 and 100 mTorr CO_2/Ar discharges as a function of %Ar added to CO_2. Ashing efficiency is defined as the thickness of PR removed after 3 min of process time over the thickness of ULK damaged during the same period. Plasmas were maintained at a 40 SCCM gas flow and 200 W source power, and no bias was added to the substrate. ULK damage and AE were evaluated for 3 min of exposure.

C. Substrate bias

Substrate bias combined with Ar addition was used to increase the energy flux to the substrate and resulted in a higher polymer etching rate.[3.30,3.31] Fig. 3.5 shows PR ashing rates versus the applied self-bias voltage for the 10 mTorr O_2 and Ar/CO_2 discharges with different gas mixing ratios. A rapid increase of ashing rate with self-bias voltage is seen for pure CO_2 plasma. As with an unbiased substrate, Ar addition to 10 mTorr CO_2 discharges decreased the ashing rate. The damage to ULK in the small gap structure was independent of the applied bias (not shown here). Although the CO_2-based ashing rate with a -100 V self-bias voltage decreased from ~280 nm/min for 0% Ar to ~200 nm/min for 75% Ar, the concomitant reduction of ULK damage was more significant (see Fig. 3.4). AE with substrate bias can therefore be improved by Ar addition. For a 75% Ar/CO_2 plasma with a -100 V self-bias, an AE of ~230 was obtained at a PR ashing rate of ~200 nm/min.

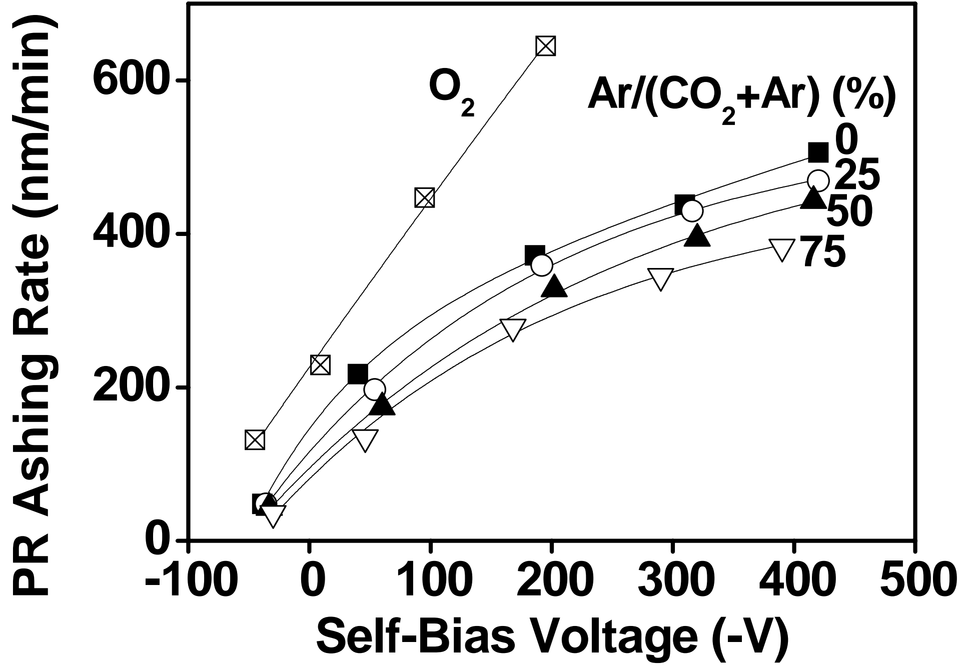

Figure 3.5: Photoresist ashing rates measured for pure O_2 and Ar/CO_2 discharges as a function of self-bias voltage. Different CO_2/Ar mixtures were used. Plasmas were maintained at 10 mTorr of gas pressure, 40 SCCM of total gas flow and 200 W of source power.

The ICDs collected from the Langmuir probe were assumed to correspond to the ICDs at the substrate with a -100 V self-bias (and consistent with RF bias power used). Based on the measured ICDs, the ion etching yield (*EY*) at a -100 V self-bias was calculated from

$$EY = \frac{ER \cdot \rho \cdot N_A \cdot q}{M_w \cdot j} \times N_c, \tag{3.4}$$

where *ER* denotes the PR ashing rate, ρ the polymer density, N_A Avogadro's number, *e* the electron charge, *q* the charge state of the ion, M_w the molecular weight of a

monomer, j the ion current density, and N_c the total number of carbons in a monomer. For 193 nm PR, ρ was 1 g/cm^3, and M_w was 208. N_c was 12. Dominant ions for O_2 and CO_2 discharges with Ar addition were assumed to be single-charged O_2^+, CO_2^+, and Ar^+ ions; thus, q is $+e$. The *EY* of 10 mTorr discharges with a -100 V self-bias was calculated for O_2 and CO_2 with different ratios of Ar addition. Fig. 3.6 indicates that the *EY* of CO_2 discharge decreased with Ar addition to CO_2. When ion-assisted chemical reaction with atomic oxygen is used to explain PR stripping, the etching yield of ions with a fixed energy depends on the gas phase density of oxygen, which controls the surface adsorption rate of oxygen.[3.28] The decrease of *EY* for the CO_2 discharge with Ar addition can be explained by a decreased amount of reactive atomic oxygen available for etching, which was insufficient for low pressure (10 mTorr) operation and further correlates to the decrease in the ashing rate for either unbiased or biased conditions. In addition, the higher *EY* for O_2 relative to CO_2 discharge might be attributed to a greater chemical sputtering rate and abundant atomic oxygen for the ion-assisted reaction between PR and O_2^+ ions.[3.28,3.32] Because the ICDs at 10 mTorr were similar for O_2 and CO_2 discharges, the ionic *EY* was primarily responsible for the low ashing rate of CO_2 relative to O_2.

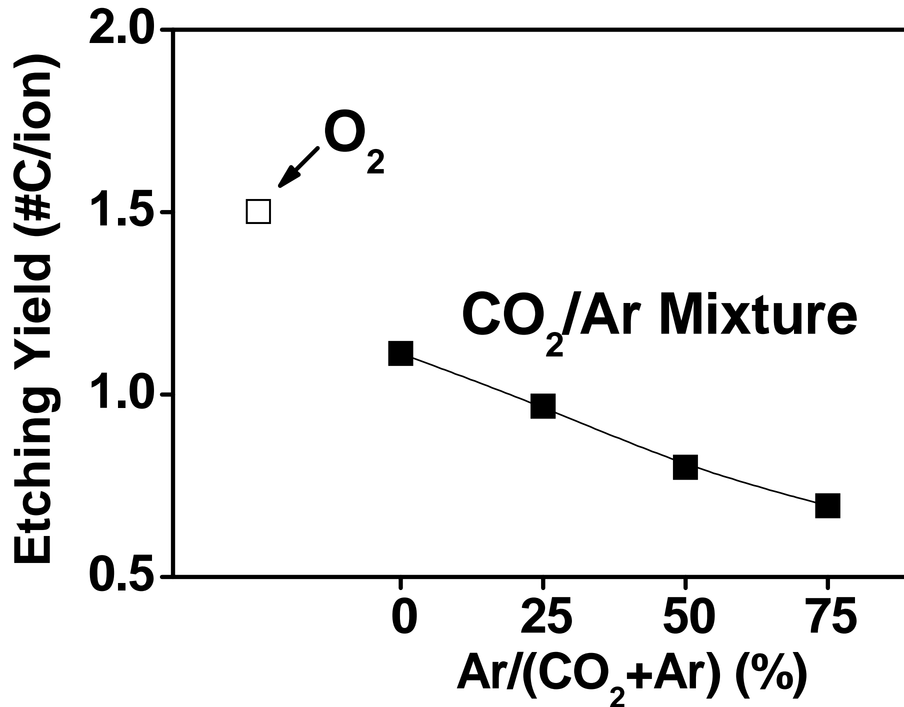

F
igure 3.6: Ion etching yields for O_2 and Ar/CO2 discharges with -100 V self-bias.

3.3.2 ULK material modification

For the results described up to this point, the ULK damage depth was determined by DHF selective etching. In the following, XPS and ToF-SIMS were employed to study surface and bulk chemical changes of the plasma-exposed ULK. The modification mechanisms of ULK exposed to oxygen-containing plasma under sidewall-like conditions will be discussed.

A. XPS

The probing depth of XPS is limited to ~10 nm, and most experimental conditions used here induce ULK modifications at greater depths. Nevertheless, the surface chemical bonding information can provide insight into the mechanism of ULK plasma damage. C 1*s*, Si 2*p* and O 1*s* spectra for untreated ULK and ULK exposed to 10 and 100 mTorr O_2 and CO_2 plasmas were acquired. To observe chemical changes of the ULK surfaces processed under sidewall-like plasma exposures, the spectra obtained with plasma-exposed ULK were subtracted from the spectra obtained for untreated ULK. These data are displayed in Fig. 3.7. We found that ULK surfaces after 20 s of exposure to O_2 plasma showed a shift of C 1*s* peaks from Si-C and C-C/C-H to carboxylic (CO) groups with BE from 286 to 289 eV[3.33] . The total C 1*s* intensity was not changed. This indicates that oxygen initiates the modification of ULK by bonding with carbon atoms in the ULK to form CO moieties. The incorporation of oxygen in the ULK can also be directly observed by the appearance of C=O and O-C=O[3.33] in the O 1*s* spectrum. The Si 2*p* spectrum was not changed, indicative of little change in the carbon bonding with Si. When the processing time was extended to 200 s, carbon depletion can be seen by the reduced total intensity of the C 1*s* spectrum. The increase of the O 1*s* intensity and the shift of both the Si 2*p* and O 1*s* peaks from $(\text{-Si(CH}_3)_2\text{O-})_n$[3.34] and $\text{Si(CH}_3)\text{O}_{1.5}$ for the pristine ULK material to SiO_x indicate Si oxidation and carbon removal. The spectra after 20 s of CO_2 plasma exposure were very similar to those measured after exposure to O_2 plasma using identical conditions. After 200 s of exposure to CO_2 plasma, the Si 2*p* and O 1*s* spectra changed in a fashion qualitatively similar to that described above for

the O_2 case, although the degree of change was smaller for CO_2 than for O_2. One marked difference for CO_2 plasma exposure was the fact that the C 1*s* intensity did not correspondingly decrease but remained roughly the same or slightly increased.

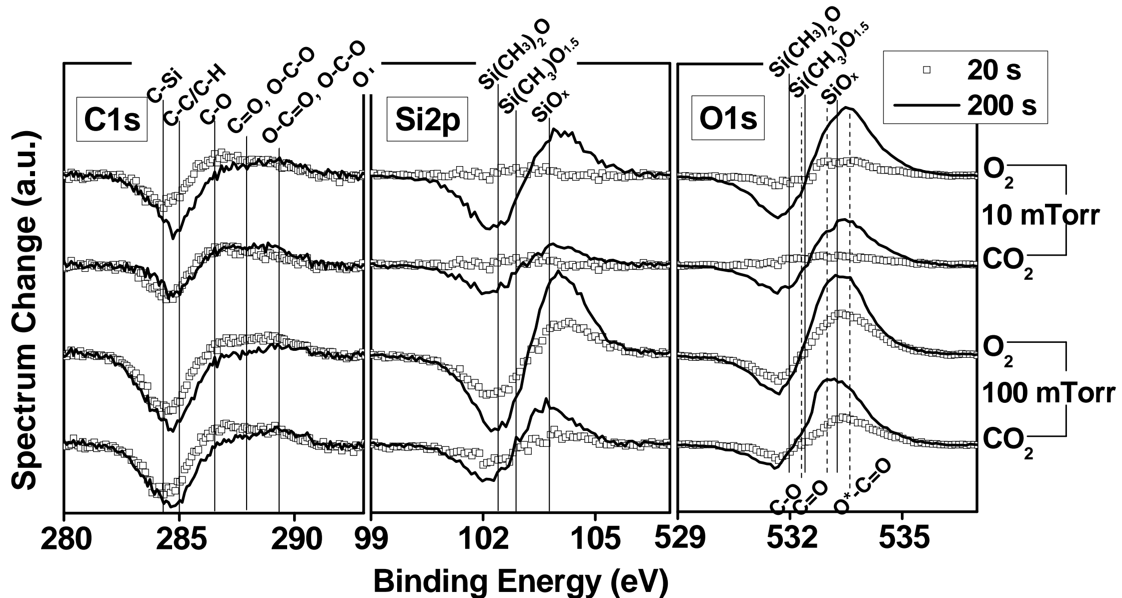

Figure 3.7: C 1*s*, Si 2*p* and O 1*s* photoemission difference spectra obtained with ULK after 20 s or 200 s of plasma exposure at two different pressures (10 and 100 mTorr for O_2 and CO_2 discharges used) and ULK reference spectra (obtained with untreated control). The other experimental parameters were: 40 SCCM gas flow, 200 W source power, no bias applied to substrate. Spectra were obtained at a photoemission angle of 90° with respect to the surface.

The effect of gas pressure is also shown in Fig. 3.7. As the gas pressure increased from 10 to 100 mTorr, the amount of oxygen incorporated into ULK increased. The magnitude of carbon loss and SiO_x conversion both increased. Overall, we conclude from the XPS studies of ULK surface damage induced by non-light-of-sight exposure to O_2 and CO_2 discharges that the magnitude of the measured Si 2*p* spectral shifts reflected the amount of ULK damage, and that the measured surface

damage levels were consistent with the correlation of ULK surface damage to the atomic oxygen gas phase density reported above.

B. ToF-SIMS

To directly evaluate whether carbon was incorporated into the ULK from CO_2 plasmas, we utilized $^{13}CO_2$ for processing and performed experiments identical to those described in conjunction with the XPS studies reported before. Employing the static SIMS technique, we collected spectra for ULK surfaces exposed to $^{13}CO_2$ discharges and resolved ^{13}C incorporation by its different atomic mass relative to the carbon present in the ULK starting material. The intensity changes of the static SIMS data for ULK after plasma treatments are displayed in Fig. 3.8. Carbon depletion and oxide conversion are indicated by the decreasing ^{12}C signal and increasing SiO_2 and SiO_3 intensities, respectively. The results show modest ULK modifications due to the CO_2 plasma treatments, except for the 100 mTorr/200 s exposure. Overall, the effects seen in the SIMS measurements reproduce the ULK damage trends as a function of plasma operating conditions found in the XPS studies. In particular, the plots of relative mass spectral intensity changes show negligible effects for 10 mTorr/ 20 s processing, intermediate changes for 10 mTorr/ 200 s and 100 mTorr/ 20 s processing and finally the strongest variations for the 100 mTorr/ 200 s process. The carbon isotope ^{13}C was observed in the measurements, but the intensity was close to the natural abundance of the heavier isotope (^{12}C: ^{13}C = 98.9: 1.1). No significant ^{13}C incorporation into the ULK material from $^{13}CO_2$ discharges was seen in the SIMS

data. This shows that any carbon incorporation from CO_2 discharges observed in the XPS studies was limited to the very surface of the ULK.

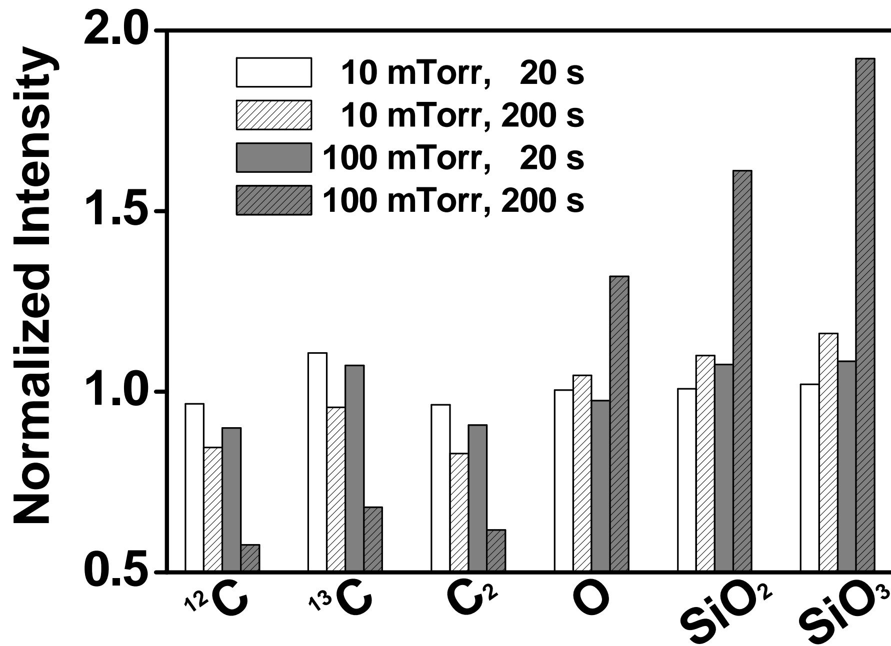

Figure 3.8: Normalized intensity of species observed in SSIMS spectra of ULK exposed to $^{13}CO_2$ plasmas maintained at a 40 SCCM gas flow rate and 200 W source power without applying a bias to the substrate. Intensities were normalized using initial intensities.

Depth profiling of bulk ULK materials was also performed using dynamic SIMS. The results are shown in Fig. 3.9. Carbon depletion can only be seen near the surface except for the 100 mTorr/ 200 s process. The low level of ULK modification seen for the films as a function of depth indicates that ULK damage introduced by CO_2 discharges was limited to the surface region except for high pressure and long time exposures, where obvious damage existed throughout the ULK film. The dynamic SIMS data show an identical process parameter dependence for carbon loss

and Si oxidation as found in the XPS and static SIMS measurements, whereas no carbon from the discharge was incorporated in the bulk of the ULK for any conditions. In addition, no film shrinkage could be seen.

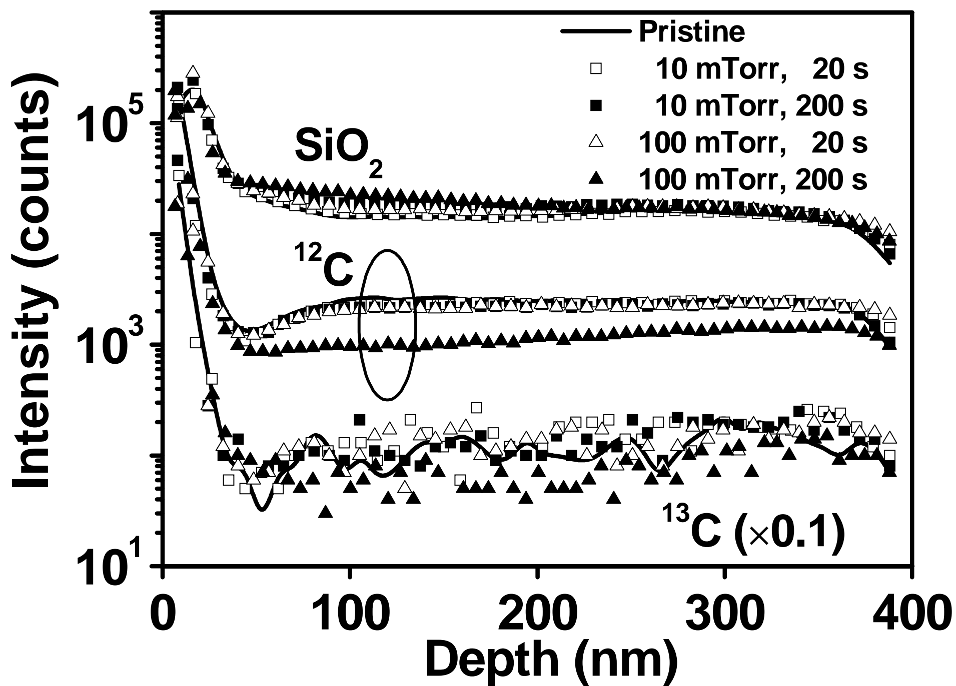

Figure 3.9: DSIMS depth profiling results obtained with untreated ULK and ULK after exposure to $^{13}CO_2$ plasma. The discharges were maintained using a 40 SCCM gas flow rate and 200 W source power without applying a bias to the substrate.

The analysis of stoichiometry changes of the ULK films can be correlated with atomic oxygen density trends measured for the CO_2 and O_2 plasmas used here. The ULK sidewall-like reaction with CO_2 or O_2 discharges can be summarized as

$$\equiv \text{Si-CH}_3 \xrightarrow{+\,\text{O}} \equiv \text{Si-CH}_x\text{O}_y \quad (3.5)$$

$$\equiv \text{Si-CH}_x\text{O}_y \xrightarrow{+\,\text{O}} \equiv \text{Si-OH} + \text{CO}_2 \uparrow \quad (3.6)$$

$$\equiv \text{Si-CH}_3 \xrightarrow{+\,\text{O}} \equiv \text{Si-OH} + \text{CO}_2 \uparrow \qquad (3.7)$$

The oxygen can subtract the hydrogen in methyl groups with simultaneous addition of O to form carboxylic groups on Si [Eq. (3.5)]. These groups are subsequently cleaved and converted into volatile CO_2 [Eq. (3.6)]. In addition, oxygen can directly eliminate CH_3 group through reaction with Si [Eq. (3.7)].[3.35] Chaudhari *et al*. presented simulation results that indicated the low energy barrier of ~0.1 eV for $O(^3P)$ to eliminate CH_3 (bonded with Si) and to subtract hydrogen (in CH_3 groups) from specific attack angles.[3.36] These results are consistent with our experimental findings using XPS and SIMS ULK measurements in conjunction with gas phase analysis. For ULK films exposed to different O_2 and CO_2 discharges at the sidewall-like position, the magnitude of chemical modification including carbon depletion, oxygen addition, and oxide conversion were correlated to atomic oxygen densities in the gas phase. The carbon incorporation into ULK during the CO_2 process, if present, was limited to the very surface.

3.4 Conclusions

We demonstrated CO_2-based *in situ* PR ashing processes with satisfactory PR ashing rates and ULK trench sidewall damage. The CO_2-based *in situ* PR ashing processes performed in a CCP reactor enabled high ashing efficiency (PR ashing rate over ULK damage) when an RF bias was applied. Key mechanistic factors of CO_2 based *in situ* PR ashing processes and ULK damage mechanisms in CCP reactor were also elucidated. For either O_2 or CO_2 *in situ* ashing, ULK exposed to the plasma

under sidewall-like conditions, and the rate of ULK damage introduction increased with atomic oxygen density of the discharge. For gas pressures ranging from 10 to 100 mTorr, use of CO_2 instead of O_2 was shown to greatly reduce ULK damage. This was explained by a lower density of atomic oxygen in the CO_2 discharges as compared to O_2 plasma. Insignificant carbon incorporation from CO_2 discharges into ULK was observed. These statements are based on XPS analysis of atomic oxygen-related surface modifications of ULK exposed to CO_2 discharges and ToF-SIMS studies in both static and dynamic modes of ULK exposed to $^{13}CO_2$ plasma. The PR ashing rate showed a parameter dependence that indicates a synergistic interaction of atomic oxygen and energetic ions.

ACKNOWLEDGEMENTS

We acknowledge financial support of this work by the Semiconductor Research Corporation’s Center for Advanced Interconnect Sciences and Technology (CAIST) under Task ID: 1292.023. We thank International SEMATECH and Lam Research for supplying the photoresist and ULK materials.

Chapter 4: Mechanistic Study of ULK-Compatible CO_2 *In Situ* Photoresist Ashing Processes. II. Interaction with Preceding Fluorocarbon Plasma ULK Etching Processes

To be submitted to J. Vac. Sci. Technol., 2010

M.-S. Kuo, A. R. Pal, G. S. Oehrlein, and X. Hua

ABSTRACT

Process interactions between fluorocarbon (FC) plasma etching ultralow *k* (ULK) dielectrics followed by CO_2 *in situ* photoresist (PR) ashing on ULK damage have been studied in a dual frequency capacitively coupled plasma reactor. Introduction of ULK trench/via sidewall damage was simulated employing blanket ULK films by exposing them in a non-line-of-sight fashion in a small gap structure to the plasma environment. ULK damage was quantified using the dilute hydrofluoric acid (0.5%/15 s) selective etching method. CO_2 *in situ* ashing processes showed a chamber memory effect due to prior FC plasma etching. For unbiased ashing conditions, the chamber memory effect influenced PR ashing rates for CO_2 discharges. No ashing rate enhancement was seen at 10 mTorr pressure whereas an ~8 times greater PR ashing rate was measured at 100 mTorr. Damage of pristine ULK films for 10 mTorr CO_2 plasma exposure was increased ~5 times by the chamber memory effect. For ULK plasma etch/PR ashing process sequences, ULK material surfaces were modified by FC plasma etching prior to the CO_2 plasma exposure. X-ray photoelectron spectroscopy studies showed that the modifications consisted primarily

of 1-2 nm FC coverage of the ULK. This FC deposit remained on the ULK surfaces during *in situ* CO_2 processing and provided protection of the underlying ULK material.

PR-patterned ULK structures were also processed employing the same processing conditions. The results obtained from characterization of the resulting trench structures support the findings obtained with blanket films. CO_2 *in situ* PR ashing processes performed at low pressure (10 mTorr) and enhanced by RF biasing provided a good combination of high PR stripping rate and low ULK damage introduction.

4.1 Introduction

The problem of ultralow *k* (ULK) material degradation caused by photoresist (PR) stripping processes has been emphasized in *the International Technology Roadmap for Semiconductors* (ITRS).[4.1] We have studied the performance of CO_2 *in situ* photoresist ashing processes in a dual frequency capacitively coupled plasma (CCP) reactor, and found them to be compatible with ULK materials (for a description see the Chapter 3).[4.2] In that work, the exposure of ULK feature sidewalls to plasma was simulated by exposing surfaces of blanket ULK films to plasma using a small gap structure.[4.3] Ashing efficiency (AE) was defined as the thickness of PR removed divided by the thickness of the ULK material simultaneously damaged. We observed that ULK damage increased with atomic oxygen density, and that a high AE can be obtained using low pressure, where reduced atomic oxygen density lowered ULK damage and application of an RF bias was used to simultaneously enhance PR ashing.

Fluorocarbon (FC)-based discharges have been widely used to etch ULK materials in a CCP etcher.[4.4] Since the etching plasma passively deposits FC films onto chamber walls, the chamber memory effect is a concern for the subsequent *in situ* PR ashing process conducted in the same reactor.[4.5] In addition, the FC plasma etching (FC-PE) -process introduces a modified layer on the PR surfaces facing the plasma (direct exposure) whereas FC deposition on ULK trench feature sidewalls exposed in a non-line-of-sight geometry can take place.[4.6-4.8] The PE-related by-products can influence the material/plasma interactions as well as the resulting material modifications during the subsequent ashing process.[4.8,4.9] In the present work

our goal was to achieve a coordinated non-damaging pattern transfer process for porous ULK materials. To this end, we studied process interactions between FC plasma etching and CO_2 *in situ* ashing for the CCP reactor on both PR ashing rate and ULK modifications. Employing a small gap structure setup, ULK sidewall-like modifications were simulated using blanket ULK films in FC plasma etching/CO_2 *in situ* ashing process sequences. The process interactions were evaluated and compared with experimental results obtained from CO_2 *in situ* ashing only processes. The mechanisms of the process interactions were determined and promising conditions for *in situ* ashing compatible with ULK materials will be demonstrated. Realistic pattern transfer processes with PR patterned ULK materials using trench features will be described. The results are consistent with our data obtained with processed blanket ULK films.

4.2 Experimental Setup and Procedures

The objective of this work was to study process interactions of plasma etching and *in situ* ashing as well as the consequences of these on a representative porous ULK material. As illustrated in Fig. 4.1, in a realistic pattern transfer process, the FC-based etching plasma produces a PE-modified layer on top of the PR mask and FC-coating of the ULK trench and hole feature sidewalls. In addition, the FC plasma etching process produces a chamber memory effect by FC film deposition on the chamber walls. Because of the chamber memory effect, fluorine is introduced into the CO_2 ashing chemistry. The process conditions for *in situ* ashing following FC etching are therefore different from CO_2 plasma ashing performed in a clean chamber, which

was evaluated in Chapter 3.[4.2] In the following, we will compare results for PR and ULK materials exposed to a FC plasma etching environment after *in situ* PR ashing in a FC-coated chamber (combined process sequence) with results obtained with pristine samples processed in a clean chamber (control experiments). These results will be compared with characterization data of patterned ULK structures after plasma etching and *in situ* ashing employing the same process conditions.

Nanoporous silica (JSR LKD 5109), a spin-coated methyl silsesquioxane (MSQ)-based dielectric with k = 2.2, was used as the representative ULK material. The photoresist material used was 193 nm (ArF) PR. The impact of a prior FC-PE process on PR ashing rate, ULK modifications, and AE during subsequent CO_2 *in situ* ashing was evaluated in this study using a dual frequency (40.68 MHz/4.0 MHz) CCP reactor (see Fig. 1.2). The ULK plasma etching process utilized (C_4F_8/90%Ar)/10%N_2 (referred to as C_4F_8/Ar/N_2). Plasma etching was performed at 30 mTorr gas pressure, a total gas flow of 44 SCCM and 200 W source power. Samples were mounted on a 125 mm electrode cooled to 10 °C and biased using 100 W RF power, which produced a self-bias voltage of about -300 V. Subsequently, *in situ* ashing processes were conducted in the same CCP reactor. For this, we produced CO_2 plasma at either 10 mTorr or 100 mTorr gas pressure employing 40 SCCM gas flow and 200 W source power. The electrode temperature was 10 °C. For selected experiments, RF bias power was applied. For PR ashing, blanket PR films were directly exposed to the CO_2 plasma, and ashing rates were determined using real-time *in situ* ellipsometry. ULK sidewall modifications introduced by the plasma etching/ashing process sequences were studied using blanket ULK films exposed in a

small gap structure to $C_4F_8/Ar/N_2$ plasma etching followed by CO_2 *in situ* ashing.[4.3] ULK damage was quantified using the dilute hydrofluoric acid (DHF) selective etching method. Surface modifications of the ULK material induced by plasma etching/ashing sequences were also analyzed by x-ray photoelectron spectroscopy (XPS). Experimental details of the XPS and ellisometric analysis were described in Sec. 2.2.

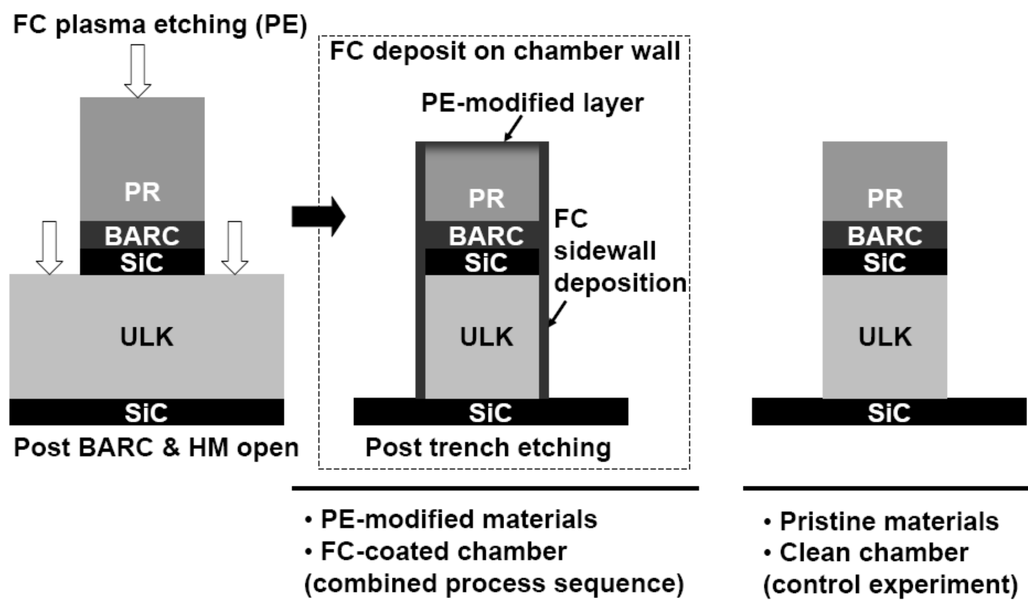

Figure 4.1: Illustration of issues related to the fluorocarbon ULK trench etching/*in situ* PR ashing process interaction.

4.3 Results and Discussion

4.3.1 PR ashing

PR removal during the ashing step of a combined process sequence was monitored using real-time ellipsometry. The temporal evolution of removed PR thickness is shown in Fig. 4.2 and is compared with data obtained for pristine PR

ashed in a clean chamber. A $C_4F_8/Ar/N_2$ plasma etching step of 100 s duration preceded the *in situ* ashing step for the PE-modified/FC coated chamber experiments (process parameters described in section II). As is well known, the PR surface is strongly modified by FC-PE exposure.[4.10-4.12] Fig. 4.2 indicate that the removal of the PE-modified PR layer was relatively difficult and led to reduced PR thickness loss during the initial period of the ashing process. From the PR thickness where the ashing rate changed, the thickness of the PE-modified layer can be determined and was about 10 nm for this work. After removal of 10 nm of material, the PR ashing rate changed from 12 to 48 nm/min for the 10 mTorr discharge and from 8 to 75 nm/min for the 100 mTorr discharge. The ashing rate of the unmodified PR was similar for the combined process sequence and the control experiments at 10 mTorr, but was dramatically enhanced for the combined process sequence when ashing was performed at 100 mTorr pressure. This indicates that chamber history due to the FC-PE process has a major effect on subsequent PR ashing if PR stripping is performed at a higher pressure, since FC films deposited during plasma etching at the inner chamber walls will be released into the gas phase during the *in situ* PR ashing process.

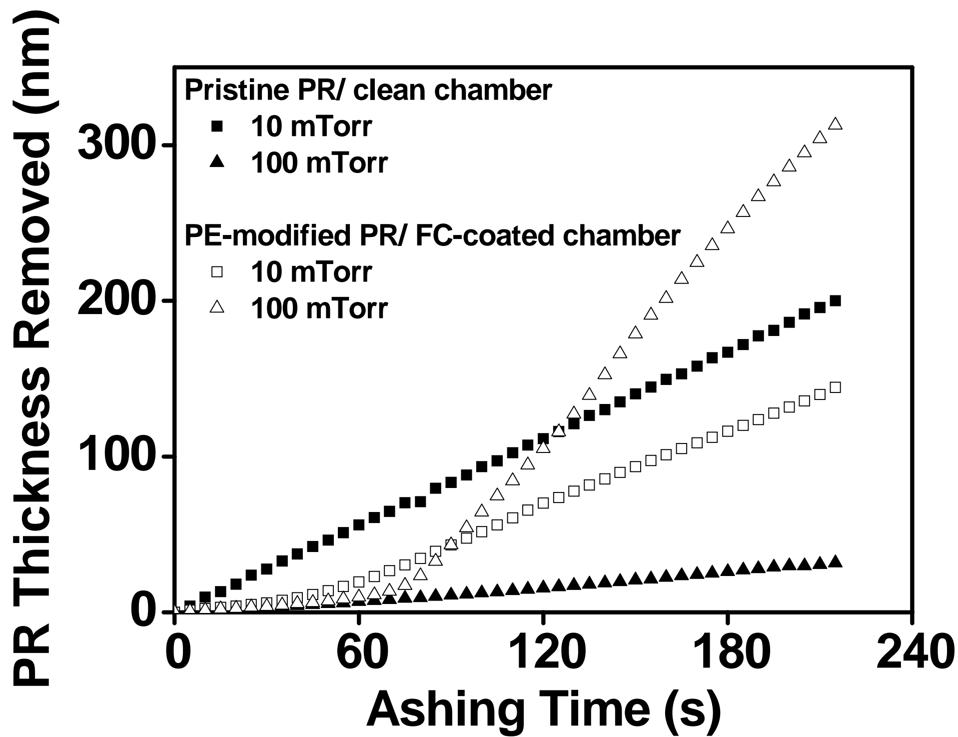

Figure 4.2: PR thickness removed in the CO_2 *in situ* ashing process. No bias power was applied to the substrate. For combined sequence process, a $C_4F_8/Ar/N_2$ PE process of 100 s duration preceded the *in situ* ashing.

To simulate the effect of FC residues on CO_2 processing, we studied PR ashing rates as a function of CF_4 added to CO_2. This is shown in Fig. 4.3. To avoid possible process interactions, the chamber was cleaned using O_2 plasma for ~20 min prior to each run, which minimized FC contamination due to prior experiments. For both the 10 and 100 mTorr experiments, the PR ashing rate peaked at 10% CF_4/CO_2. For pure CF_4 plasma, the measured PR ashing rate was very small (less than 5 nm/min). Figure 4.3 shows that for 10 % CF_4/CO_2, the PR ashing rate measured at 100 mTorr was greatly increased relative to pure CO_2, and was above the PR ashing rate measured at 10 mTorr for the same gas mixture. The results of Fig. 4.3 are

qualitatively consistent with the observations reported in Fig. 4.2 on the chamber memory effect and its impact on the PR ashing rate at different pressures. These results are consistent with prior work; for instance, addition of fluorocarbon gases to O_2 plasma has been employed in conventional PR stripping processes as an approach to enhance PR ashing rates, and explained by a mechanism where the presence of fluorine on the PR surface reduces the activation energy of the PR/oxygen reaction.[4.13] Fluorine can abstract hydrogen atoms from the PR surface and produce reactive sites that are susceptible to the attack of oxygen.[4.14] In the control experiment without fluorine, the PR ashing rate was limited by the flux of ions to the PR surface.[4.2] In our reactor, 100 mTorr discharges are characterized by a lower ion density than 10 mTorr discharges. A lower PR ashing rate is thus achieved at 100 mTorr than at 10 mTorr in a clean chamber. However, for FC plasma etching/ashing combinations, the high pressure CO_2 discharge also contained fluorine in the gas phase due to the volatilization of plasma etching-related FC, and, as a result, the PR ashing reaction was enhanced.

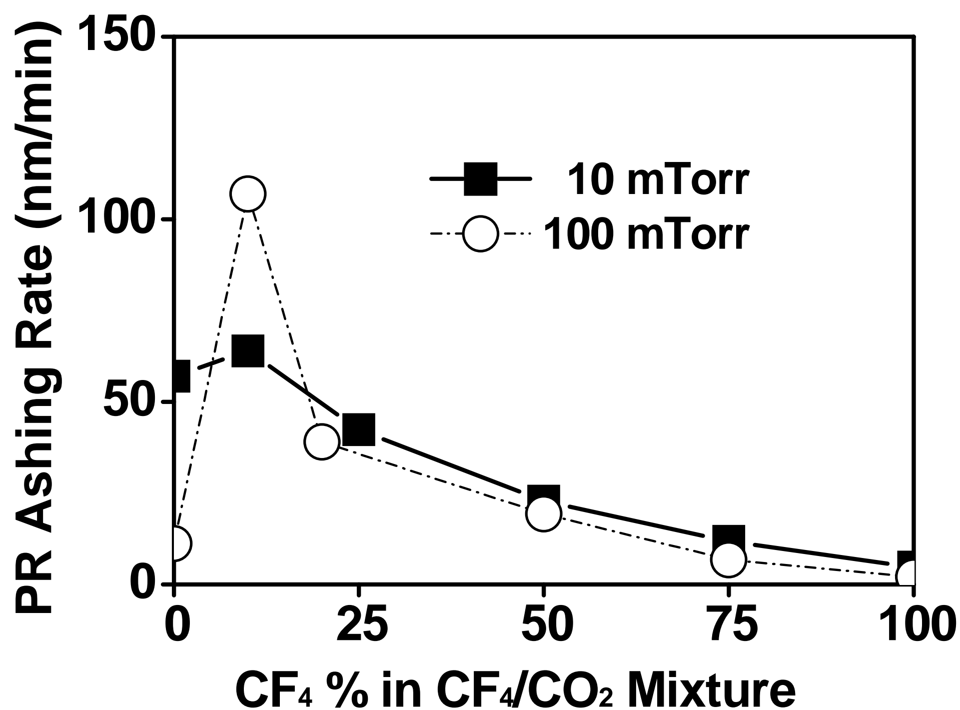

Figure 4.3: PR ashing rate as a function of CF_4 ratio in a CF_4/CO_2 mixture. Plasmas were maintained at 40 SCCM total gas flow rate and 200 W source power. No bias power was applied to the substrate. Ashing rates using 10 and 100 mTorr gas pressure were examined and compared.

To overcome the difficulty of ashing through the PE-modified PR surface layer, application of a substrate bias is useful. This is shown in Fig. 4.4 for PR ashing in a 10 mTorr CO_2 discharge. Ashing of the modified PR surface layer can be enhanced with the application of a RF bias. For an ashing process using a 10 mTorr CO_2 discharge, an essentially time-independent PR ashing rate of 90 or 180 nm/min was achieved by applying -10 V or -90 V self-bias voltage, respectively.

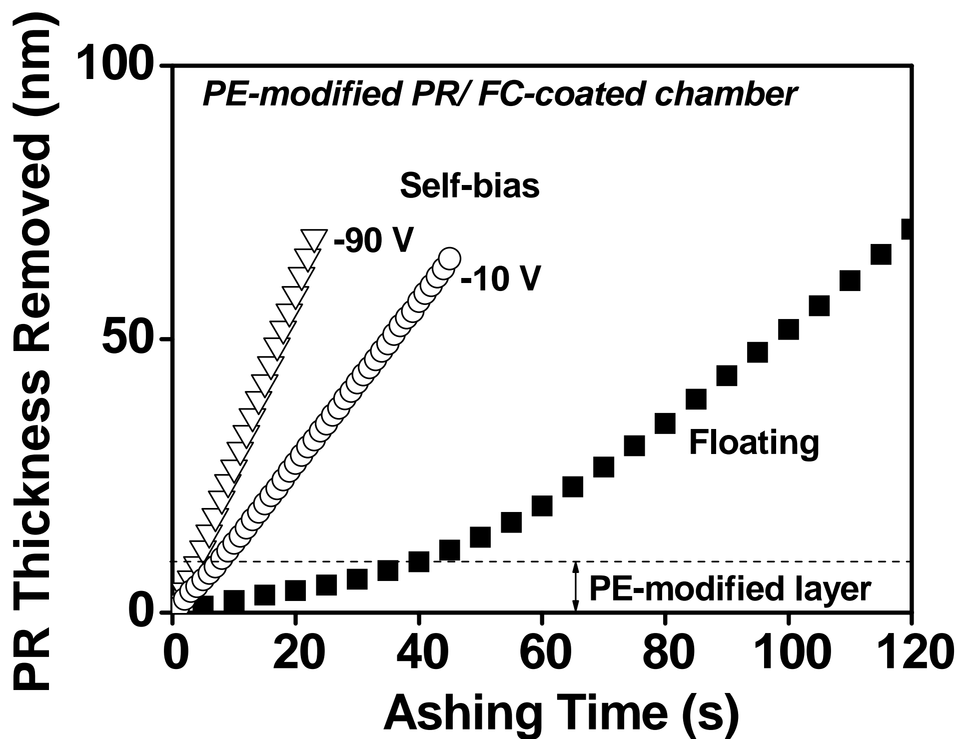

Figure 4.4: PR thickness removed in the ashing step of the combined process sequence. The ashing process was conducted using 10 mTorr CO_2 discharge. Bias power was selectively applied to the substrate. A $C_4F_8/Ar/N_2$ PE process of 100 s duration preceded the *in situ* ashing.

4.3.2 ULK damage

The modification of the chamber condition due to a prior FC plasma etching step also increased ULK damage during ashing. The thickness of ULK damage introduced during the CO_2 ashing step of a combined process sequence is depicted as a function of time in Fig. 4.5. Additionally, damage of a pristine ULK film during CO_2 ashing exposure in a clean chamber (control experiment) and a chamber after $C_4F_8/Ar/N_2$ plasma etching is shown. The plasma exposure of the blanket ULK films was performed in a small gap structure to simulate sidewall-like reactions. A rapid

growth of damaged ULK thickness is seen when pristine ULK was exposed to CO_2 in a FC-coated chamber. The ULK damage level was ~4.5 times higher than that seen for ULK processed in a clean chamber after 180 s exposure. For the latter case, the ULK damage depth was ~8 nm as revealed by the DHF etching method.

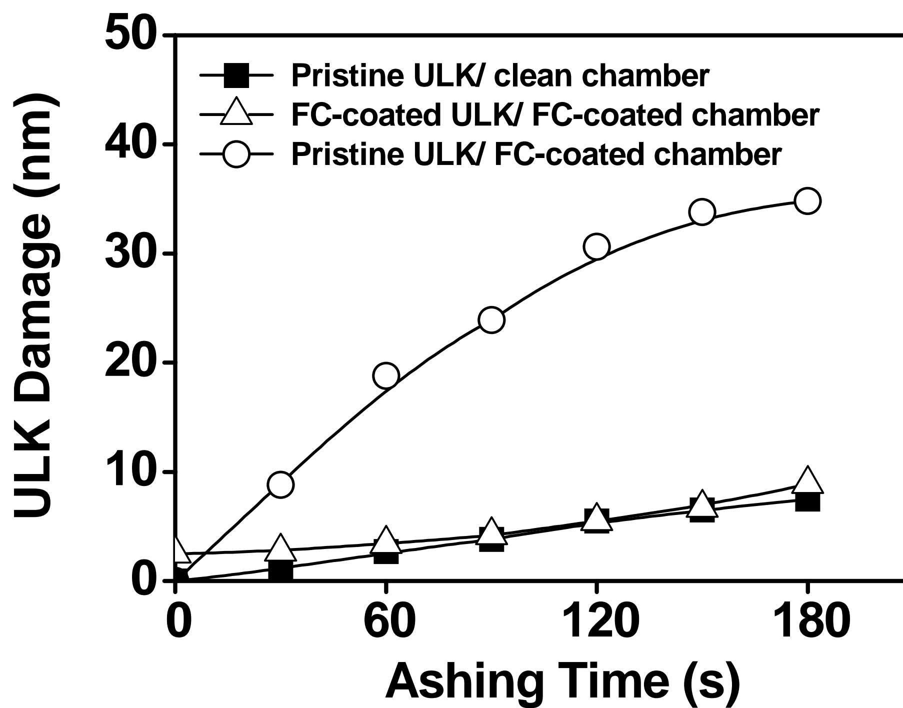

Figure 4.5: ULK damage in CO_2 *in situ* ashing process. No bias power was applied to the substrate. In some cases, to study etching/ashing process interaction, a $C_4F_8/Ar/N_2$ PE process of 160 s duration preceded the *in situ* ashing for the seasoning chamber and/or introducing PE-related ULK modification. A small gap structure was employed to simulate sidewall-like reaction on the blanket ULK films.

During a realistic FC-PE process, FC material is also deposited on the surfaces of the nanostructure, including the sidewall of features formed in the ULK

material. This effect was reproduced with the gap structure by exposing the ULK material to the FC etching discharge in that location. For ULK material processed in this fashion, some minor ULK damage was caused by the FC-plasma and can already be seen before ashing plasma exposure (see Fig. 4.5). However, Fig. 4.5 shows that the FC coverage of the ULK material reduces ULK damage introduction during a subsequent CO_2 ashing step in a FC-coated chamber by about 80% as compared to the damage level observed for pristine ULK processed in the same FC-coated chamber.

To study how the ULK material was damaged by a fluorine-containing CO_2 discharge, surfaces of a pristine ULK material after CO_2 exposure in either a clean or a FC-coated chamber were analyzed by XPS. The C 1*s*, Si 2*p*, O 1*s*, and F 1*s* spectra are shown in Fig. 4.6. The spectra obtained with untreated ULK are displayed as a reference. Previously, we described the modification mechanism of pristine ULK films during exposure to CO_2 plasma in a clean chamber.[4.2] Here, we focus on ULK damage introduction in a FC-coated chamber. The C 1*s* spectrum shows depletion of the C-Si/C-C moieties for the ULK material processed in a FC-coated chamber relative to an untreated ULK material [see Fig. 4.6(c) vs. 4.6(a)], whereas a much smaller loss of the C-Si/C-C peak intensity is observed for ULK material processed in the same way in a clean chamber [see Fig. 4.6(b)]. Only a small intensity of residual FC is seen on the ULK surface [see the low intensity in the binding energy region assigned to C-CF_x (x=1,2,3), CF, CF_2, and CF_3 bonding].[4.15] Fluorine was present at the surface of the ULK material (see the F 1*s* spectrum). When the F 1*s* sensitivity factor was employed to analyze the spectra of Fig. 4.6(c), the total fluorine content

corresponding to the F 1*s* spectrum was found to be higher than required to account for CF_x bonding in the C 1*s* spectrum. A portion of fluorine appears to be present as Si-F and Si-F_2 bonding.[4.16] In addition, because carbon was significantly depleted from Si, both the Si 2*p* and O 1*s* peaks shifted to higher binding energies.

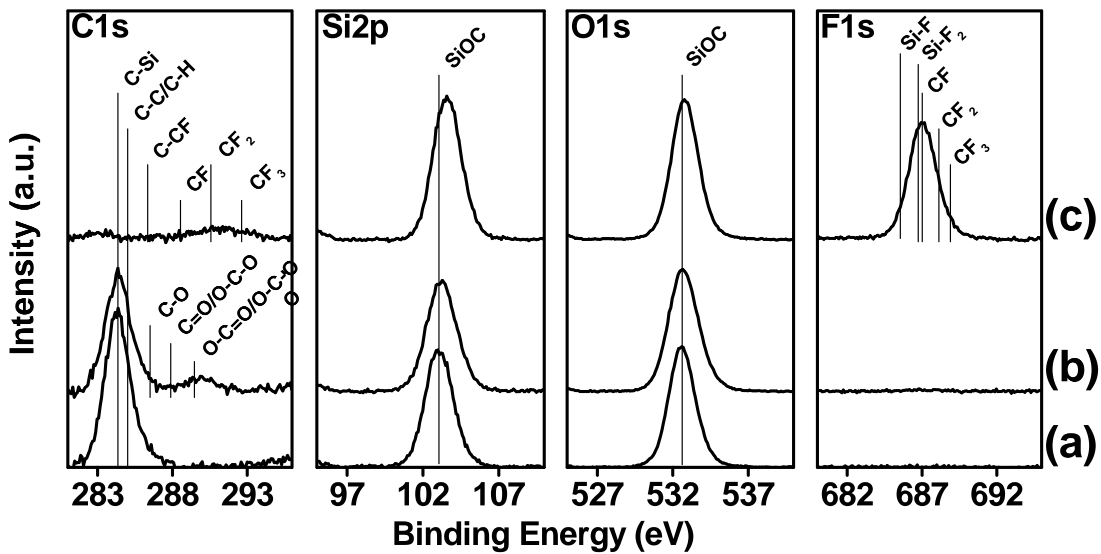

Figure 4.6: XPS C 1*s*, Si 2*p*, O 1*s*, and F 1*s* spectra of untreated ULK (a) and pristine ULK exposed to CO_2 discharges in a clean (b) and a FC-coated chamber (c) for 180 s. No bias power was applied to the substrate. A C_4F_8/Ar/N_2 PE process of 160 s duration was conducted to introduce a FC-coated chamber. A small gap structure was employed to simulate a sidewall-like reaction on the blanket ULK films. A nonmonochromatized Mg *Kα* x-ray source (1253.6 eV) was used for XPS.

The post-etching and post-ashing ULK surface in the combined process sequence was monitored by XPS. The C 1*s*, F 1*s*, N 1*s*, Si 2*p*, and O 1*s* spectra are shown in Fig. 4.7. The detailed analysis for the ULK post C_4F_8/Ar/N_2 etching plasma exposure at a sidewall-like position has been discussed in Sec. 2.3. For this discharge chemistry, a N-containing FC film was deposited on the ULK surface [Fig. 4.7(a)].

After subsequent CO_2 plasma exposure, FC intensities measured with the post-etching surface were slightly reduced. The deconvolution of the C 1*s* spectra indicates that the loss of FC intensities was primarily attributed to the removal of the FC-based film with CF_2, NCF_2, CF_3, and NCF_3 bonding. The removal was simultaneously observed in the F 1*s* spectra [Fig. 4.7(b)], where the intensity loss corresponded to the loss of FC bonding.[4.17] The reduction (of ~25%) of NCF_2 and NCF_3 was similar to that for CF_2 and CF_3. This suggests the small influence of nitrogen content on FC removal during the CO_2 exposure. The removal of N-related fluorocarbons was directly observed in the decreased intensity of the N 1*s* spectra [Fig. 4.7(c)]. Based on the C 1*s* spectra, the N 1*s* spectra were primarily composed of NCF_2 and NCF_3 peaks. The comparable intensity reduction between both moieties led to an unchanged center BE for the N 1*s* spectrum. In addition, the oxidation of SiCOH materials is normally reflected in XPS with an increased BE for the Si 2*p* and O 1*s* peaks.[4.2] The post-etching Si 2*p* and O 1*s* BE increased with the subsequent ashing process [Fig. 4.7(d) and 4.7(e)], but the variation was smaller than 0.1 eV. This can be explained by the minimal ULK modification introduced during the CO_2 exposure. Moreover, the dielectric substrate signals including the C-Si peak in C 1*s*, Si 2*p*, and O 1*s* were attenuated by the FC coverage. The partial loss of FC led to the increase of Si 2*p* and O 1*s* intensities. The FC coverage thickness (d_{FC}) can be determined by the attenuation of Si 2*p* intensities using[4.18]

$$d_{FC} = \lambda \cdot \ln\left(I_{0,Si2p} / I_{Si2p}\right) \tag{4.1}$$

Here, λ is the mean free path of a Si 2*p* photoelectron (1383 eV) in the FC layer. $I_{0,Si2p}$ is the initial Si 2*p* intensity from the untreated ULK. λ was set to 3.9 nm. The FC

coverage thickness measured decreased from 1.5 nm to 1.3 nm as the ULK was processed with the CO_2 discharge. Most of the FC coverage remained on the ULK surface at the sidewall position. This supports the fact that the FC sidewall coverage can provide effective protection of the ULK material against damage otherwise introduced by the fluorine-containing CO_2 ashing plasma.

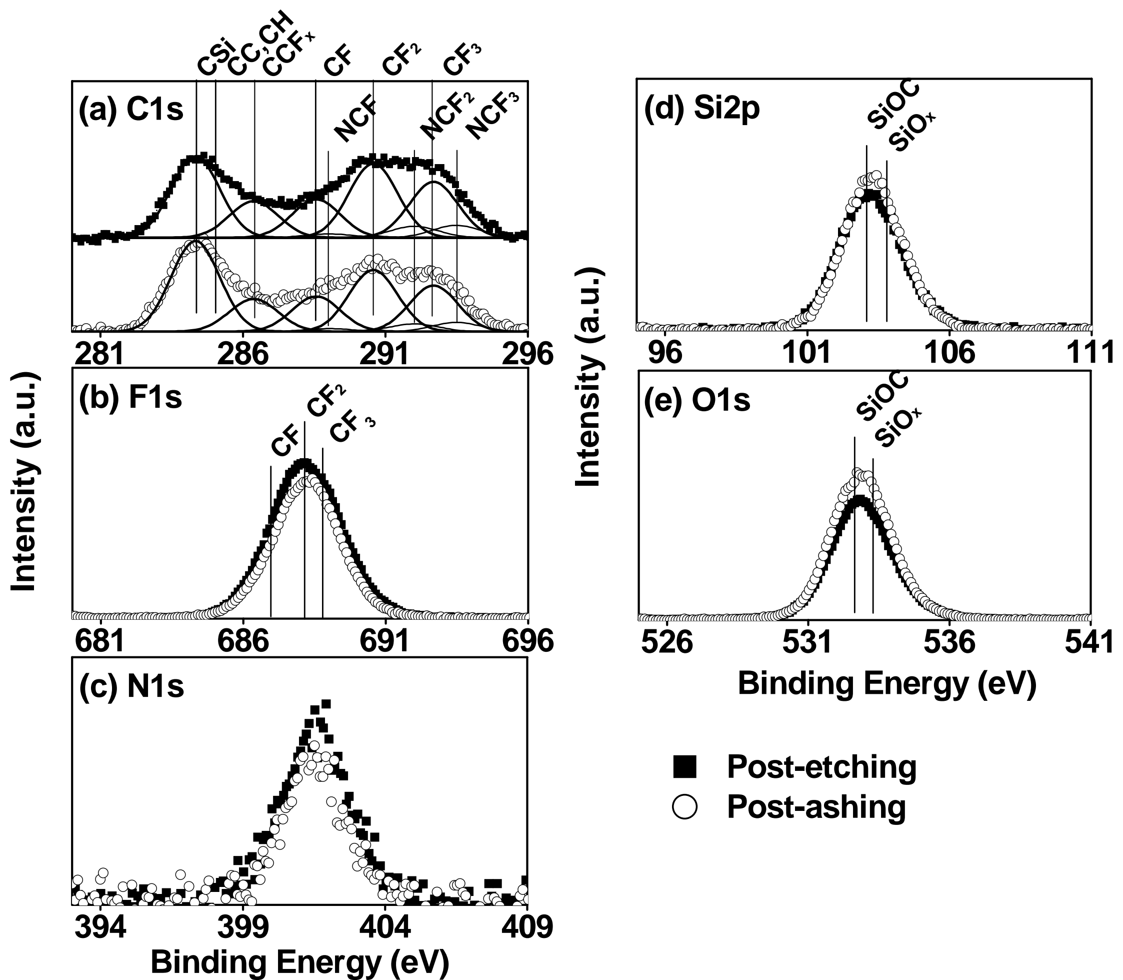

Figure 4.7: XPS C 1*s* and Si 2*p* spectra of untreated, post-etching, and post-ashing ULK in the combined processes. The $C_4F_8/Ar/N_2$ etching process was conducted for 160 s. The subsequent CO_2 *in situ* discharge was maintained for 180 s without bias power applied to the substrate. Both processes were simulated with blanket ULK films in the small gap structure.

4.3.3 Ashing efficiency

In Fig. 4.8, we summarize AE of 10 mTorr CO_2 discharges for a clean chamber and a FC-coated chamber. The PR ashing and ULK damage data are from Figs. 4.2, 4.4 and 4.5. The AE obtained with pristine samples in a clean chamber was ~18. For a combined process sequence, when the chamber was FC contaminated, the ashing plasma became more damaging and the AE decreased to ~3 in the absence of FC film protection on the ULK material. With sufficient FC coverage present on the ULK surface, the underlying ULK was protected. ULK damage in the more aggressive FC coated chamber was reduced, and an AE of 18 was restored. When a substrate bias was applied during *in situ* ashing, the PR ashing rate increased while ULK damage was not affected. This improved AE to ~85.

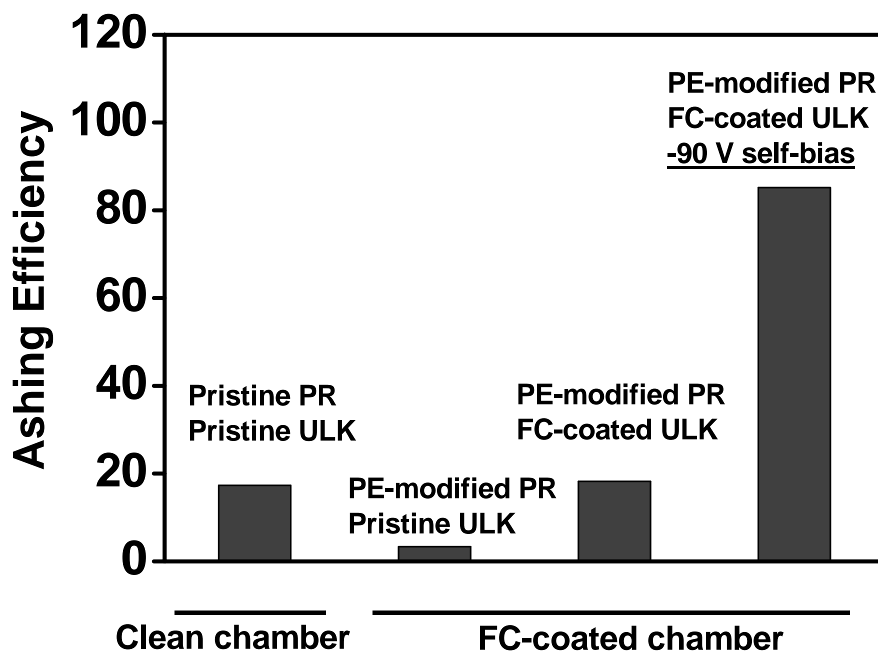

Figure 4.8: Summary of AE for CO_2 *in situ* ashing using a clean chamber and the FC-coated chamber with 10 mTorr CO_2 discharges for 180 s.

4.3.4 Validations using actual pattern transfer process sequence

The etching/*in situ* ashing process interactions were evaluated using patterned films. A patterned layer stack consisting of line and space features was formed on a 400 nm thick ULK film. From the top, it consisted of a 260 nm thick layer of a 193 nm PR, a 70 nm thick organic bottom antireflection coating (BARC), and a 50 nm thick SiC hard mask. A SiC etch stop layer (ESL) layer was employed under the ULK film. The pattern was transferred using $C_4F_8/Ar/N_2$ plasma etching employing the same conditions as used for the blanket film studies. For experiments where ULK trench etching was performed on the ESL layer, an issue was damage to the

ULK/ESL interface and ULK films peeling off when the structures were dipped into the DHF solution used to delineate the ULK damage. We therefore under-etched the ULK trenches. Figure 4.9(a) shows cross-sectional SEM images of post-etching trench structures. A 300 nm deep trench feature was formed in the ULK layer while a 200 nm thick PR layer remained in the structure. The trenched samples were subsequently processed using CO_2 discharges maintained at either 10 mTorr or 100 mTorr without bias for 200 s. The post-ashing SEM images in Figs. 4.9(b) and 4.9(c) show a partial removal of the PR/BARC layers. The removed thickness of ~225 nm for 100 mTorr and ~110 nm for 10 mTorr were quantitatively consistent with results obtained from the blanket film studies and proved the effects of process interaction on PR ashing. The concomitant ULK damage was evaluated using DHF selective etching. ULK damage is defined as the ULK sidewall loss as a result of the CO_2 plasma exposure and subsequent DHF treatment. Post-DHF SEM images for 10 and 100 mTorr CO_2 plasma ashing are shown in Figs. 4.9(d) and 4.9(e), respectively. Figure 9(e) shows that the ULK film after 100 mTorr ashing exposure was completely lost, indicative of excessive ULK damage. The ULK film after 10 mTorr exposure showed an undercut under the hard mask. Figure 4.9(e) indicates a ULK damage thickness of more than 100 nm for 100 mTorr CO_2 ashing. For the 10 mTorr case, ULK damage was estimated at the location shown in Fig. 4.9(d), and was found to be approximately 25 nm deep. This value is greater than the damage depth of ~ 10 nm measured for the blanket film (see Fig. 4.5). The A/R of ~6 of our trench structures was lower than the effective A/R of the gap structure used for the blanket film studies, which was ~15. It is possible that for the reduced A/R of 5, off-normal ion

bombardment and a higher reactive neutral flux explains the discrepancy between the actual trench structures and the simulation using blanket films and the gap structure.

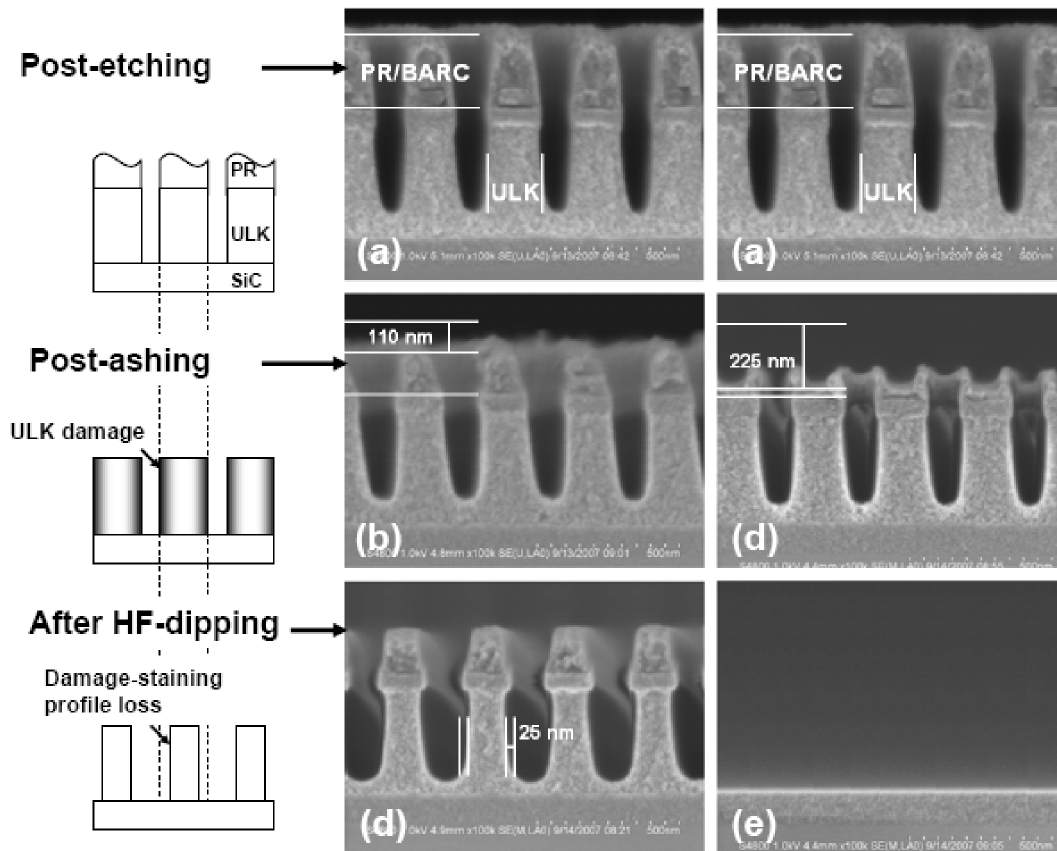

Figure 4.9: SEM cross-sectional profiles of ULK trenches etched using (a) $C_4F_8/Ar/N_2$ etching plasma for 100 s, (b) subsequently *in situ* ashed by 10 mTorr CO_2 plasma or (c) 100 mTorr CO_2 plasma without substrate bias applied, and finally dipped into 0.5% DHF/ 15 s for damage evaluation. [(b)→(d), (c) →(e)].

Figure 4.9 confirms that to minimize ULK damage during PR ashing, low pressure *in situ* ashing processes are best. To increase the ashing rate at low pressure and rapidly attack the plasma etching-modified PR layer, we applied a -90 V self-bias to the substrate. The post-ashing images are shown in Fig. 4.10(b). Even though PR

residues were observed on the HM layer, most of the PR was removed. We estimate that ~270 nm PR/BARC thickness was removed. The effective ashing rate calculated by the total PR/BARC thickness removed over the processing time was ~160 nm/min, which was about 5x improved relative to an ashing rate of ~30 nm/min rate for the unbiased substrate. The post-DHF image [see Fig. 4.10(c)] indicates a ULK damage depth of ~13 nm for the 100 s exposure. From the unbiased to the biased cases, the reduction of damage from 25 to 13 nm is consistent with the reduction of processing time from 200 to 100 s. This suggests that no additional damage due to the substrate bias can be seen using the DHF method. Overall, the AE of the 10 mTorr CO_2 ashing discharge measured using actual trench structures was improved by a factor of 5 by applying -90 V self-bias to the substrate as compared to the unbiased substrate. The self-bias thus enabled a satisfactory PR ashing rate while maintaining low ULK damage for the CO_2 *in situ* PR ashing process.

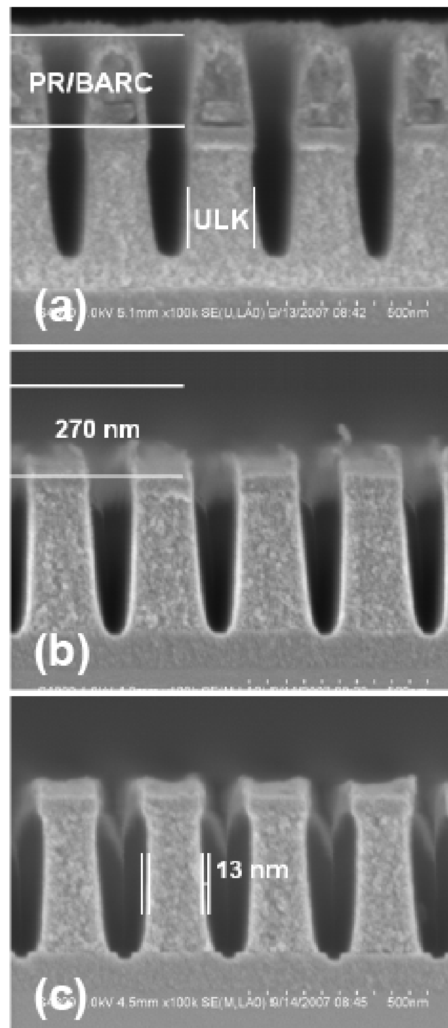

Figure 4.10: SEM cross-sectional profiles of ULK trenches etched using (a) $C_4F_8/Ar/N_2$ etching plasma for 100 s, (b) subsequently *in situ* ashed by 10 mTorr CO_2 plasma without -90 V self-bias, and finally dipped into 0.5% DHF/ 15 s for damage evaluation.

4.4 Conclusions

We have investigated combined CCP $C_4F_8/Ar/N_2$ plasma ULK etching/ CO_2 *in situ* PR ashing processes using blanket materials and actual 193 nm PR patterned ULK trench structures that enable satisfactory PR ashing rates and ULK trench sidewall damage. CO_2 *in situ* ashing plasma operated at low chamber pressure

enabled high ashing efficiency if an RF bias was applied to the substrate, without increasing ULK damage. We showed that gas phase chemistry changes related to the chamber history effects for FC plasma etching processes made CO_2 discharges more reactive during subsequent *in situ* PR ashing and introduced higher ULK damage levels for unprotected ULK films. We found that the PE-process-related FC film coating deposited on ULK sidewalls during plasma etching provided effective protection of the ULK, and played an essential role for maintaining low ULK damage for the CO_2 *in situ* PR ashing process in this situation.

ACKNOWLEDGEMENTS

Financial support of this work by the Semiconductor Research Corporation's Center for Advanced Interconnect Sciences and Technology (CAIST) under Task ID: 1292.023 is gratefully acknowledged. We would like to thank Lam Research for supplying the photoresist and ULK materials.

Chapter 5: Surface and Near-surface Modifications of Ultralow Dielectric Constant Materials Exposed to Plasmas under Sidewall-like Conditions

To be submitted to J. Vac. Sci. Technol. B, 2010

M.-S. Kuo and G. S. Oehrlein

ABSTRACT

We describe the temporal evolution of the surface and near-surface regions of a porous SiCOH ultralow-k (ULK) dielectric during exposure under sidewall-like exposure conditions to various plasma processing environments. We studied the exposure of the ULK material to Ar plasma, C_4F_8/Ar-based etching plasma, and O_2 or CO_2 plasmas, as well as various sequences of these processes. Real-time monitoring of the ULK surfaces during plasma processing was performed by *in situ* ellipsometry employing a novel gap structure. Additionally, changes in ULK surface properties were characterized by X-ray photoelectron spectroscopy (XPS) and selective dilute hydrofluoric acid (DHF) wet etching in combination with *ex situ* ellipsometry measurements.

Pristine ULK material exposed to O_2 plasma without ion bombardment shows the formation of a near-surface porous layer. For exposure of the ULK to CO_2 plasma operated at comparable plasma operation conditions, the modification depth for a given exposure time is reduced relative to O_2, but otherwise an identical ellipsometric

trajectory is followed. This is indicative of a similar ULK damage mechanism for the two discharges, although at different rates. Energetic (~400 eV) ion bombardment on the surface of ULK with line-of-sight Ar plasma exposure introduced a ~ 12 nm thick SiO_2-like densified layer on the ULK surface meanwhile sputtering off the ULK material. The sidewall-like modifications of ULK due to metastable Ar, if present, were too subtle to be measureable in this work.

For ULK exposed under sidewall-like geometry to C_4F_8/Ar-based etching plasma, fluorocarbon quickly permeated into the subsurface region and showed saturation at a mixed layer thickness of about 15 nm. For additional exposure to O_2 or CO_2 discharges, a strong decrease of the O_2 or CO_2 plasma induced ULK surface modifications with increasing fluorocarbon (FC) film thickness was found, indicative of surface protection by FC surface deposition along with pore-sealing by the FC material. Attempts to increase the protective nature of the FC film by additional plasma processing, e.g., by exposure to Ar or He plasma after FC plasma etching, did not reduce O_2 or CO_2 plasma induced ULK surface modifications further.

5.1 Introduction

The 2007 International Technology Roadmap for Semiconductor (ITRS)[5.1] highlights the problem of dielectric constant degradation during process integration of porous ultralow-*k* (ULK) dielectric materials. One key contributor to the degradation (increase) of the dielectric constant of ULK materials is damage inflicted during the combination of plasma etching of ULK and stripping of the photoresist mask.[5.2-5.3] For porous ULK materials, the diffusivity of reactant during processing is dramatically increased relative to non-porous materials. Significant surface and near-surface modifications take place during plasma etching and photoresist stripping, including carbon loss from the trench/via sidewalls and densification during PR stripping, and increase the dielectric constant.[5.4-5.7] For the combination of plasma etching and photoresist *in situ* ashing, process interaction is likely to occur on trench sidewalls and influence the ULK ashing damage.[5.8-5.9] Pore-sealing by etching process by-products deposited on the ULK trench sidewalls may be a compelling strategy to protect ULK materials during subsequent process steps.[5.10-5.11]

This work seeks to establish the factor that determines the ability of etching-process-related residues/plasma surface modification of trench sidewalls of porous ULK dielectric to protect the ULK materials during subsequent *in situ* ashing processes. Our objective was to establish a relationship between the fluorocarbon etching processes and the post-ashing damage levels that are inflicted on the ULK sidewall.

5.2 Experimental Setup and Procedures

The ultralow k material used in this work was a ~500 nm CVD-based porous SiCOH film with k~2.2 on silicon wafers. The porosity was induced in the silicon-oxide-based CVD film by ultraviolet curing.[5.12] The overall porosity was above 25% based on nanopores with an average diameter of ~1 nm.[5.13]

Experiments addressing plasma etching, ULK surface modification by Ar plasma exposure, ashing and combinations of these processes were all performed in a dual frequency capacitively coupled plasma system (see Fig. 1.2) with the substrate temperature maintained at 10 °C using active cooling of the substrate electrode.

In this work, sidewall-like plasma exposures of the ULK were performed utilizing a silicon roof that shielded the ULK film, located underneath, from direct ion bombardment. The aspect ratio (A/R) of the small gap structure was selected to be equal to that of actual trench structures. This enables simulation and surface studies of trench sidewall-like surface modifications induced by etching processes, along with the determination of their impact on ashing damage introduced during the subsequent PR stripping process. The setup has been described in Sec. 2.2. For the present work, a roof width of 39 mm and a gap height of 1.3 mm were used for the gap structure. This produces an A/R of about 15 for a sample positioned at the center of the gap structure, similar to A/R encountered in actual trench structures. Ellipsometry has been widely used for real-time monitoring of material modification during plasma processing.[5.14,5.15] For materials processed in a small gap structure, the silicon roof blocks the probing laser beam and prevents ellipsometry characterization. To enable real time *in situ* ellipsometric monitoring of ULK materials exposed to plasma under

sidewall-like conditions, the “regular roof” [see Fig. 5.1(a)] was modified in the fashion illustrated in Fig. 5.1(b) and will be referred to as the “ellipsometric roof”. On the Si roof, an aluminum block was mounted. Through the aluminum block and the Si roof, a tunnel was created for the probing laser beam, enabling *in situ* ellipsometry characterization of the ULK surface. The length of the tunnel is large, and the A/R of the laser tunnel is much greater than the A/R of the gap structure. During plasma processing, the high-aspect-ratio tunnel prevents ions from reaching the sample surface. Neutrals may be able to diffuse through the tunnel, but the flux is expected to be much lower than the neutral flux entering the gap structure laterally. This structure is compatible with *in situ* ellipsometric monitoring and enables probing of ULK surfaces under sidewall-like plasma exposure by ellipsometry.

As compared with the interelectrode gap distance, the height of the roof in Fig. 5.1(b) was significant and could not be neglected. Its presence may influence plasma properties, e.g., plasma density. To avoid heating the roof and to prevent aluminum sputtering, which would lead to plasma and surface contamination, no bias power was applied to the substrate during processing using the setup of Fig. 5.1(b). Plasma operation was therefore different for the cases where real-time ellipsometry monitoring under sidewall-like conditions was performed [Fig. 5.1(b)] as compared to exposure of actual PR-patterned ULK structures or blanket ULK exposures using the roof of Fig. 5.1(a). However, the defining characteristics of sidewall-like exposure using a roof structure, namely, preventing ion bombardment of the ULK surfaces and exposing ULK surfaces to a plasma-generated neutral flux modified by multiple collisions at opposing surfaces are the same for Figs. 5.1(a) and 5.1(b). This suggests

that characteristic sidewall-like ULK modifications may be studied using the approach illustrated in Fig. 5.1(b).

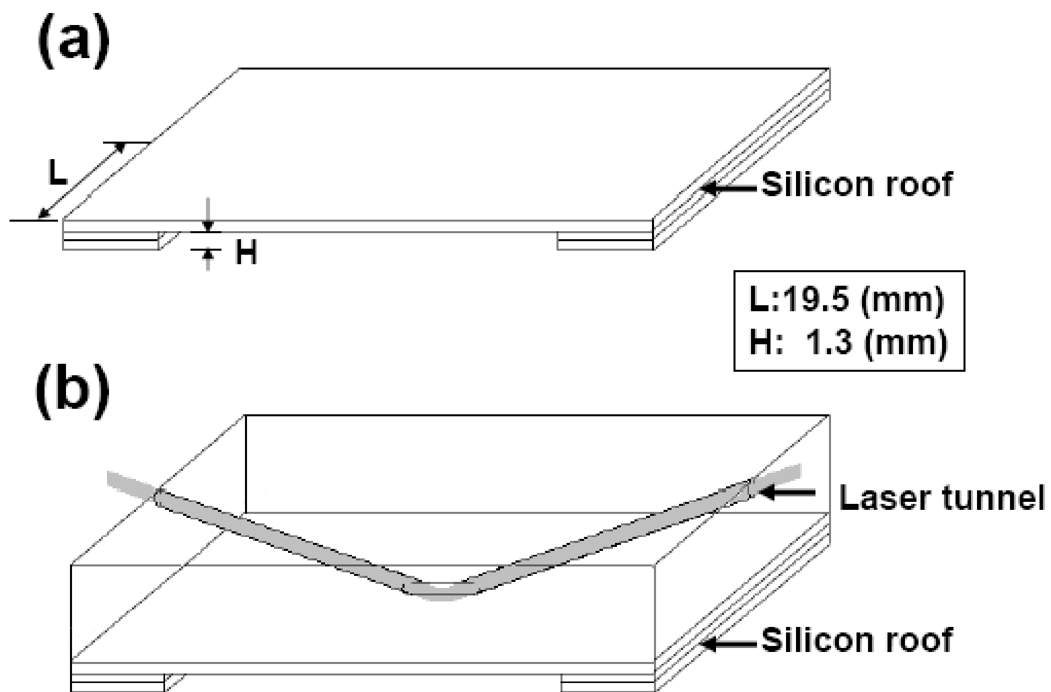

Figure 5.1: Schematic of the small gap structure using the regular roof (a) and the ellipsometric roof (b), which supports *in situ* ellipsometry characterization.

The experiments to be described are grouped into two sections, and the discharge parameters are summarized in Table 5.1. In the first section, studies with the ellipsometric roof allowed us to obtain information on the temporal evolution of ULK materials during sidewall-like plasma exposure by *in situ* ellipsometry. The sidewall-like modifications of ULK using 10% C_4F_8/Ar etching plasma, and CO_2 and O_2 *in situ* ashing plasmas were individually studied. Effects of the Ar plasma species, including metastable Ar and Ar ions on ULK modification, on ULK surface

modification were also studied using remote and line-of-sight exposure monitored by real-time ellipsometry. This knowledge provides insight into plasma sidewall interaction of porous ULK.

In the second part, the influence of fluorocarbon etching and their combination with CO_2 and O_2 *in situ* ashing plasmas on ULK surface modifications were investigated using the regular roof structure. For this part of the work, the materials were characterized after plasma treatment using X-ray photoelectron spectroscopy (XPS), and the ULK damage was quantified by dilute hydrofluoric acid (DHF, 0.5%) selective etching. For *ex situ* and *in situ* ellipsometry measurements, we used two different ellipsometers operated in the polarizer-compensator-sample-analyzer (PCSA) configuration with a 632.8 nm He/Ne laser source beam incident at an angle near 73° from the surface normal.

Discharge Chemistry	C_4F_8/Ar-based	Ar	O_2 or CO_2
Material Process	ULK etching	ULK surface tailoring	*In situ* PR ashing
Top electrode (40.68 MHz)	200 W	120 W	200 W
Bottom electrode (4 MHz)	0 or ~100 W	0 or 100 W	0 W
Chamber pressure	30 mTorr		10 mTorr
Total gas flow rate	40 SCCM		

Table 5.1: Discharge parameters used in this work. For real time study of ULK plasma modification, ULK films were respectively exposed to C_4F_8/Ar, Ar, and O_2 or CO_2 plasma under an ellipsometric roof and monitored by real time ellipsometry. The effects of Ar ion bombardment (100 W bias power applied) were also studied using ULK film with line-of-sight Ar plasma exposure. For the study of etching/ashing process interaction, ULK films under a regular roof were processed with the different C_4F_8/Ar etching followed by a standard CO_2 *in situ* ashing processes. Post-ashing damage was quantified by DHF method.

5.3 Results and Discussion

5.3.1 Real-time Ellipsometric Study for Individual Processes

The temporal evolution of ULK surface modifications due to plasma exposure was monitored by real-time ellipsometry, and the data was analyzed by optical modeling.

A. CO_2, and O_2 Ashing Plasma Sidewall-like Modification

Measured ellipsometric trajectories for ULK exposed to O_2 and CO_2 ashing plasmas under a sidewall-like condition are shown in Fig. 5.2(a) and 5.2(b) as a close-up. A "compass" in Fig. 5.2(c) illustrates the ellipsometric trajectories expected for

different material modifications. The initial refractive index (*n*) of the pristine ULK was 1.320. A decrease in the refractive index of the plasma-modified ULK was observed due to exposure to the O_2 plasma. The decreased refractive index suggests increased porosity. If we assume the formation of a highly porous layer, a refractive index of 1.248 (corresponding to highly porous SiCOH, e.g., JSR LKD 5109) may be appropriate to describe its properties.[5.16] The film porosity can be estimated from the refractive index of porous silica (n_p) using the Lorentz-Lorenz equation[3]

$$\frac{(n_p^2-1)}{(n_p^2+2)} = P\cdot\frac{(n_1^2-1)}{(n_1^2+2)} + (1-P)\cdot\frac{(n_s^2-1)}{(n_s^2+2)}, \qquad (5.1)$$

where n_p is the refractive index of porous ULK, and n_s and n_1 are the refractive indices of the film skeleton and of the material inside the pore, respectively. *P* is the porosity. If the pore is empty, then n_1=1, and the porosity (*P*) is given by

$$P = 1 - \left[\frac{(n_p^2-1)}{(n_p^2+2)}\right] \Bigg/ \left[\frac{(n_s^2-1)}{(n_s^2+2)}\right]. \qquad (5.2)$$

n_s=1.465 (silica) was set. For a refractive index of 1.32 for pristine ULK and 1.248 assumed for oxygen-damaged ULK, porosities of *P*=28 and 43% were obtained, respectively. The increase in porosity can correspond to an increase in pore size. The ellipsometric data show that when pristine ULK was exposed to remote oxidizing plasma, some of the ULK was converted into a porous layer. This finding is consistent with observations by Shamiryan *et al.*,[5.17] who also observed a decrease of the refractive index due to remote O_2 plasma exposure near room temperature. They explained their observations by pore size enlargement of porous ULK. We used a

two-layer optical model to interpret the ellipsometry data. We employed a refractive index n=1.248 for the plasma-modified layer and n=1.320 for the unmodified ULK. We assume the formation of a plasma-modified layer with a constant refractive index. In Fig. 5.2(a), curve 1 (solid squares) corresponds to simulation results for an unexposed (unmodified) ULK film (n=1.320) of decreasing thickness on a Si substrate [the separation of points in the direction of the arrow equals to 20 nm thickness decrease in Fig. 5.2(a)]. The family of curves 2 (open squares) shows the effect of adding plasma-modified overlayers (n=1.248) of increasing thickness on unmodified ULK films (n=1.320) with a given thickness. Each modeled line of the family of curves 2 correspond to a given constant thickness of the underlying unmodified ULK layer while the thickness of the plasma-modified overlayer is increased. The increment of thickness in the arrow direction is 1 nm. As we follow experimental trajectories, each line 2 that is crossed corresponds to a plasma-modified overlayer of increasing thickness grown on an unmodified film with reducing thickness. Fig. 5.2 shows that there is a correspondence of the increase of the plasma-modified layer and the thickness reduction of the unmodified ULK layer. If the transformation of ULK film into a plasma-modified layer would occur without loss of Si-based skeleton, the plasma-modified layer would be thicker than the converted ULK film (this corresponds to the end of each of the curves 2) due to the lower film density in the highly porous plasma-modified layer. According to the simulation, for instance, the plasma-modified layer thickness was approximately 49 nm, corresponding to a 40 nm converted ULK film. The total thickness peaked at ~80 s (point a) as 509.4 nm, and subsequently decreased with exposure time. This shows

that erosion occurred simultaneously with conversion of plasma-modified layer. It may be explained by some Si skeleton material loss due to volatile product formation. The comparison of the data with the model results shows that the removal rate of the highly porous layer was slower than the growth rate of highly porous layer from the conversion of the ULK film for all times examined here The thickness of the highly porous layer did not reach steady-state for exposure time up to 300 s for our O_2 experimental conditions. The modification found for CO_2 plasma was less than that measured with O_2 plasma; however, it followed a trajectory that was nearly identical to that seen for O_2 plasma, indicative of the similar nature of the modified ULK surface regions.

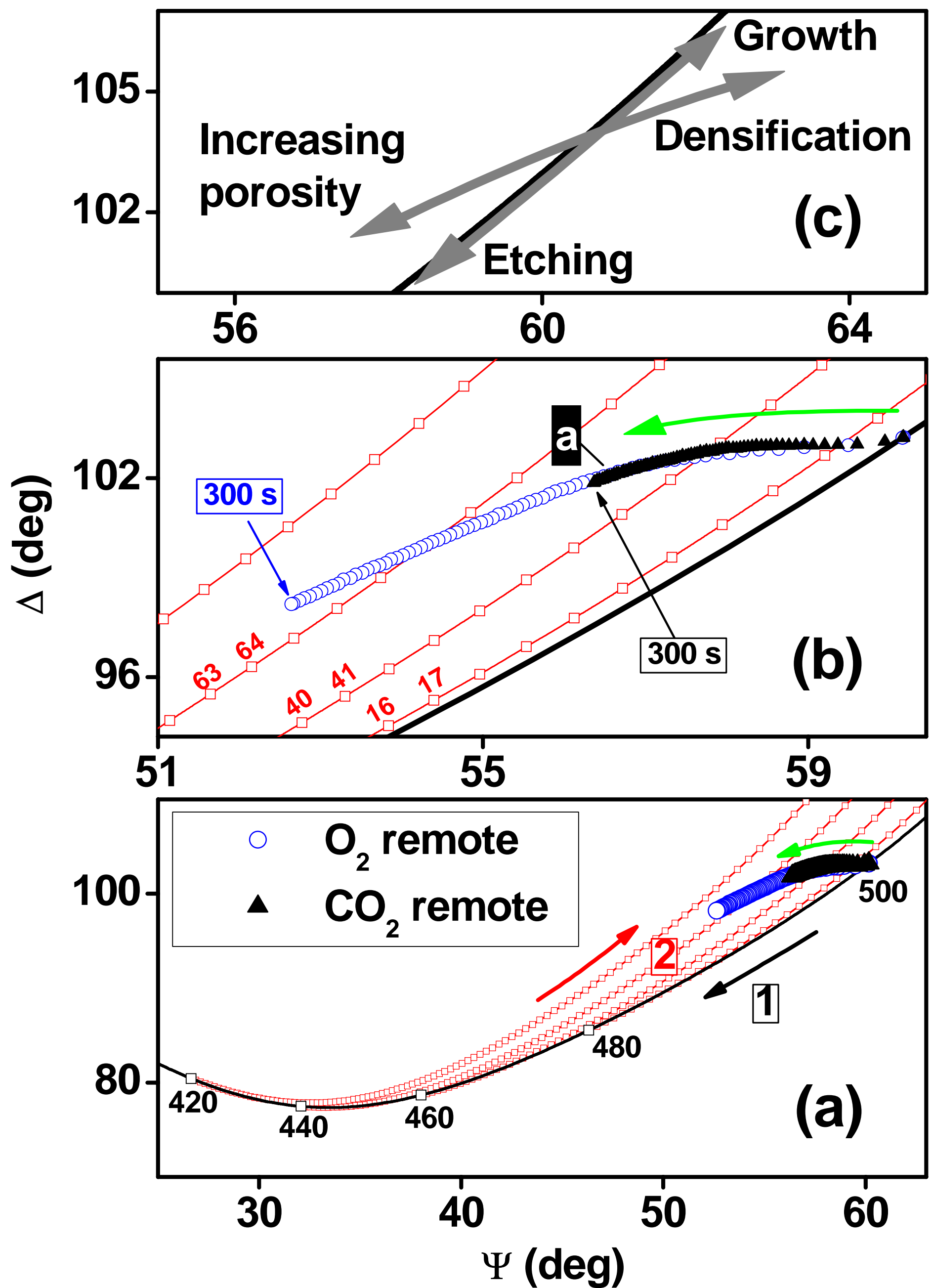

Figure 5.2: (a) Real-time ellipsometric Ψ-Δ trajectories for ULK exposed to remote O_2 and CO_2 plasmas using the ellipsometric roof (remote). Modeled curves based on two-layer structure comprising the highly porous overlayer (n=1.248) and modified ULK film (n=1.320) are superimposed. Initial thickness of ULK film was 500 nm. Figure (b) shows a close-up for the experimental trajectories. The "compass" in figure (c) indicates general directions of trajectories for deposition or erosion, and changes in (optical) material density.

The thickness loss of the unmodified ULK obtained in Fig. 5.2(b) is interpreted as ULK damage. The ULK damage thickness for O_2 and CO_2 plasma are shown in Fig. 5.3 as a function of exposure time. The ULK damage introduction rate was initially fast and subsequently slowed. This may be explained by plasma reactant diffusion effects through the plasma-modified layer. For our process conditions, ULK damage had not reached saturation after 300 s. In Fig. 5.3, ULK damage values after 300 s plasma exposure obtained by the DHF method are shown for comparison. For O_2 plasma, the same ULK damage values were found for the two methods, lending support for the assumed refractive index of n=1.248 for the damaged ULK. For CO_2 plasma, less ULK damage was seen for the DHF method as compared to the damage depth found from ellipsometric modeling. A possible explanation of the lower damage depth given by DHF relative to ellipsometric modeling may be the existence of an extended damage profile after CO_2 plasma processing, where a region with a low level of ULK damage exists that could not be dissolved in DHF.

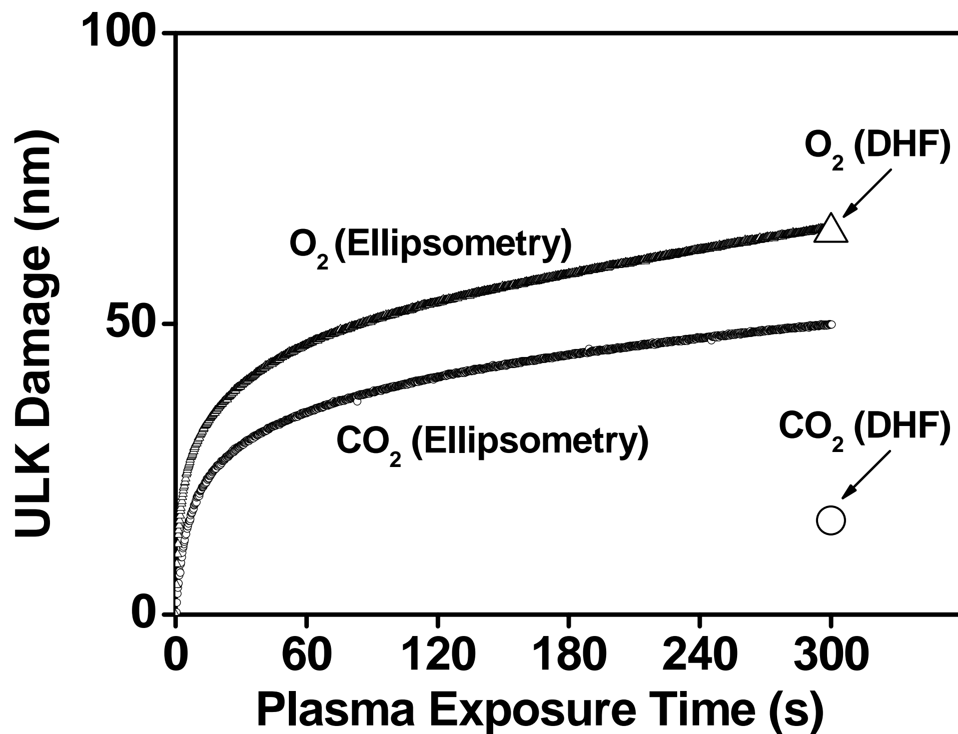

Figure 5.3: ULK damage as a function of exposure time obtained by optical two-layer modeling with refractive index *n*=1.248 for the plasma-modified layer (see Fig. 5.2). The ULK damage depth obtained with the DHF method for 300 s CO_2 and O_2 plasma exposure is included for comparison.

B. Ar Plasma Modification

The measured trajectories for ULK with either remote or direct Ar plasma exposure are displayed in Fig. 5.4. For the direct exposure, as noted in Fig. 5.2(c), its trajectory shows an increasing density together with a decreasing thickness of the ULK material. This indicates that Ar ion bombardment resulted in surface densification.[5.18] A two-layer model based on the refractive index *n*=1.465 for the densified silica layer was adopted for the simulation. The movement of Ψ-Δ takes place on a curve (ii) that is parallel to the curve (i) which simulates an unmodified

ULK with varying thickness. The experimental trajectory is fitted by a simulated curve of a ULK film of varying thickness underneath a 12 nm densified silica (n=1.465) layer. The steady leftward movement of Ψ-Δ points shown in the figure is explained by ULK thickness loss due to sputtering. The measured Ar sputtering rate was 50 nm/min. In addition, sidewall-like (remote) exposure for Ar plasma caused much less of a modification. As compared with O_2 trajectory shown in Fig. 5.2, the trajectory suggests a modification similar to that seen for O_2 and may be explained by residual oxygen in the discharge.

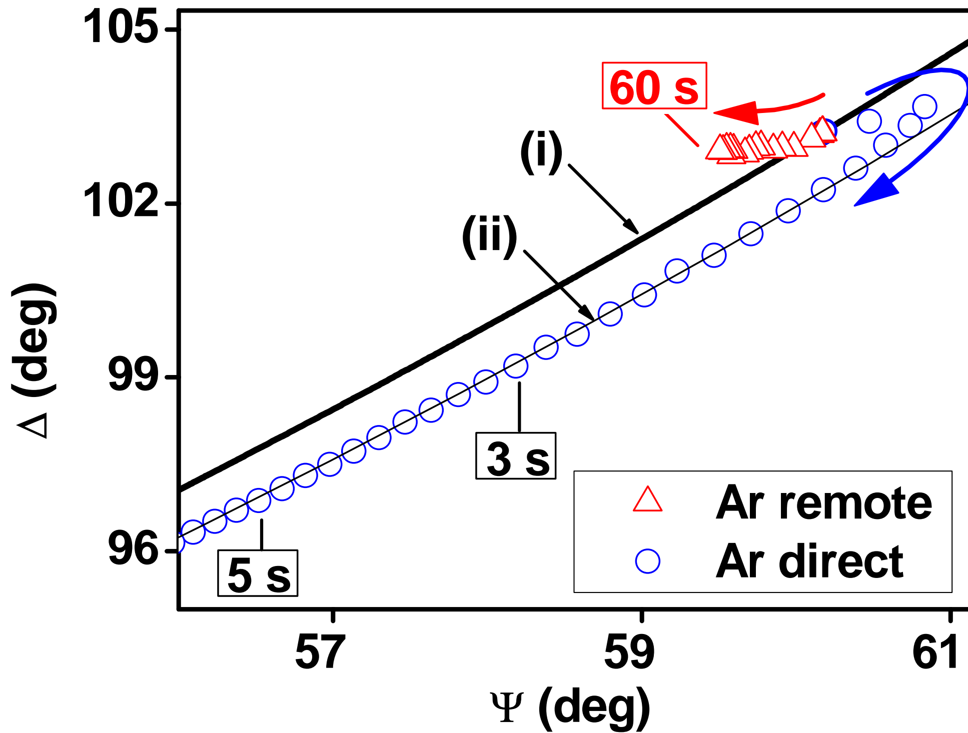

Figure 5.4 Real-time ellipsometric Ψ-Δ trajectories for ULK exposed to remote or direct Ar plasma. The Ψ-Δ simulated trajectories of unmodified ULK film (n=1.320) with varying thickness and constant refractive index are shown with curve (i). Also, the Ψ-Δ simulated trajectory for a constant 12 nm silica-like densified layer (n=1.465) on top of a varying thickness of unmodified ULK is shown with curve (ii). Initial ULK film thickness was 500 nm.

C. C_4F_8/Ar etching Plasma Sidewall-like Modification

Modifications of ULK induced by sidewall-like exposure to C_4F_8/Ar plasma etching processes were studied employing blanket ULK films in the small gap structure and real-time ellipsometric monitoring. A typical Ψ-Δ trajectory is shown in Fig. 5.5(a). We found that when FC penetrates into and fills the nanopores of a porous structure, the effective refractive index increases due to the elimination of the pores.

When a pore is completely filled with FC material (n_1=1.4), the refractive index of the FC permeated ULK was found from Eq. 5.1 as n=1.446. Modeling was performed for the ULK/FC-mixed layer, and is shown in Fig. 5.5. The two-layer model consists of unmodified ULK and a near-surface ULK region with permeated FC (FC penetrated into the nanopores and produced a mixed layer). The growth of the mixed layer as a function of exposure time based on the modeling of real time data is shown in Fig. 5.5(b) and indicates that the layer was established within about 30 s and then its extent no longer changed. For our processing conditions and assuming the model described, a ~14 nm thick ULK/FC-mixed layer was found.

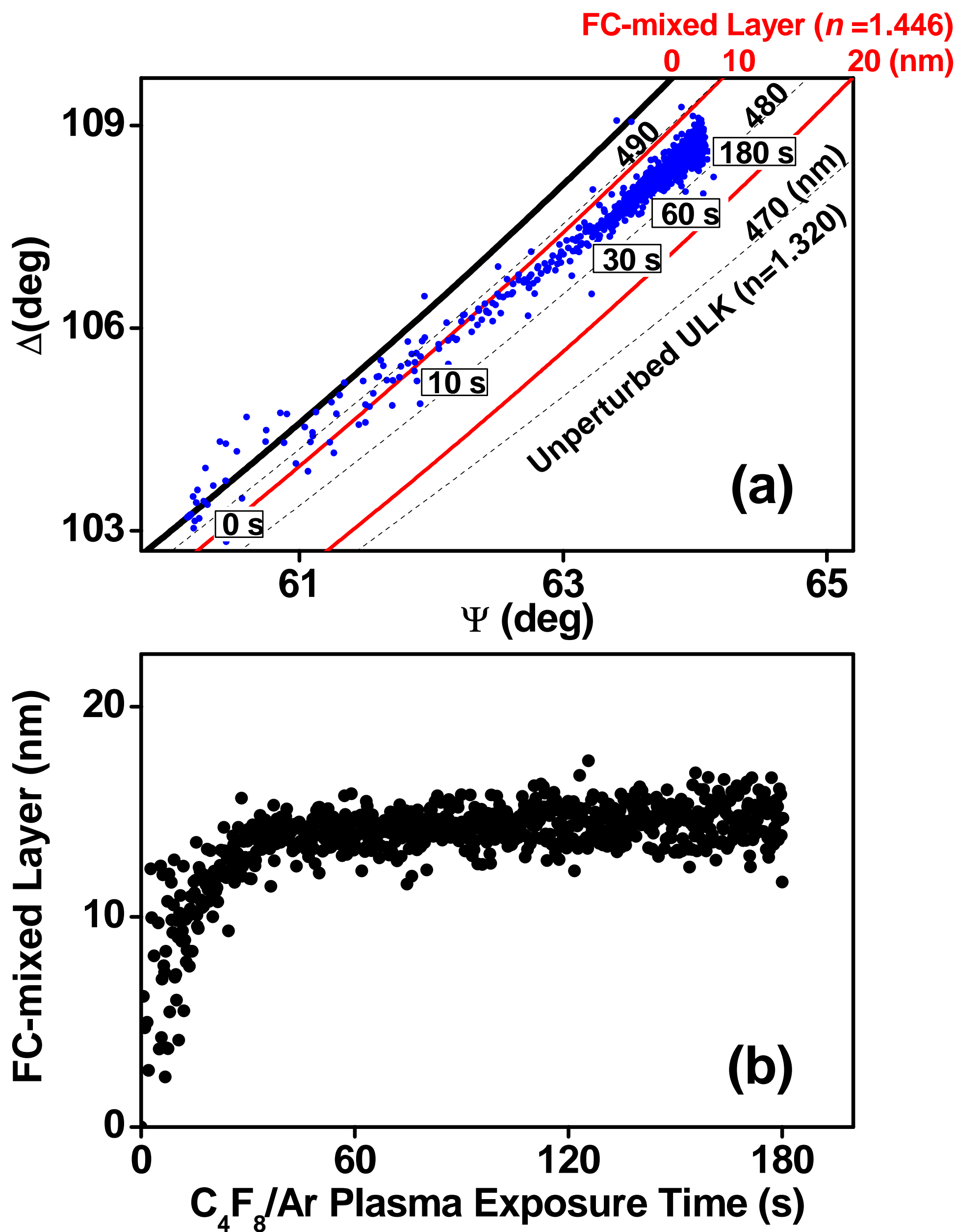

Figure 5.5: (a) Real-time ellipsometric Ψ-Δ trajectories for ULK exposed to 10% C_4F_8/Ar plasma using the ellipsometric roof. Modeled curves based on a two-layer structure comprising the ULK/FC-mixed layer (*n*=1.446) and unmodified ULK (*n*=1.320) are superimposed. Initial ULK film thickness was 500 nm. (b) The ULK/FC-mixed layer thickness is shown as a function of exposure time, and was obtained from the measured trajectories of (a) by optical modeling.

5.3.2 Process interaction

Next, we report on how the introduction of ULK plasma ashing damage changes with the presence of FC-plasma-related ULK surface modifications introduced during a prior plasma etching step.

A. FC Protection: Etching Parameter Dependence

For combined plasma etching/PR plasma ashing sequences, during FC plasma etching fluorocarbon material is deposited on the ULK surface, and prevents interaction of reactive neutrals with the ULK material during subsequent plasma ashing. ULK films were exposed to various C_4F_8/Ar-based etching plasmas in the small gap structure, and then further exposed to a subsequent CO_2 *in situ* ashing plasma. The roof shown in Fig. 5.1(a) was used. Based on our standard etching conditions, source power of 100-300 W, gas pressure of 10-60 mTorr, C_4F_8 ratio of 5-20%, and addition of 5% O_2 and 10% N_2 were each varied at a constant (~ -300 V) self-bias voltage. Fluorocarbon sidewall-like deposition on post-etching ULK surface was characterized by XPS, and used to obtain the FC film thickness on ULK after plasma etching. The ULK plasma damage depth following the CO_2 ashing step was quantified by DHF selective etching.

In Fig. 5.6, we present the relationship of ULK post-ashing damage and FC film thickness deposited during the FC plasma etching step. The parameters used for the FC plasma etching step are shown. In addition, selected C 1s and Si 2*p* spectra after three plasma etching processes for which the C_4F_8/Ar ratio was varied are displayed in Fig. 5.6. The C 1*s* spectra showed the characteristic C-Si/C-C signal of

the SiCOH material and peaks assigned to C-CF_x, CF, CF_2, and CF_3 bonds of the fluorocarbon film.[5.19] We found that while the composition of fluorocarbon films produced by different plasma etching conditions employing C_4F_8/Ar with either O_2 or N_2 gas additives was fairly similar, there were significant differences in the FC film thickness. The film thickness (d_{FC}) was determined from the attenuation of the Si *2p* intensity (I_{Si2p}) relative to the initial value using Eq. 4.1.The mean free path of a Si 2*p* photoelectron (1151 eV) in the FC layer was set to 3.4 nm. The FC film thickness after different processing conditions was acquired and correlated with ULK post-ashing damage. In Fig. 5.6 we also show results for post-ashing damage of pristine ULK when exposed to the ashing plasma in a clean chamber, or alternatively in a chamber seasoned with a standard FC plasma etching process. The damage of pristine ULK processed with CO_2 plasmas in a pre-seasoned (FC-coated) chamber was much higher than in a clean chamber and can be explained by the fluorine memory effect.[5.20,5.21] When FC material was present on the ULK surface for plasma etching/ashing process combinations, ULK post-ashing damage was significantly reduced and decreased with increasing FC film thickness. Figure 5.6 shows that ULK post-ashing damage is primarily determined by FC film thickness. Therefore, plasma etching conditions, which enhance FC deposition at the sidewall-like ULK surface, will reduce ULK damage during subsequent exposure to ashing plasma.

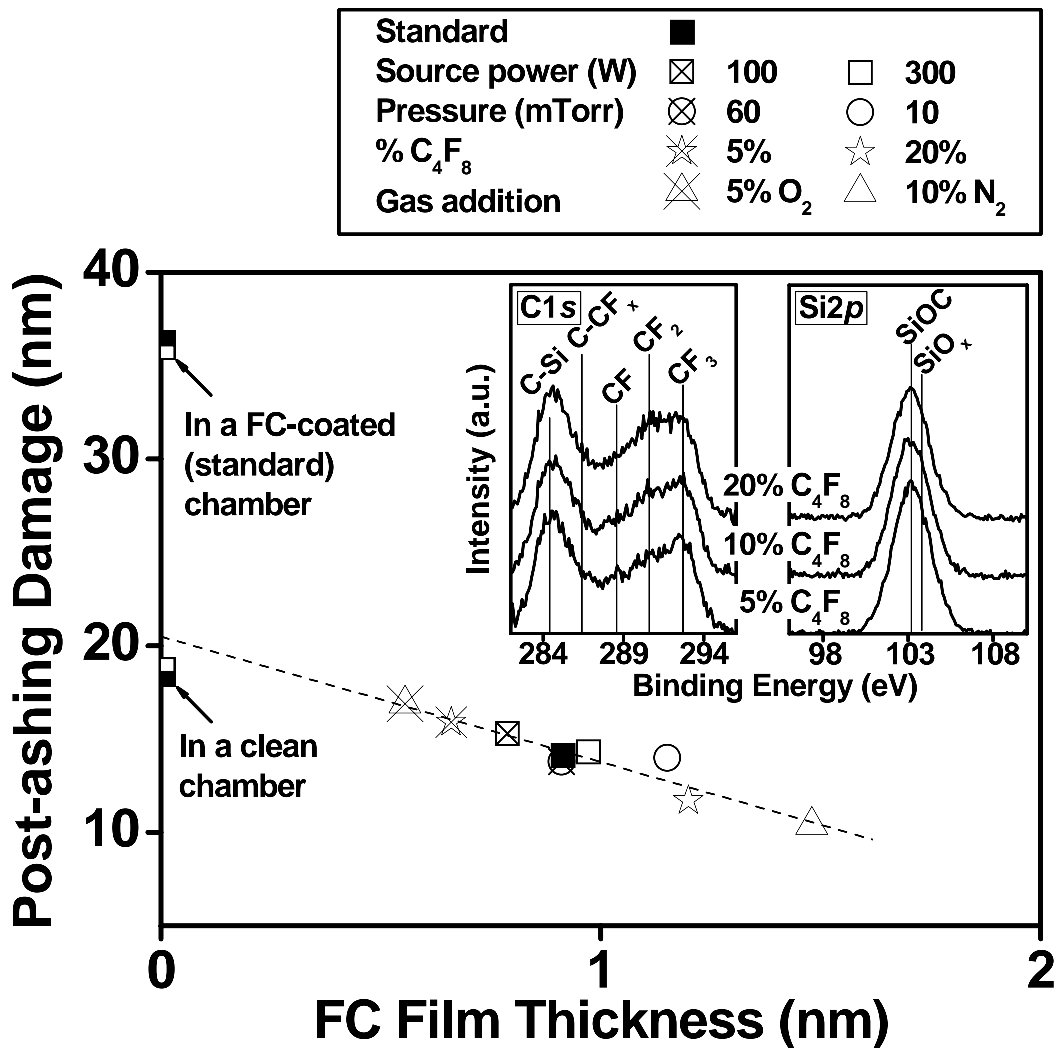

Figure 5.6: Post-ashing damage as a function of post-etching FC film thickness determined by XPS. The standard etching conditions are listed in Table I. The processing time for C_4F_8/Ar-based etching plasma, and subsequent CO_2 *in situ* ashing plasma, were 180 s and 300 s, respectively. The exposures were conducted using a regular roof. For comparison, post-ashing damages of the pristine samples processed in a clean chamber and in a FC-coated chamber seasoned with standard etching conditions are also shown. Post-ashing damage was quantified by the DHF method.

B. FC Protection: Etching Plasma Exposure Time Dependence

In a patterned wafer etching process, the exposure time of ULK sidewalls to the plasma etch environment varies as a function of position from the top surface, possibly leading to a non-uniform ashing damage profile along a trench/via sidewall. We determined ULK post-ashing damage as a function of exposure time of ULK under sidewall-like conditions to a 10% C_4F_8/Ar plasma. To avoid the interference of the fluorine memory effect, the subsequent CO_2 ashing plasma exposures of the processed ULK were performed in a clean reactor. The results are displayed in Fig. 5.7. We observe that the ULK post-ashing damage decreased strongly with time the ULK was exposed to the FC plasma. This observation (Fig. 5.7) correlates well with the temporal evolution of FC film thickness shown in Fig. 5.5.

The results of Fig. 5.7 suggest that additional FC sidewall deposition, e.g. by a brief no-bias exposure of ULK to FC plasma, may be used as a means to increase ULK protection by FC film for conditions that provided insufficient FC film on ULK sidewalls, or to make FC coating more uniform as a function of trench/via depth. We also performed experiments aimed enhancing the FC film protection efficacy during CO_2 ashing by additional post-etching inert plasma exposures. Such treatments could presumably lead to densification of the mixed FC-ULK layer formed on the ULK surface and render it more impermeable to reactive species generated in the CO_2 ashing plasma. Exposure of FC films to Ar or He discharges under sidewall-like exposures introduced negligible modification of the FC films. Conversely, low-energy Ar (or He) direct ion bombardment destroyed the deposited FC films and led

to the complete loss of the ULK protection by the FC film during the subsequent ashing process.

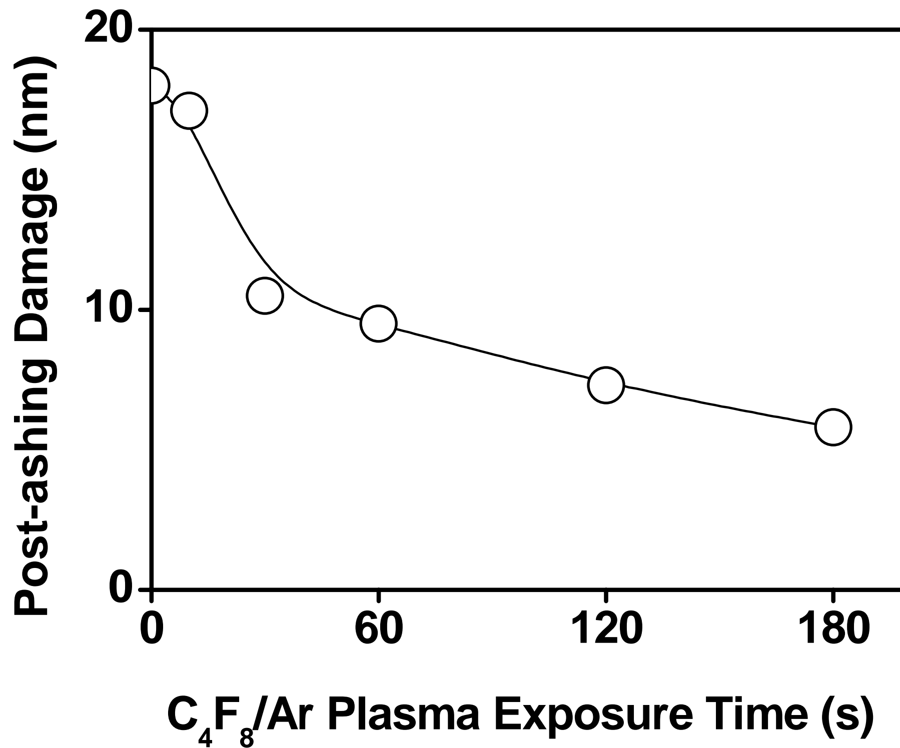

Figure 5.7: ULK post-ashing damage measured for a FC etching plasma/CO_2 ashing plasma combination as a function of ULK exposure time to the 10% C_4F_8/Ar plasma. We employed 300 s CO_2 ashing plasma exposure, regular roof, and post-ashing damage was quantified by the DHF method.

5.4 Conclusions

We demonstrated a novel roof approach that allowed us to perform real-time *in situ* ellipsometry monitoring of ULK surfaces during exposure to plasma under sidewall-like conditions. Measured ellipsometry trajectories were interpreted using

appropriate optical models. For O_2 and CO_2 ashing processes, we observed the formation of a porous layer near the ULK surface. No saturation of the ULK modification was observed up to 300 s processing time. The ULK damage induced by CO_2 plasma was less than that induced by O_2 discharges, but the Ψ-Δ data followed the same trajectory as measured with O_2 plasma. This indicates a similar ULK damage mechanism for sidewall-like exposure to O_2 or CO_2 plasma, although the rate of damage introduction was smaller for CO_2 plasma. During exposure of ULK to a remote C_4F_8/Ar etching plasma, we observed the generation of a ULK/FC-mixed near-surface layer. The mixed layer was rapidly established and saturated at a thickness of ~14 nm, and can be explained by permeation of FC material into the pores of the ULK. For plasma etching/ashing process sequences, the FC mixed layer was found to provide significant protection to the ULK sidewall from damage during CO_2 plasma exposure used for PR ashing. While the composition and nature of the FC film formed on ULK were not significantly changed by varying plasma etching parameters over the range of process conditions examined here, the equivalent FC film thickness changed significantly. Post-ashing ULK damage was significantly reduced by employing plasma etching processes that produced thicker FC films under sidewall-like deposition conditions.

ACKNOWLEDGEMENTS

Financial support of this work by the Semiconductor Research Corporation's Center for Advanced Interconnect Sciences and Technology (CAIST) is gratefully

acknowledged under Task ID: 1292.050. The authors also thank Applied Materials and IBM for supplying the ultralow *k* and low *k* materials.

Chapter 6: General Conclusions

The work in this thesis presents the mechanistic study of non-damaging plasma etching and PR stripping coordinated processes for porous ULK materials. For ULK plasma etching based on C_4F_8/Ar plasma, we evaluated alternative plasma chemistries for both remote and *in situ* ashing processes as a replacement for O_2 ashing. The factors determining ULK damage were identified. Preferable process conditions were specified and compared to alternatives with the goal of preventing ULK sidewall damage while achieving production-worthy stripping rates of PR masks. *Ashing efficiency (AE) was defined as the amount of PR removed divided by the amount of ULK material damaged for a given time.*

In chapter 2, we demonstrate that H_2 remote plasmas enable practical PR stripping rates while introducing little damage to the ULK dielectric for an elevated temperature (200-275 °C) substrate. ULK damage was quantified using the DHF method (1% HF/15 s). PR ashing was more sensitive to substrate temperature than ULK damage was. An AE of ~60 was obtained with the PR ashing rate of 900 nm/min for pure H_2 remote plasma ashing at 275 °C substrate temperature. Our results showed that PR ashing rates were not greatly improved by adding Ar and N_2 to H_2 remote plasmas, whereas addition of N_2 to H_2 increased ULK damage dramatically. The N_2 addition to H_2 degraded AE from 60 to less than 10 and had very little benefit.

ULK plasma etching process using 10% C_4F_8/Ar plasma deposited FC coating on ULK feature sidewalls. H_2 remote plasma ashing performed in a dedicated chamber and with the substrate at high temperature lead to most of FC coating to be removed from the substrate. Its influence on ULK ashing damage, as indicated by ToF-SIMS depth profiling with deuterium, was minor.

In chapter 3 and chapter 4, the performance of the CO_2 *in situ* ashing processes was studied along with the influence of FC plasma ULK etching/*in situ* PR ashing process interaction on the materials modification. First, *in situ* ashing was performed in a clean chamber. ULK damage was quantified DHF method (0.5% /15 s). We found that for either novel CO_2 or conventional O_2 plasma, the sidewall-like damage of the pristine ULK was strongly correlated with the atomic oxygen density in the gas phase. Because the dissociation energy for CO_2 molecules that leads to production of atomic oxygen (11.5 eV) is higher than for O_2 (6 eV), the atomic oxygen density was significantly reduced in CO_2 relative to O_2 plasma under identical operation conditions, and lead to low ULK damage. Chamber pressure varied from 10 to 100 mTorr. For our unbiased conditions, the ashing rates of the pristine PR were limited by the ion current density of the discharges. Low pressure plasmas, which have high ion current and low neutral density, enabled higher ashing rates while suppressing ULK damage. PR ashing rate (unbiased) of 10 mTorr O_2 and CO_2 discharges was 134 and 57 nm/min; ULK damage was 21 and 3 nm for one min exposure. Thus, AE was improved from 6 to 19 by switching the plasma chemistry from O_2 to CO_2. Moreover, by applying substrate bias, the contribution of ion bombardment to ashing rate can be used to enhance PR ashing rates. With -90 V RF

bias, the PR ashing rate was increased to a practical value of ~250 nm/min without introducing more ULK damage, and enabled an AE of ~80.

The exposure of the process chamber to the FC plasmas required for ULK etching produced a fluorine memory effect due to FC deposition on the chamber walls. For *in situ* ashing performed in a chamber after a FC etching process, FC deposits on chamber walls can be decomposed and release fluorine into the CO_2 plasma during *in situ* ashing processes. The ULK was significantly damaged by fluorine attack. The ULK damage increased from 3 to 19 nm for 1 min of 10 mTorr CO_2 plasma processing due to the reaction with fluorine. However, since FC coating remaining on ULK sidewalls provided effective protection of the ULK against the damage from fluorine. The presence of FC coating fully restored AE to ~80 and was essential for the success of *in situ* ash processes.

The FC coating acted as a barrier and stopped reactive species of *in situ* ashing plasmas from diffusing into ULK material, thereby reduced ULK damage during the *in situ* ashing process. The interaction between the etching/ashing that influenced damage levels that were inflicted on the ULK was investigated in chapter 5. We first described temporal evolution of porous SiCOH exposed to C_4F_8/Ar-based etching, Ar surface tailoring, and CO_2 and O_2 PR ashing plasmas under sidewall-like conditions were using real-time ellipsometry. For pristine ULK exposed to O_2 plasma without ion bombardment, we showed that a near-surface highly porous layer was created. The ULK modification induced by CO_2 plasma operated at comparable plasma operating conditions was reduced relative to O_2 for exposures of the same duration, but subjected to a similar damage mechanism. For sidewall-like exposure of

ULK to C_4F_8/Ar etching plasma, FC material quickly permeated into the porous structure of the ULK material. Saturation of the surface modifications were seen after ~30 s. For our processing conditions (10% C_4F_8/Ar, 30 mTorr, 200 W source power, and 10 °C substrate temperature), we observed the formation of a FC/ULK mixed layer with an extent of ~14 nm from the ULK surface.

For a combined ULK plasma etching/PR stripping sequence, we observed that post-etching FC thickness varied between 1~2 nm on the ULK sidewall for the plasma etching process conditions examined (% C_4F_8: 5-10%; source power: 100-200 W; chamber pressure: 10-60 mTorr; gas addition: 5% O_2 or 10% N_2). This statement was based on quantitative XPS analysis. The composition of the FC films deposited under sidewall-like exposure was similar for different plasma etching conditions employing C_4F_8/Ar plasma chemistries with either O_2 or N_2 gas addition. However, a strong decrease of ULK post-ashing damage with deposited FC film thickness was found. For ULK exposed under sidewall-like conditions to the ashing plasma, the minimum post-ashing ULK damage depth for our FC plasma etching/CO_2 *in situ* ashing (300 s) combined processes was 10 nm (for C_4F_8/Ar/N_2 etching plasma exposure), but for the same ashing process the ULK damage depth ~36 nm if the PE-related residues were absent. We also noted that there was a fluorine memory effect in plasma process chambers after prior FC plasma etching processes. Therefore, the *in situ* ashing process conditions may be different, depending on the nature of the prior plasma etching process. The strong dependence of ULK damage on deposited FC film thickness indicated that the post-ashing damage was primarily determined by the FC coverage of the ULK material. The plasma etching conditions, which can enhance

FC deposition at the sidewall-like ULK surface, were expected to reduce ULK damage during subsequent exposure to the PR ashing plasmas.

Chapter 7: Future Work

In this work, ULK sidewall plasma modification was simulated using blanket ULK films exposed to plasma in a small gap structure where energetic ions were completely excluded. However, in a real pattern transfer process, when the mean free path of plasma gases is less than plasma sheath thickness, the ions could be scattered due to collision with gas molecules in the plasma sheath and subsequently bombard upper areas on feature sidewalls. To study the effect of scattered ion bombardment on ULK sidewall modification, the surface analysis for ULK sidewall exposed to etching/ *in situ* ashing plasma with a real trench structure is required. The highly porous imprint organosilicate glass (OSG) materials have been developed in National Institute of Standards and Technology (NIST). The imprint technology compatible with ULK materials can provide virgin ULK materials in trench structure. The sidewall surface can be characterized with angle-glancing XPS and serve as a baseline for ULK sidewall plasma modification in the subsequent etching/in situ ashing plasma processing. This approach provides a platform to study the plasma ULK sidewall modification due to plasma etching, surface tailoring plasma treatment, *in situ* ashing, and their combined processing. This surface analysis on the real ULK sidewalls can be complementary data for our results obtained from the small gap structure and enable the study of the effect of scattered ion on ULK surface modification.

Besides the topic of ULK plasma damage, to continue our progress in BEOL dielectric patterning process, the research of the present PhD thesis could be followed

by a research with a topic of "*Processes and Scientific Understanding of Near-Surface Alterations of Photoresist Masks for Enhanced Plasma Etch Performance and Three-Dimensional Control of Interconnect Features*". The 2007 International Technology Roadmap for Semiconductors (ITRS) points out among Interconnect Difficult Challenges the problem of three-dimensional control of interconnect features. Control of line edge roughness (LER), and etched profile shapes of trenches and vias is a prerequisite of ensuring necessary circuit performance and reliability. The formation of a stressed, ion-damaged layer at the surface of a soft polymer film would induce a buckling instability, leading to surface wrinkling and LER. Plasma-induced surface roughness results from the difference between the mechanical properties of the ion-damaged layer and the polymer underlayer which mostly depend on plasma processing parameters and the polymer structure respectively. Our team show that poly(4-vinylpyridine) (P4VP) resist eliminates plasma-induced surface roughening for etching process conditions that produce significant roughness in a wide variety of other polymers. This can be explained by the penetration of plasma vacuum ultraviolet (VUV) radiation which led to the crosslinking of polymer and suppressed the wrinkling during ion-damaged layer formation. Fundamental understanding of plasma-surface interactions in a capacitively coupled plasma (CCP) reactor are required to address dry etching integrity of 193 nm photoresists with line edge roughness and lack of etch profile control during etching. These challenges are due to several developments, including: 1) Need to control interaction of the PR mask with liquid for immersion lithography by hydrophobic surface modifications of PR materials, impacting subsequent PE performance, and 2) Introduction of tri-layer

masking (TLM) schemes for 32 and 22 nm BEOL patterning. These developments impose unprecedented challenges on photoresist/organic mask pattern transfer by plasma etching processes, and lead to intensive investigations of how plasma pre-treatments of organic mask materials prior to plasma etching may be used to achieve enhanced PR/organic mask performance during plasma etching and meet etching resistance, LER and other profile requirements.

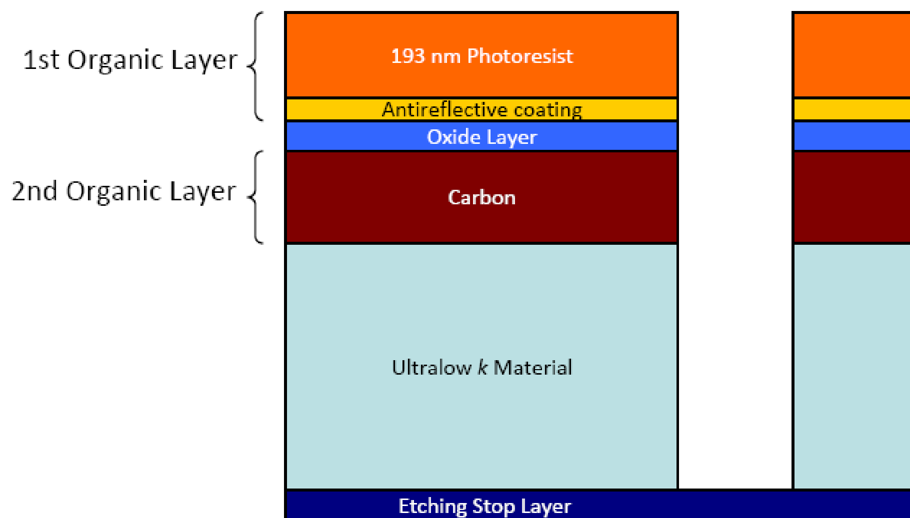

Figure 7.1: Schematic of tri-layer masking

The work would be aimed to address the question how pre-treatments of PR and organic mask materials and structures can increase plasma etching durability of PR/organic materials and structures, improve resulting dielectric profile shapes, LER control, and prevent etched profile imperfections in ULK and other dielectrics. This requires modifying in a rational and highly controlled fashion 193 nm PR surface layers to enable improved etching performance and achieve better profiles during

BEOL plasma etching. This methodology can be extended to the question how modifications of the second organic layer (carbon hard mask) in TLM approaches may be used to "harden" the "soft" high aspect ratio organic mask. In addition, the immersion lithography (IL) modified PR materials, e.g. use of a top coat hydrophobic layer or PR additives to create a thin hydrophobic layer (fluorination), may be used to improve three-dimensional control of features etched in dielectric layers. These materials alterations present an opportunity to improve surface and line edge roughness characteristics of the IL-modified PR in the plasma etch environment. Fundamental understanding of how treatments of PR layers/organic mask materials/structures following lithographic exposure and prior to plasma etch can increase plasma etch durability of PR/organic materials/structures, and improve resulting dielectric profile shapes during interconnect fabrication, along with an understanding how alterations of IL PR and modifications of the materials used for the second organic layer in tri-layer masking, can be used to improve etched profile control. The scientific elucidation of the factors that allow to improve synergy between lithography and plasma etching is expected to significantly impact our ability of "three-dimensional control of interconnect features". This research is currently under investigation at the Laboratory for Plasma Processing of Materials at the University of Maryland, College Park.

References

Chapter 1:

[1.1] Chapman, *Glow discharge Process*, (John Wiley& Sons, Inc.,1980).

[1.2] M. A. Lieberman, A. J. Lichtenberg, *Principles of Plasma Discharges and Materials Processing*, (John Wiley & Sons, Inc., 1994).

[1.3] A. Grill, *Cold Plasma in Materials Fabrication: from Fundamentals to Applications*, (Wiley-IEEE Press, 1994).

[1.4] D. M. Manos and D. L. Flamm (Eds), *Plasma Etching*, (Academic Press, 1988).

[1.5] R. J. Shul and S. J. Pearton (Eds.), *Handbook of Advanced Plasma Processing Techniques*, (Springer, 2000).

[1.6] O. A. Popov (Eds.), *High Density Plasma Sources: Design, Physics, and Performance*, (Noyes, Park Ridge, NJ, 1996).

[1.7] P. S. Ho, J. Leu, and W. W. Lee, *Low Dielectric Constant Materials for IC application*, (Springer, 2003).

[1.8] S. P. Murarka, M. Eisenberg, and A. K. Sinha, *Interlayer Dielectric: for Semiconductor Technolgies*, (Academic Press, 2003).

[1.9] *The International Technology Roadmap for Semiconductors (ITRS): 2007 Edition for Interconnect*, (Semiconductor Industry Association, 2007).

[1.10] S. Wolf, *Silicon Processing for the VLSI Era*, (Lattice Press, 2004).

[1.11] K. Maex, M. R. Baklanov, D. Shamiryan and F. Iacopi, S. H. Brongersma, and Z. S. Yanovitskaya, J. Appl. Phys. **93**, 8793 (2003).

[1.12] X. Hua, M.-S. Kuo, G. S. Oehrlein, P. Lazzeri, E. Iacob, M. Anderle, C. K. Inoki, T. S. Kuan, P. Jiang, and W.-L. Wu, J. Vac. Sci. Technol. **B 24**, 1238 (2006).

Chapter 2:

[2.1] The International Technology Roadmap for Semiconductors (ITRS): 2006 Update, Semiconductor Industry Association, 2006.

[2.2] *Low dielectric Constant Materials for IC Applications, Spring Series in Advanced Microelectronics*, edited by P. S. Ho, J. Leu, and W. W. Lee (Springer, New York, 2002), Vol 9.

[2.3] X. Hua *et al*., J. Vac. Sci. & Technol. **B 24**, 1238 (2006).

[2.4] D. Shamiryan, M. R. Baklanov, S. Vanhaelemeersch, and K. Maex, J. Vac. Sci. Technol. **B 20**, 1923 (2002).

[2.5] O. Louveau, D. Louis, M. Assous, R. Blanc, P. Brun, S. Lamy, and E. Lajoinie, Microelectron. Eng. **61-62,** 867 (2002).

[2.6] O. Louveau, C. Bourlot, A. Marfoure, I. Kalinovski, J. Su, G. Hills, and D. Louis, Microelectron. Eng. **73-74,** 351 (2004).

[2.7] D. L. Moore *et al*., J. Electrochem. Soc. **152**, G528 (2005).

[2.8] K. Yonekura, S. Sakamori, K. Goto. M. Matsuura, N. Fugiwara, and M. Yoneda, J. Vac. Sci. Technol. **B 22**, 548 (2004).

[2.9] S. Xu *et al*., J. Vac. Sci. Technol. **B 25**, 156 (2007).

[2.10] M.-S. Kuo and G. S. Oehrlein (unpublished).

[2.11] G. J. Stueber, G. S. Oehrlein, P. Lazzeri, M. Bersani, M. Anderle, R. McGowan, and E. Busch, J. Vac. Sci. Technol. **B 25**, 1593 (2007).

[2.12] L. Zheng, L. Ling, X. Hua, G. S. Oehrlein, and E. A. Hudson, J. Vac. Sci. Technol. **A 23**, 634 (2005).

[2.13] L. Ling, X. Hua, L. Zheng, G. S. Oehrlein, E. A. Hudson, and P. Jiang, J. Vac. Sci. Technol. **B 26,** 11 (2008).

[2.14] O. Richard, F. Iacopi, H. Bender, and G. Beyer, Microelectron. Eng. **84,** 517 (2007).

[2.15] R. D. Miller, J. L. Hedrick, D. Y. Yoon, R. F. Cook, and J. P. Hummel, MRS Bull. **22**, 44 (1997).

[2.16] Q. R. Huang, C. W. Frank, D. Mecerreyes, and R. D. Miller, Polym. Mater. Sci. Eng. **84**, 792 (2001).

[2.17] A. Das *et al*., Microelectron. Eng. **64**, 25 (2002).

[2.18] S. Engelmann *et al*, J. Vac. Sci. & Technol. **B 25**, 1353 (2007).

[2.19] S. Engelmann *et al*, J. Vac. Sci. Technol. **B 27**, 92 (2009).

[2.20] J. W. Coburn and M. Chen, J. Appl. Phys. **51**, 3134 (1980).

[2.21] Q. T. Le, M. R. Baklanov, E. Kesters, A. Azioune, H. Struyf, W. Boullart, J.-J. Pireaux, and S. Vanhaelemeersch, Electrochem, Solid-State Lett. **8**, F21 (2005).

[2.22] R. W. B. Pearse and A. G. Gaydon (Chapman and Hall, London, 1976), pp. 217-220.

[2.23] Yu. Ralchenko, A. E. Kramida, J. Reader, and NIST ASD Team (2008). NIST Atomic Spectra Database (version 3.1.5) (online).

[2.24] J. Amorim, G. Baravian, and A. Ricard, Plasma Chem. Plasma Process. **15**, 721 (1995).

[2.25] B. Gordiets, C. M. Ferreira, M. J. Pinheiro, and A. Ricard, Plasma Source Sci. Technol. **7**, 379 (1998).

[2.26] T. Belmonte, L. Lefèvre, T. Czerwiec, H. Michel, and A. Ricard, Thin Solid Films **341**, 27 (1999).

[2.27] S. M. Tarr, J. A. Schiavone, and R. S. Freund, Phys. Rev. Letters **44**, 1660 (1980).

[2.28] R. Nagpal and A. Garscadden, Chem. Phys. Letters **231**, 211 (1994).

[2.29] A. R. de Souza, M. Digiacomo, J. L. R. Muzart, J. Nahorny, and A. Ricard, Eur. Phys. J. AP **5**, 185 (1999).

[2.30] I. L. Berry, Q. Han, C. Waldfried, O. Escorcia, and A. Becknell, SEMI Technical Symposium 2004 (unpublished).

[2.31] P. Lazzeri, G. J. Stueber, G. S. Oehrlein, R. McGowan, E. Busch, R. Pederzoli, M. Bersani, and M. Anderle, J. Vac. Sci. Technol. **B 24,** 2695 (2006).

[2.32] P. Lazzeri, G. J. Stueber, G. S. Oehrlein, R. McGowan, E. Busch, S. Pederzoli, C. Jeynes d, M. Bersani, and M. Anderle, Thin Solid Films **516**, 3697 (2008).

[2.33] D. Briggs, *Surface analysis of polymers by XPS and static SIMS* (Cambridge University Press, Cambridge, 1998).

[2.34] A. Grill, V. Sternhagen, D. Neumayer, and V. Patel, J. Appl. Phys. **98**, 074502 (2005).

Chapter 3:

[3.1] P. S. Ho, J. Leu and W. W. Lee (Eds.), *Low dielectric Constant Materials for IC Applications, Spring Series in Advanced Microelectronics*, *Vol. 9*, (Springer, 2002).

[3.2] S. P. Murarka, M. Eizenberg, and A. K. Sinha, *Interlayer Dielectrics for Semiconductor Technologies*, (Elsevier, 2003).

[3.3] K. Maex, M. R. Baklanov, D. Shamiryan, F. Iacopi, S. H. Brongersma, Z. S. Yanovitskaya, J. Appl. Phys. **93**, 8793 (2003).

[3.4] *The International Technology Roadmap for Semiconductor (ITRS): 2003 Edition for Executive Summary*, (Semiconductor Industry Association, 2003).

[3.5] *The International Technology Roadmap for Semiconductors (ITRS): 2007 Edition for Interconnect*, (Semiconductor Industry Association, 2007).

[3.6] C. Waldfried, O. Escorcia, Q. Han, and P. B. Smith, Electrochem. Solid-State Lett. **6**, G137 (2003).

[3.7] X. Hua, M.-S. Kuo, G. S. Oehrlein, P. Lazzeri, E. Iacob, M. Anderle, C. K. Inoki, T. S. Kuan, P. Jiang, and W.-L. Wu, J. Vac. Sci. & Technol. **B 24**, 1238 (2006).

[3.8] G. J. Stueber, G. S. Oehrlein, P. Lazzeri, M. Bersani, M. Anderle, R. McGowan, and E. Busch, J. Vac. Sci. Technol. **B 25**, 1593 (2007).

[3.9] M.-S. Kuo, X. Hua, G. S. Oehrlein, A. Ali, P. Jiang, P. Lazzeri, and M. Anderle, J. Vac. Sci. Technol. **B 28**, pp. (2010).

[3.10] M. A. Hartney, D. W. Hess, and D. S. Soane, J. Vac. Sci. Technol. **B7**, 1 (1989).

[3.11] R. Doering and Y. Nishi, *Handbook of semiconductor manufacturing technology*, (CRC Press, 2007).

[3.12] A. M. Urbanowicz, V. V. Talanov, M. Pantouvaki, H. Struyf, S. De Gendt, and M. R. Baklanov, IEEE Interconnect Technology Conference, 2009. IITC 2009. IEEE International Volume, 134 (2009).

[3.13] N. Posseme, T. Chevolleau, T. David, M. Darnon, O. Louveau, and O. Joubert, J. Vac. Sci. Technol. **B 25**, 1928 (2007).

[3.14] J. Bao, H. Shi, J. Liu, H. Huang, P. S. Ho, M. D. Goodner, M. Moinpour, and G. M. Kloster, J. Vac. Sci. Technol. **B 26,** 216 (2008).

[3.15] C. M. Fuller, M. A. Worsley, L. Tai, S. Bent, C. Labelle, A. Arnold, T. Dalton, Thin Solid Films **516**, 3558 (2008).

[3.16] M. A. Worsley, S. F. Bent, S. M. Gates, N. C. F. Fuller, W. Volksen, M. Steen and T. Dalton, J. Vac. Sci. Technol. **B 23**, 395 (2005).

[3.17] L. Zheng, L. Ling, X. Hua, G. S. Oehrlein, and E. A. Hudson, J. Vac. Sci. Technol. **A 23**, 634 (2005).

[3.18] L. Ling., X. Hua, L. Zheng, G. S. Oehrlein, E. Hudson, and P. Jiang, J. Vac. Sci. Technol. **B 26**, 11 (2008).

[3.19] Q. T. Le, M. R. Baklanov, E. Kesters, A. Azioune, H. Struyf, W. Boullart, J.-J. Pireaux, and S. Vanhaelemeersch, Electrochem, Solid-State Lett. **8**, F21 (2005).

[3.20] J. W. Coburn and M. Chen, J. Appl. Phys. **51**, 3134 (1980).

[3.21] Ralchenko, Yu., Kramida, A. E., Reader, J. and NIST ASD Team (2008). *NIST Atomic Spectra Database* (version 3.1.5), [Online].

[3.22] N. C. M. Fuller, M. V. Malysev, V. M. Donnelly, and I. P. Herman, Plasma Source Sci. Technol. **9**, 116 (2000).

[3.23] M. A. Worsley, S. F. Bent, N. C. M. Fuller, and T. Dalton, J. Appl. Phys. **100**, 083301 (2006).

[3.24] A. Fridman, *Plasma Chemistry*, (Cambridge, 2008) p. 265.

[3.25] R. S. Freund, J. Chem. Phys. **55**, 3569 (1971).

[3.26] P. C. Cosby, J. Chem. Phys. **98**, 9560 (1993).

[3.27] E. J. H Collart, J. A. G. Baggerman, and R. J. Visser, J. Appl. Phys. **78**, 47 (1995).

[3.28] O. Joubert, J. Pelletier, and Y. Arnal, J. Appl. Phys. **65**, 5096 (1989).

[3.29] X. Li, L. Ling, X. Hua, G. S. Oehrlein, Y. Wang, and H. M. Anderson, J. Vac. Sci. Technol. **A 21**, 1955 (2003).

[3.30] J. A. G. Baggerman, R. J. Visser, and E. J. H. Collart, J. Appl. Phys. **75**, 758 (1994).

[3.31] T. E. F. M. Standaert, P. J. Matsuo, X. Li, G. S. Oehrlein, T.-M. Lu, R. Gutmann, C. T. Rosenmayer, J. W. Bartz, J. G. Langan, and W. R. Entley, J. Vac. Sci. Technol. **A 19**, 435 (2001).

[3.32] W. E. Vanderlinde and A. L. Ruoff, J. Vac. Sci. Technol. **B 6**, 1621 (1988).

[3.33] D. Briggs, *Surface analysis of polymers by XPS and static SIMS*, (Cambridge, 1998).

[3.34] G. Vargo and J. A. Gardella, Jr., J. Vac. Sci. Technol. **A 7**, 1733 (1989).

[3.35] C. Chang, P. T. Liu, Y. S. Mor, T. M. Tsai, C. W. Chen, Y. J. Mei, F. M. Pan, W. F. Wu, and S. M. Sze, J. Vac. Sci. Technol. **B 20**, 1561 (2002).

[3.36] Chaudhari, J. Du, S. Behera, S. Manandhar, S. Gaddam, and J. Kelber, Appl. Phys. Lett. **94**, 204102 (2009).

Chapter 4:

[4.1] *The International Technology Roadmap for Semiconductors (ITRS): 2007 Edition for Interconnect*, (Semiconductor Industry Association, 2007).

[4.2] M.-S. Kuo, A. R. Pal, G. S. Oehrlein, P. Lazzeri, and M. Anderle, Mechanistic Study of ULK-Compatible CO_2 *In Situ* Photoresist Ashing Processes. I. Process Performance and Influence on ULK Material Modification, (unpublished).

[4.3] L. Zheng, L. Ling, X. Hua, G. S. Oehrlein, and E. A. Hudson, J. Vac. Sci. Technol. **A 23**, 634 (2005).

[4.4] L. Ling, *Ph. D. Thesis*, (2006).

[4.5] K. Tokashiki, T. Maruyama, and A. Nishizawa, IEEE Transactions on Semiconductor Manufacturing, **17**, 305 (2004).

[4.6] Y. Furukawa, M. Patz, T. Kokubo, and J. H. M. Snijders, Microelectron. Eng. **70**, 267 (2003).

[4.7] O. Richard, F. Iacopi, H. Bender, and G. Beyer, Microelectron. Eng. **84**, 517 (2007).

[4.8] M.-S. Kuo, X. Hua, G. S. Oehrlein, A. Ali, P. Jiang, P. Lazzeri, and M. Anderle, J. Vac. Sci. Technol. **B 28**, (2010).

[4.9] N. C. M. Fuller, M. A. Worsley, L. Tai, S. Bent, C. Labelle, J. Arnold, and T. Dalton, Thin Solid Films **516**, 3558 (2008).

[4.10] L. Ling, X. Hua, X. Li, G. S. Oehrlein, E. Hudson, P. Lazzeri, N. Coghe, M. Anderle, J. Vac. Sci. Technol. **B 22**, 2594 (2004).

[4.11] S. Engelmann, R. L. Bruce, M. Sumiya, T. Kwon, R. Phaneuf, G. S. Oehrlein, C. Andes, D. Graves, D. Nest, and E. A. Hudson, J. Vac. Sci. & Technol. **B 27**, 92 (2009).

[4.12] S. Engelmann, R. L. Bruce, F. Weilnboeck, M. Sumiya, T. Kwon, R. Phaneuf, G. S. Oehrlein, C. Andes, D. Graves, D. Nest, and E. A. Hudson, J. Vac. Sci. & Technol. **B 27**, 1165 (2009).

[4.13] J. J. Hannon and J. M. Cook, J. Electrochem. Soc. **131**, 1164 (1984).

[4.14] D. M. Manos and D. L. Flamm, *Plasma Etch: An Introduction*, (Academic Press, 1989) p. 168.

[4.15] D. Briggs, *Surface analysis of polymers by XPS and static SIMS,* (Cambridge University Press, 1998).

[4.16] S.-H. Jeong, J. Nishii, H.-R. Park, J.-K. Kim, B.-T. Lee, Surf. Coat. Technol. **168**, 51 (2003).

[4.17] G. Beamson and D. Briggs, *High resolution XPS of organic polymers: the Scientia ESCA 300 database* (Wiley, *1992*).

[4.18] D. Briggs and M. P. Seah, *Practical Surface Analysis*, Vol. 1, (Wiley, 1990).

Chapter 5:

[5.1] *The International Technology Roadmap for Semiconductors (ITRS): 2007 Edition for Interconnect*, (Semiconductor Industry Association, 2007).

[5.2] M. R. Baklanov, Q. T. Le, E. Kesters, F. Iacopi, J. Van Aelst, H. Struyf, W. Boullart, S. Vanhaelemeersch, and K. Maex, Interconnect Technology Conference, 2004. Proceedings of the IEEE 2004 International, 187 (2004).

[5.3] K. Maex, M. R. Baklanov, D. Shamiryan and F. Iacopi, S. H. Brongersma, and Z. S. Yanovitskaya, J. Appl. Phys. **93**, 8793 (2003).

[5.4] O. Richard, F. Iacopi, H. Bender, and G. Beyer, Microelectron. Eng. **84**, 517 (2007).

[5.5] X. Hua, M.-S. Kuo, G. S. Oehrlein, P. Lazzeri, E. Iacob, M. Anderle, C. K. Inoki, T. S. Kuan, P. Jiang, and W.-L. Wu, J. Vac. Sci. & Technol. **B 24**, 1238 (2006).

[5.6] N. Posseme, T. Chevolleau, T. David, M. Darnon, O. Louveau, and O. Joubert, J. Vac. Sci. Technol. **B 25**, 1928 (2007).

[5.7] B. Kong, T. Choi, S. Sirard, D. J. Kim, and N.-E. Lee, J. Vac. Sci. Technol. **A 25**, 986 (2007).

[5.8] Y. Furukawa, M. Patz, T. Kokubo, and J. H. M. Snijders, Microelectron. Eng. **70**, 267 (2003).

[5.9] N. C. M. Fuller, M. A. Worsley, L. Tai, S. Bent, C. Labelle, J. Arnold, and T. Dalton, Thin Solid Films **516**, 3558 (2008).

[5.10] A. Furuya, E. Soda, M. Shimada, and S. Ogawa, Jpn. J. Appl. Phys. **44,** 7430 (2005).

[5.11] M.-S. Kuo, A. R. Pal, G. S. Oehrlein, P. Lazzeri, and M. Anderle, Mechanistic Study of ULK-Compatible CO_2 *In Situ* Photoresist Ashing Processes. I. Process Performance and Influence on ULK Material Modification, (unpublished).

[5.12] S. Jain, V. Zubkov, T. Nowak, A. Demos, and J. Rocha, Solid State Technology **48**, 43 (2005).

[5.13] A. Grill, S. Gates, C. Dimitrakopoulos, V. Patel, S. Cohen, Y. Ostrovski, E. Liniger, E. Simonyi, D. Restaino, S. Sankaran, S. Reiter, A. Demos, K. S. Yim, V. Nguyen, J. Rocha, D. Ho, 2008 IEEE International Interconnect Technology Conference, IITC, p. 28-30 (2008).

[5.14] L. Ling, X. Li, G. S. Oehrlein, E. A. Hudson, P. Lazzeri, and M. Anderle, J. Vac. Sci. Technol. **B 22**, 2594 (2004).

[5.15] R. L. Bruce, S. Engelmann, T. Lin, T. Kwon, R. J. Phaneuf, G. S. Oehrlein, B. K. Long, C. G. Willson, J. J. Végh, D. Nest, D. B. Graves, and A. Alizadeh, J. Vac. Sci. Technol. **B 27**, 1142 (2009).

[5.16] A. Das, T. Kokubo, Y. Furukawa, H. Struyf, I. Vos, B. Sijmus, F. Iacopi, J. Van Aelst, Q. T. Le, L. Carbonell, S. Brongersma, M. Maenhoudt, Z. Tokei, I. Vervoort, and E. Sleeckx, Microelectron. Eng. **64**, 25 (2002).

[5.17] D. Shamiryan, M. R. Baklanov, S. Vanhaelemeersch, and K. Maex, J. Vac. Sci. Technol. **B 20**, 1923 (2002).

[5.18] J. Bao, H. Shi, J. Liu, H. Huang, P. S. Ho, M. D. Goodner, M. Moinpour, and G. M. Kloster, J. Vac. Sci. Technol. **B 26**, 219 (2008).

[5.19] D. Briggs, Surface *analysis of polymers by XPS and static SIMS*, (Cambridge University Press, 1998).

[5.20] M.-S. Kuo, A. R. Pal, G. S. Oehrlein, and X. Hua, Mechanistic Study of ULK-Compatible CO_2 *In Situ* Photoresist Ashing Processes. II. Interaction with Preceding Fluorocarbon Plasma ULK Etching Processes, (unpublished).

[5.21] K. Tokashiki, T. Maruyama, and A. Nishizawa, IEEE Transactions on Semiconductor Manufacturing, **17**, 305 (2004).